Optimization of NEMS for Frequency Shift Sensing Applications

Thesis by
Elizabeth Caryn Bullard

In Partial Fulfillment of the Requirements for the
degree of
Doctor of Philosophy

CALIFORNIA INSTITUTE OF TECHNOLOGY
Pasadena, California

2016
Defended March 29, 2016

© 2016

Elizabeth Caryn Bullard
ORCID: orcid.org/0000-0001-8579-2147

All rights reserved

ACKNOWLEDGEMENTS

ABSTRACT

This thesis has two areas of focus: the application of the dynamic similarity principle in microelectromechancial systems (MEMS) and nanoelectromechanical systems (NEMS) and the study of anomalous phase noise (APN) in MEMS and NEMS. In the first portion of the thesis, we employ the dynamic similarity principle to predict the quality factor due to gas damping in MEMS and NEMS. In the second portion of the thesis, we provide a theoretical framework for sources of phase noise in MEMS and NEMS and describe the measurements that we made to quantify the temperature dependence of anomalous phase noise in silicon doubly clamped beams.

PUBLISHED CONTENT AND CONTRIBUTIONS

[1]E. C. Bullard, J. Li, C. R. Lilley, P. Mulvaney, M. L. Roukes, and J. E. Sader, "Dynamic similarity of oscillatory flows induced by nanomechanical resonators", Phys. Rev. Lett. **112**, 015501 (2014),
E.C.B. performed substantial portions of the device fabrication, performed all measurements and analysis, assisted in the writing of the main manuscript and wrote the supplementary information.

[2]M. S. Hanay, S. Kelber, A. K. Naik, D. Chi, S. Hentz, E. C. Bullard, E. Colinet, L. Duraffourg, and M. L. Roukes, "Single-protein nanomechanical mass spectrometry in real time", Nature Nanotechnology **7**, 602–608 (2012),
E.C.B. assisted in the construction and commissioning of the ESI setup and assisted in the initial measurements employing the ESI setup.

[3]M. Sansa, E. Sage, E. C. Bullard, M. Gély, T. Alava, E. Colinet, A. K. Naik, L. G. Villanueva, Duraffourg, M. L. Roukes, G. Jourdan, and S. Hentz, "Frequency fluctuations in silicon nanoresonators", Nature Nanotechnology (2016) `doi:10.1038/nnano.2016.19`,
E.C.B. participated in discussions on phase noise in the silicon nanoresonators and provided comments on the manuscript.

TABLE OF CONTENTS

Acknowledgements iii
Abstract iv
Published Content and Contributions v
Table of Contents vi
List of Illustrations viii
List of Tables xii
Chapter I: Introduction 1
Chapter II: Dynamic Similarity of Oscillatory Flows Induced by NEMS . . . 4
2.1 Overview 4
2.2 Gas Damping in MEMS and NEMS 4
2.3 Theory 5
2.4 Device Fabrication 10
2.5 Experimental Setup 12
2.6 Measurements 16
2.7 Analysis 20
2.8 Conclusion 27
Chapter III: Phase Noise in Oscillators 31
3.1 Overview of Oscillators 32
3.2 Frequency Stability Measurements 33
3.3 Comparison of Frequency Stability Measurement Techniques 36
3.4 Sources of Frequency Noise 38
3.5 Power Law Dependence of Phase Noise 39
3.6 Previous Knowledge of Anomalous Phase Noise 44
3.7 Summary 49
Chapter IV: Sources of Phase Noise in MEMS and NEMS 50
4.1 Noise Analysis of a Phase Feedback Oscillator 51
4.2 Prototype Device 57
4.3 Thermomechanical Noise 59
4.4 Parameter Fluctuations: Ω_0 62
4.5 Summary of Phase Noise Sources 89
Chapter V: Experimental Setup 93
5.1 Overview of Optical Setup 93
5.2 Optical System Design 93
5.3 Detection System 103
5.4 Actuation System 110
5.5 Annealing System 113
5.6 Vacuum System 113
5.7 Cryostat and Sample Holder 115
5.8 Sample Fabrication 115

5.9 Summary . . . 117
Chapter VI: Characterization of Anomalous Phase Noise . . . 119
6.1 Temperature Calibration . . . 119
6.2 Oscillator Setup . . . 122
6.3 Temperature Dependence of Anomalous Phase Noise . . . 123
6.4 Frequency Dependence of Anomalous Phase Noise . . . 130
6.5 Mode Dependence of Anomalous Phase Noise . . . 131
6.6 Back Action . . . 133
6.7 Noise Analysis . . . 134
6.8 Summary . . . 138
Chapter VII: Conclusion . . . 140
Bibliography . . . 141

LIST OF ILLUSTRATIONS

Number *Page*

2.1 Device Fabrication 11
2.2 Colorized Images of 100 nm Devices 13
2.3 Experimental Setup for Measurements 14
2.4 Optical Setup 14
2.5 Frequency Spectrum of Laser Noise 18
2.6 Thermomechanical Noise Peak 19
2.7 Measurement of 500 nm 10:1 Aspect Ratio Device. 20
2.8 Plot of Pressure vs Q for Die A Cantilevers with Aspect Ratio 10:3 . 21
2.9 Plot of Pressure vs Q for Die A Cantilevers with Aspect Ratio 5:1 . . 21
2.10 Plot of Pressure vs Q for Die A Cantilevers with Aspect Ratio 10:1 . 22
2.11 Plot of Pressure vs Q for Die C Cantilevers with Legs 22
2.12 Plot of Pressure vs Q for Die C Square Headed Cantilevers 23
2.13 Plot of Pressure vs Q for Die C Triangular Cantilevers 23
2.14 Plot of Kn vs Q_{SCALED} for Die A Cantilevers with Aspect Ratio 10:3 27
2.15 Plot of Kn vs Q_{SCALED} for Die A Cantilevers with Aspect Ratio 5:1 . 28
2.16 Plot of Kn vs Q_{SCALED} for Die A Cantilevers with Aspect Ratio 10:1 28
2.17 Plot of Kn vs Q_{SCALED} for Die C Cantilevers with Legs 29
2.18 Plot of Kn vs Q_{SCALED} for Die C Square Headed Cantilevers 29
2.19 Plot of Kn vs Q_{SCALED} for Die C Triangular Cantilevers 30
3.1 Diagram of a Feedback Oscillator 32
3.2 Comparison of Phase and Amplitude Fluctuations. 33
3.3 Allan Deviation Measurement Setup 37
3.4 Phase Noise Measurement Setup 38

3.5 Power Law Dependence of Phase Noise 41

3.6 Power Law Dependence of Allan Deviation. 41

3.7 Diagram of a Feedback Oscillator with Phase Fluctuations 42

3.8 Temperature versus $S_0(T) = S_y(f)f$ 48

4.1 Diagram of a phase feedback oscillator with operating parameters. . . 51

4.2 Colorized image of a Si doubly clamped beam. 58

4.3 Comparison of Direct and A$-\phi$ Conversion Thermomechanical Phase Noise. 61

4.4 Comparison of Thermomechanical Noise 62

4.5 Thermal model for a doubly clamped beam. 63

4.6 Comparison of phase noise. 67

4.8 Comparison of phase noise. 71

4.7 Comparison of $Q_{e,n}$ values. 72

4.9 Geometry for charge noise model 73

4.10 Comparison of phase noise 75

4.11 Comparison of phase noise. 78

4.12 Asymptotes of $\psi(x)$. 80

4.13 Comparison of phase noise. 81

4.14 Comparison of phase noise. 83

4.15 Comparison of phase noise. 89

5.1 Schematic of the Optical Setup 94

5.2 Diagram of the Focal Plane 97

5.3 Knife Edge Measurement 97

5.4 Knife Edge Measurement for w_x 98

5.5 Knife Edge Measurement for w_y 98

5.6 A ray trace showing an ideal lens 100

5.7 A ray trace showing spherical aberration 100

5.8 A ray tracing showing coma. 101
5.9 Simple Interferometer 103
5.10 Interference pattern for $\lambda = 632.8nm$. 105
5.11 Detection beam power vs Δf. 106
5.12 Setup for Measuring Thermomechanical Noise 108
5.13 Thermomechanical Noise of Device #3 at 297K 109
5.14 Background Noise for Device #3 at 297K 110
5.15 Angular emission of a semiconductor laser 111
5.16 Photograph of Vacuum Setup 114
5.17 RGA Spectrum Before Bake Out 115
5.18 Photograph of Sample Holder 116
5.19 Device Fabrication for Phase Noise Measurements 118
5.20 Colorized image of a Si doubly clamped beam. 118
6.1 Measurement Setup for Temperature Calibration 120
6.2 Backbone curve for Device #3 at 297K 121
6.3 Thermomechanical Noise of Device #3 at 297K 121
6.4 Diagram of Oscillator Setup 122
6.5 Fit of amplitude squared versus fractional frequency shift for Device # 2 125
6.6 Fit of amplitude squared versus fractional frequency shift for Device # 3 126
6.7 Phase Noise of Device #3 vs Temperature 127
6.8 Comparison of Phase Noise at 23 K 128
6.9 Comparison of Phase Noise at 55 K 128
6.10 Comparison of Phase Noise at 297 K 129
6.11 Comparison of Phase Noise at 10 Hz Offset vs Temperature 130
6.12 Frequency Dependence of Phase Noise at T=25 K 131

6.13 Frequency Dependence of Phase Noise at T=45 K 131

6.14 Frequency Dependence of Phase Noise at T=297 K 132

6.15 Comparison of phase noise measured in first and second mode of Device #3. 132

6.16 Comparison of Phase Noise at 297 K 133

6.17 Comparison of phase noise from N518A at two different drive levels . 135

6.18 Comparison of phase noise from components under test 136

6.19 Comparison of phase noise 138

LIST OF TABLES

Number *Page*

2.1 Measured and Predicted Q_{GAS} for Die A 27
2.2 Measured and Predicted Q_{GAS} for Die C 27
3.1 Power Law Dependence of Selected Phase Noise Processes 40
3.2 Power Law Dependence for Allan Deviation 40
4.1 Diffusion Coefficients 57
4.2 Prototype Device Properties 58
4.3 Material Properties 58
4.4 Mode Shape Parameters 60
4.5 Mode Shape Parameters for Modes 1 and 2 82
4.6 Summary of Sources of Phase Noise 91
4.7 Summary of Allan Deviation 92
6.1 Temperature Dependent Properties of Device #2 124
6.2 Temperature Dependent Properties of Device #3 124
6.3 Comparison of Actuation Efficiency vs Temperature for Device #2 . . 125
6.4 Comparison of Actuation Efficiency vs Temperature for Device #3 . . 125
6.5 Table of Operation Points for Device #3 126
6.6 Table of Operation Points 129

Chapter 1

INTRODUCTION

This thesis has two areas of focus: the application of the dynamic similarity principle in microelectromechancial systems (MEMS) and nanoelectromechanical systems (NEMS) and the study of anomalous phase noise (APN) in MEMS and NEMS. In the first portion of the thesis, we employ the dynamic similarity principle to predict the quality factor due to gas damping in MEMS and NEMS. In the second portion of the thesis, we provide a theoretical framework for sources of phase noise in MEMS and NEMS and describe the measurements that we made to quantify the temperature dependence of anomalous phase noise in silicon doubly clamped beams. In this chapter, we provide an overview of the entire thesis.

In Chapter 2, we describe the application of the dynamic similarity principle to predict quality factor due to gas damping. We derive the formula used to predict the quality factor due to gas damping, Q_{GAS} in MEMS and NEMS. We describe the prototype devices used to validate the theory. Specifically, we used rectangular cantilever with different aspect ratios, for which an analytical expression for Q_{GAS} exists in the rarefied and continuum flow regimes. We also used triangular cantilevers and square headed cantilevers, for which an analytical expression for Q_{GAS} exists only in the rarefied gas regime. We describe the pressure vs quality factor measurements made to validate the theory. We then analyze the data and compare the data with the results predicted by the dynamic similarity principle and with the results predicted by the analytical expressions, where appropriate. We demonstrate that the dynamic similarity principle accurately predicts Q_{GAS} for a wide range of devices.

In Chapter 3, we discuss the applications of MEMS and NEMS as frequency shift

sensors and as oscillators. We discuss how noise limits the frequency stability in these devices. We then give an overview of feedback oscillators, before discussing the metrics used to characterize noise in oscillators: amplitude noise, phase noise, fractional frequency noise, and Allan deviation. We also discuss the frequency dependence of various noise sources. We next discuss anomalous phase noise (APN), a source of phase noise of unknown origin present in a wide variety of MEMS and NEMS. APN limits the frequency stability of these devices to a stability above the thermomechanical noise limit. APN currently limits the frequency stability of NEMS oscillators and the minimum detectable mass of NEMS mass sensors. We end with a discussion of our current knowledge of APN.

In Chapter 4, we provide a theoretical framework for sources of phase noise in MEMS and NEMS. We then provide a derivation of many potential sources of phase noise. We also calculate the expected phase noise for a test device. We address the following sources of phase noise in a device: direct thermomechanical noise, amplitude to phase conversion thermomechanical noise, temperature fluctuation noise, extensional fluctuation noise, charge fluctuation noise, gas interaction noise, defect motion noise, noise from higher order mode coupling, and noise from defect reorientation. We end the chapter with two summary tables containing expressions for phase noise due to these sources and the Allan deviation due to these sources.

In Chapter 5, we describe the experimental setup used to measure anomalous phase noise in a silicon doubly clamped beam over a range of temperatures. We describe the optical setup used to actuate and detect the devices, as well as to anneal them, the vacuum system used for the measurements, and the cryostat and sample holder used. We end with a description of the fabrication process for the devices.

In Chapter 6, we measure the phase noise of silicon doubly clamped beams over a range of temperatures. We begin with a description of the oscillator setup used

for the phase noise measurements, as well as a characterization of the noise in the measurement setup. We then use the oscillator setup to measure the phase noise of two silicon doubly clamped beams over a range of temperatures. We then anneal one of the devices and measure the phase noise post-anneal. We end the chapter with a summary of the data.

In Chapter 7, we discuss our conclusions and further avenues of study. We consider further measurements to quantify anomalous phase noise. We also consider methods to limit anomalous phase noise.

Chapter 2

DYNAMIC SIMILARITY OF OSCILLATORY FLOWS INDUCED BY NEMS

2.1 Overview

The dynamic similarity principle offers an alternate method to determine the quality factor due to gas damping. Unlike numerical simulations, which can require computationally intensive calculations, the dynamic similarity principle allows us to predict the quality factor of a prototype device through a measurement of the quality factor on a scaled device. In order to determine the quality factor of a prototype device at a pressure P_0, we measure the quality factor at a pressure P_0/n on a device that has been scaled up by a factor of n.

2.2 Gas Damping in MEMS and NEMS

MEMS and NEMS have a wide range of applications, including AFM[1], gas sensing[2], and mass spectrometry at both the atomic[3] and molecular scale[4]. An important characteristic of these devices is their quality factor, Q. For AFM cantilevers, the minimum detectable force is ideally proportional to $1/Q$[5]. For cantilevers used in gas damping, the response time of the cantilever, τ_0, is approximately Q/f_0, where f_0 is the resonant frequency of the device[6]. The response time of the cantilever controls how quickly it responds to a change in the gas mixture. Thus, the quality factor determines the sensitivity of the devices.

The quality factor is an important design parameter. For devices operating at atmospheric pressure, the quality factor is generally dominated by gas damping. Devices with a width on the order of tens to hundreds of nanometers operate in the transition flow regime. In the transition flow regime, the calculation of the quality

factor due to gas damping requires numerical simulations[7]. These simulations are complex and time and resource intensive. The dynamic similarity principle offers a simpler, alternate method to predict the quality factor; a measurement on a scaled device is used to predict the performance of the prototype device.

The dynamic similarity principle allows us to measure the quality factor of a scaled device at a scaled pressure and use that measurement to predict the quality factor of the prototype device. The dynamic similarity principle has been used previously to successfully predict the aerodynamic properties of aircraft using wind tunnels[8]. In that case, the prototype model is scaled down and the flow conditions are scaled appropriately to determine the aerodynamic properties of the plane. We apply the dynamic similarity principle in a novel endeavor: the prediction of fluid flows on the nanoscale. In order to determine the quality factor of a prototype device at a pressure P_0, we measure the quality factor of a device that has been scaled up by a factor of n at a pressure P_0/n. We then use the measured quality factor to predict the quality factor of the prototype at P_0.

2.3 Theory

In this section, we discuss the governing equations for gas flows and the calculation of the quality factor due to gas damping. We then then employ the dynamic similarity principle to derive an expression for the quality factor of a prototype device from a measurement of the quality factor of a scaled device.

Gas Damping

The theoretical model used to describe gas damping depends upon the Knudsen number, Kn. The Knudsen number is the ratio of the mean free path of gas, λ, to the critical length scale of the device, L_0 [9].

$$\mathrm{Kn} = \frac{\lambda}{L_0}. \tag{2.1}$$

The mean free path of a gas is given in Eq. 2.2 [9]:

$$\lambda = \frac{1}{2^{1/2}\pi d_0^2 \rho_{gas}}, \tag{2.2}$$

where d_0 is the molecular diameter and ρ_{gas} is the gas density. For N_2 gas, $d_0 = 3.75 \times 10^{-10}$m [9]. We rewrite Eq. 2.2 in terms of the gas pressure, P, using the ideal gas law, $P = \rho_{gas} k_B T$.

$$\lambda = \frac{k_B T}{2^{1/2}\pi d_0^2 P}, \tag{2.3}$$

where k_B is Boltzmann's constant and T is the temperature. For a rectangular cantilever, the critical dimension is $b/2$ [10], where b is the width of the cantilever. We then rewrite the expression for the Knudsen number:

$$\mathrm{Kn} = \frac{1}{b}\frac{2^{1/2} k_B T}{\pi d_0^2 P}. \tag{2.4}$$

There are four regions of flow [7]. For $\mathrm{Kn} \leq 10^{-2}$, the fluid surrounding the device is treated as a continuum and the flow is governed by the Navier-Stokes equations with the no-slip boundary condition; the velocity tangential to the surface is zero. For $10^{-2} < \mathrm{Kn} < 0.1$, the no-slip boundary condition no longer applies. A constant-slip velocity value is assumed at the boundary between the fluid and the surface. The flow is governed by the Navier-Stokes equations, with corrections from Maxwell's velocity slip boundary condition and von Smoluchowski's temperature jump boundary condition. In the transition flow regime, ($0.1 < \mathrm{Kn} < 10$), higher order corrections are required for the governing equations for the stress tensor and heat flux vector of the fluid; the flow is described by the Burnett equations. Determining the quality factor due to gas damping in this regime requires computational simulations. In the free molecular flow regime, $\mathrm{Kn} \geq 10$. Devices operating in the transition regime are of special interest. We can use the dynamic similarity to predict the quality factor due to gas damping of these devices, obviating the need for complex numerical simulations.

Dynamic Similarity Principle

In order to test the dynamic similarity principle, we formulate a model for Q in terms of the experimental parameters. Following the derivation given by Sader et al. [10], we model the cantilever as a linear harmonic oscillator with one degree of freedom. The damping force on the oscillator is proportional to the velocity of the oscillator. We define Q as given in Eq. 2.5.

$$Q \equiv 2\pi \left. \frac{E_{stored}}{E_{diss}} \right|_{\omega=\omega_R}, \tag{2.5}$$

where ω_R is the radial resonant frequency in gas. E_{diss} is the energy dissipated by the oscillator during once cycle of oscillation. For a linear harmonic oscillator, $E_{stored} = \frac{1}{2}kA^2$, where k is the spring constant of the oscillator and A is the amplitude of the oscillation. For a linear oscillator, the energy dissipated per cycle and the energy stored per cycle are both proportional to A^2. We rewrite Eq. 2.5,

$$Q = 2\pi \left. \frac{\frac{\partial^2 E_{stored}}{\partial A^2}}{\frac{\partial^2 E_{diss}}{\partial A^2}} \right|_{\omega=\omega_R}. \tag{2.6}$$

By combining Eq. 2.6 with $\frac{\partial^2 E_{stored}}{\partial A^2} = k$, we determine a relationship between k and the energy dissipated:

$$k = \left(\frac{1}{2\pi} \left. \frac{\partial^2 E_{diss}}{\partial A^2} \right|_{\omega=\omega_R} \right) Q. \tag{2.7}$$

We now consider what properties affect the energy dissipation of the cantilever. The energy dissipation depends upon the square of the oscillation amplitude, A, the gas density, ρ_{gas}, the length scale of the resonator, L_0, its radial resonant frequency in gas, ω_R, the fluid shear viscosity, μ, and the Knudsen number, Kn. However, we are interested in finding $\frac{1}{2\pi} \left. \frac{\partial^2 E_{diss}}{\partial A^2} \right|_{\omega=\omega_R}$, instead of E_{diss}, because this property does not depend upon A^2, allowing us to reduce the number of variables by one. Thus, we write the following expression for E_{diss}:

$$\frac{1}{2\pi} \left. \frac{\partial^2 E_{diss}}{\partial A^2} \right|_{\omega=\omega_R} = f\left(\rho_{gas}, L_0, \omega_R, \mu, \mathrm{Kn}\right), \tag{2.8}$$

where f is an undetermined function. We now use the Buckingham Pi theorem [11] to reduce the number of variables and to nondimensionalize Eq. 2.8. We begin by reformulating Equation 2.8:

$$g\left(\frac{1}{2\pi}\frac{\partial^2 E_{diss}}{\partial A^2}\bigg|_{\omega=\omega_R}, \rho_{gas}, L_0, \omega_R, \mu, \mathrm{Kn}\right) = 0, \tag{2.9}$$

where g is another undetermined function different from f. The Buckingham Pi theorem states that given a relationship of the form $g(x_1, x_2, ..., x_n) = 0$, the n parameters can be rewritten in terms of $n-m$ independent dimensionless parameters. m is usually the minimum number of dimensions required to specify the dimensions of the parameters. In this case, the dimensions required are mass, length, and time, which leads to $m = 3$ and $n - m = 3$. We form three independent dimensionless parameters:

$$\Pi = \frac{1}{\rho_{gas} L_0^3 \omega_R^2}\left(\frac{1}{2\pi}\frac{\partial^2 E_{diss}}{\partial A^2}\bigg|_{\omega=\omega_R}\right), \tag{2.10a}$$

$$\mathrm{Re} = \frac{\rho_{gas} L_0^2 \omega_R}{\eta}, \tag{2.10b}$$

$$\mathrm{Kn} = \frac{\lambda}{L_0}. \tag{2.10c}$$

Re is the Reynolds number. We now rewrite 2.8:

$$\Pi = \Omega\left(\mathrm{Re}, \mathrm{Kn}\right), \tag{2.11a}$$

$$\frac{1}{2\pi}\frac{\partial^2 E_{diss}}{\partial A^2}\bigg|_{\omega=\omega_R} = \rho_{gas} L_0^3 \omega_R^2 \Omega\left(\mathrm{Re}, \mathrm{Kn}\right). \tag{2.11b}$$

We use Eq. 2.7 to rewrite Eq. 2.11b in terms of Q.

$$k = \rho_{gas} L_0^3 \omega_R^2 \Omega\left(\mathrm{Re}, \mathrm{Kn}\right) Q \tag{2.12}$$

This equation is close to the desired result; however, there is still size dependence in k, the stiffness of the oscillator. We eliminate k from the equation. We note that $\rho_{av} L_0^3 \omega_{vac}^2 / k$, the ratio of the kinetic energy to potential energy, depends upon the

shape of the oscillator and not its size. ρ_{av} is the average density of the device and ω_{vac} is the resonant frequency in vacuum. We combine these results, yielding

$$Q = \frac{\rho_{av}\omega_{vac}^2}{\rho_{gas}\omega_R^2}\frac{1}{\Pi\left(\mathrm{Re},\mathrm{Kn}\right)}. \tag{2.13}$$

We next consider $\frac{\omega_{vac}}{\omega_R}$. Sader [12] has shown that for devices with Q$\gg$ 1, this ratio is approximately equal to 1. For these types of devices, the frequency shift due to viscous damping effects is negligible. We rewrite Eq. 2.13,

$$Q = \frac{\rho_{av}}{\rho_{gas}}\frac{1}{\Pi\left(\mathrm{Re},\mathrm{Kn}\right)} \tag{2.14}$$

We now have an expression for Q, in terms of Re and Kn.

We next determine the conditions required for the model and prototype flows to be similar. Following Fox et al. [11], the first condition is that the model and prototype are geometrically similar. They must be the same shape; all dimensions must be scaled by a constant scale factor between model and prototype. The second condition is that the flows must be kinematically similar. The velocities at corresponding points must have the same direction and only be different by a constant scale factor. The third and most restrictive condition is that the flows are dynamically similar. In this case, the force distributions are parallel and scaled by a constant factor at all points. To ensure dynamic similarity between the model and prototype flows, the governing dimensionless groups obtained from the Buckingham Pi theorem must have the same value for both flows.

At this point, it is unclear how many samples of (Kn, Re) pairs are required to experimentally determine $\Pi\left(\mathrm{Re},\mathrm{Kn}\right)$. We consider the product of ReKn:

$$\mathrm{ReKn} = \left(\frac{\rho_{gas}L_0^2\omega_R}{\mu}\right)\left(\frac{\lambda}{L_0}\right), \tag{2.15a}$$

$$\mathrm{ReKn} = \left(\frac{\rho_{gas}\lambda}{\mu}L_0\omega_{vac}\right)\frac{\omega_R}{\omega_{vac}}. \tag{2.15b}$$

$$\mathrm{ReKn} = \left(\frac{\rho_{gas}\lambda}{\mu}L_0\omega_{vac}\right) \tag{2.15c}$$

We have used $\frac{\omega_R}{\omega_{vac}} \approx 1$ to simplify the equation. $\rho_{gas}\lambda$ is independent of pressure.

$$\begin{aligned} \rho_{gas}\lambda &= \rho_{gas} \times \frac{1}{2^{1/2}\pi d_0^2 \rho_{gas}} \\ &= \frac{1}{2^{1/2}\pi d_0^2} \end{aligned} \tag{2.16}$$

$L_0\omega_{vac}$ is independent of the oscillator size. Thus, ReKn is a constant, independent of pressure or the critical dimension of the device. We do not need to explore the entire 2D phase space; for any given value of Kn, the value of Re is fixed. We rewrite the expression for Q in terms of Kn:

$$Q = \frac{\rho_{av}}{\rho_{gas}}\frac{1}{\Pi\,(\mathrm{Kn})} \tag{2.17}$$

We also remove the dependence on ρ_{av}, the density of the device, by rewriting Q in terms of G(Kn, a dimensionless function inversely proportional to $\Pi\,(\mathrm{Kn})\,\rho_0/\rho_{av}$, where ρ_0 is a normalization factor.

$$Q = \frac{\rho_0}{\rho}H(\mathrm{Kn}) \tag{2.18}$$

We now have an equation that will predict the quality factor of the model device based upon measurements on a scaled prototype device.

2.4 Device Fabrication

We fabricated a variety of devices with different shapes and aspect ratios to test the principle of dynamic similarity. We used 4” silicon wafers coated with either 100 nm, 300 nm, or 500 nm of low stress silicon nitride (SiN) on both sides to fabricate the devices. We scaled all dimensions of the device with thickness; the 300 nm devices had a length three times longer than the 100 nm devices and a width three times wider than the 100 nm devices. The 500 nm devices had a length five times longer than the 100 nm devices and a width five times wider than the 100

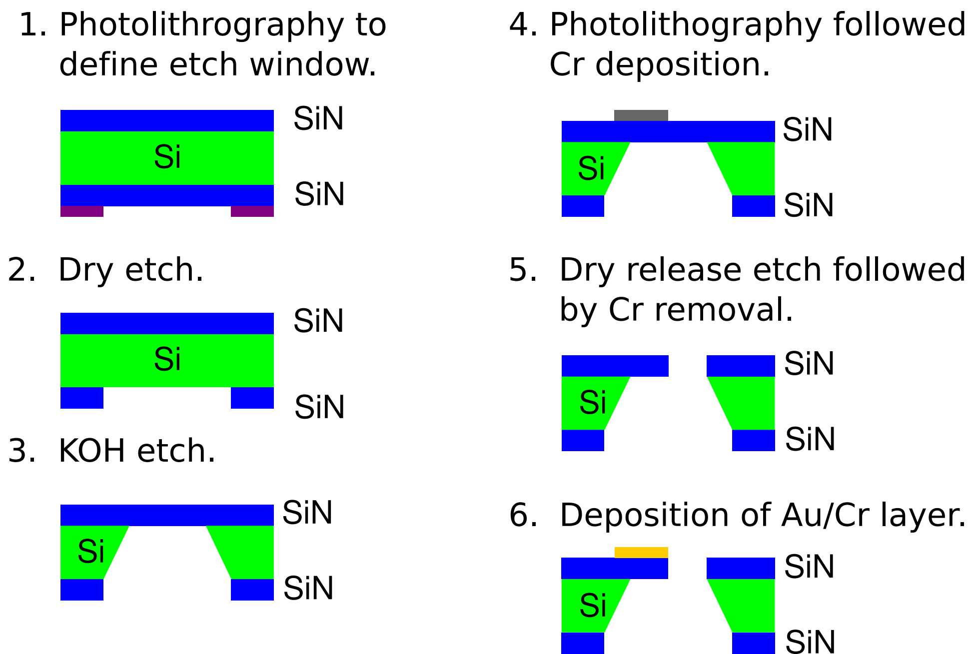

Figure 2.1: Device Fabrication

nm devices. We used photolithography to define etch windows on the backside of each wafer, followed by a dry etch to remove the SiN. We then used a KOH etch to remove the silicon from the selected areas to form SiN membranes on the front side of the wafer. We used electron beam lithography to define cantilevers along the edges of the membranes. We deposited either a layer of Cr or a Cr/Au layer as an etch mask. We dry etched the silicon nitride membranes to define the cantilevers. We then removed the metal layer(s) with a wet etch. All of the devices were then coated with a Cr/Au bilayer for reflectivity; the Cr layer served as an adhesion layer for the Au layer. A thermal evaporator was used for the 100nm and 500nm devices, while an electron beam evaporator was used for the 300nm devices. Prior to deposition of the metal layer on the devices, we performed a test deposition on a SiN coated SOI wafer; the wafer had been patterned with rectangles using photolithography. After liftoff, we measured the step height of the bilayer rectangles with an atomic force microscope. We used the step height to calibrate the subsequent metal deposition on the devices. The 500nm devices had a 3nm

layer of Cr with a 100-110nm thick layer of Au on top. The 300nm devices had a 3nm layer of Cr with a 60-66nm layer of Au on top. The 100nm devices had a 3nm layer of Cr with a 20-22nm layer of Au on top. The reflective layer was not deposited prior to the etch of the SiN membrane because the etch would have also etched the Au, leaving a layer of unknown thickness. The thickness of the metal layers must be within 10% of the desired thickness to ensure geometric similarity between the devices and to ensure that the density of the devices remains constant. Colorized SEM images of the 100nm set of devices are shown in Figure 2.2. As shown in Figure 2.2, we fabricated six types of devices. On Die A, we fabricated three rectangular cantilevers with differing aspect ratios (length:width): 10:1, 5:1, and 10:3. Each device had a different Knudsen number at the same pressure. On Die C, we fabricated three cantilevers of various shapes: a square paddle head cantilever, a triangular cantilever, and a cantilever with legs. The square paddle head cantilever is often used for torsional sensing applications, such as torsional magnetometry used for gas sensing [13]. The triangular cantilever shape is used in AFM measurements that require torsional and lateral stability, such as contact AFM imaging [14]. The cantilever with legs is often used in gas sensing measurements [2], since the legs allow piezoresitive detection of the cantilever motion.

2.5 Experimental Setup

An overview of the experimental setup is shown in Figure 2.3. We used optical interferometry to measure the quality factors of the devices with both a network analyzer and a spectrum analyzer. For the network analyzer measurements, we used a piezoelectric shaker to actuate the cantilevers. We placed the devices in a vacuum chamber and measured the quality factor over a range of pressures, from 3mT to 760T.

A schematic of the optical interferometry setup is shown in Figure 2.4. The simple

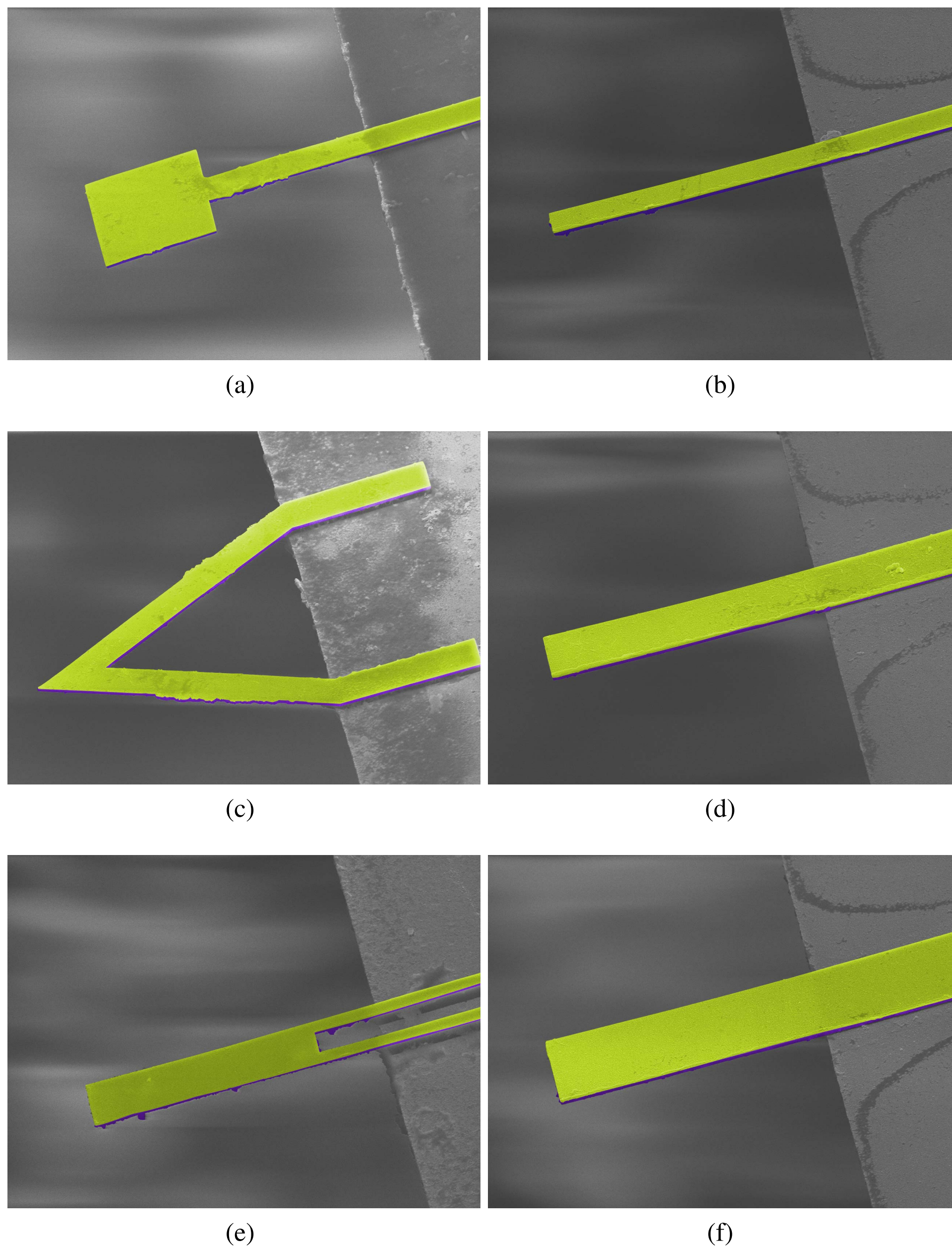

Figure 2.2: Colorized images of 100 nm devices, with L=10μm. Yellow is gold; purple is SiN. All images are taken at 7500x magnification. (a)Square paddle head cantilever. (b)L:w=10:1 cantilever. (c)Triangular cantilever. (d)L:w=5:1 cantilever. (e)Cantilever with legs. (f)L:w=10:3 cantilever.

interferometer is very similar to the design used by Rugar et al. [15]. The first component of the detection system is the laser. We used an amplitude stabilized HeNe laser to minimize fluctuations in the beam intensity. Fluctuations in the

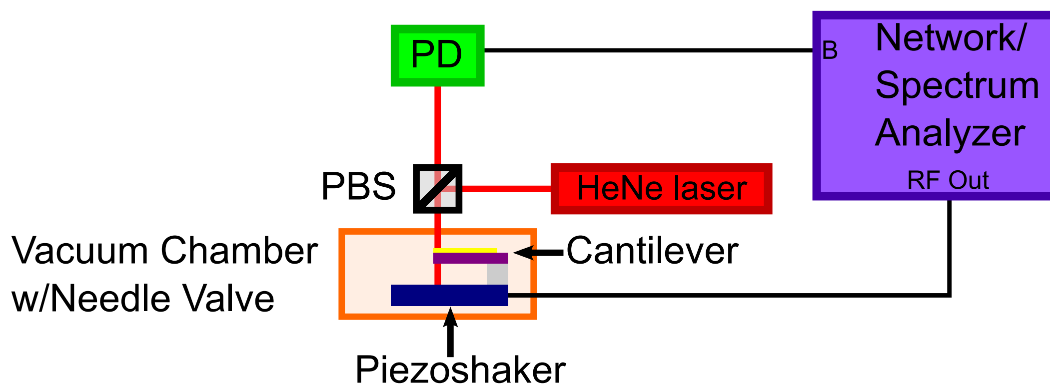

Figure 2.3: Experimental setup for measurements of device quality factor vs pressure. The cantilever is in a vacuum chamber with a needle valve used to control the pressure. The cantilever is mounted on a piezoelectric shaker. The optical interferometery setup has been simplified to the key components: the HeNe laser, the beam splitter (PBS), and the photodetector (PD) used to detect the motion. The network analyzer outputs a drive signal on RF out; it measures the signal from the PD on B. The spectrum analyzer measures the signal from the PD on B as well.

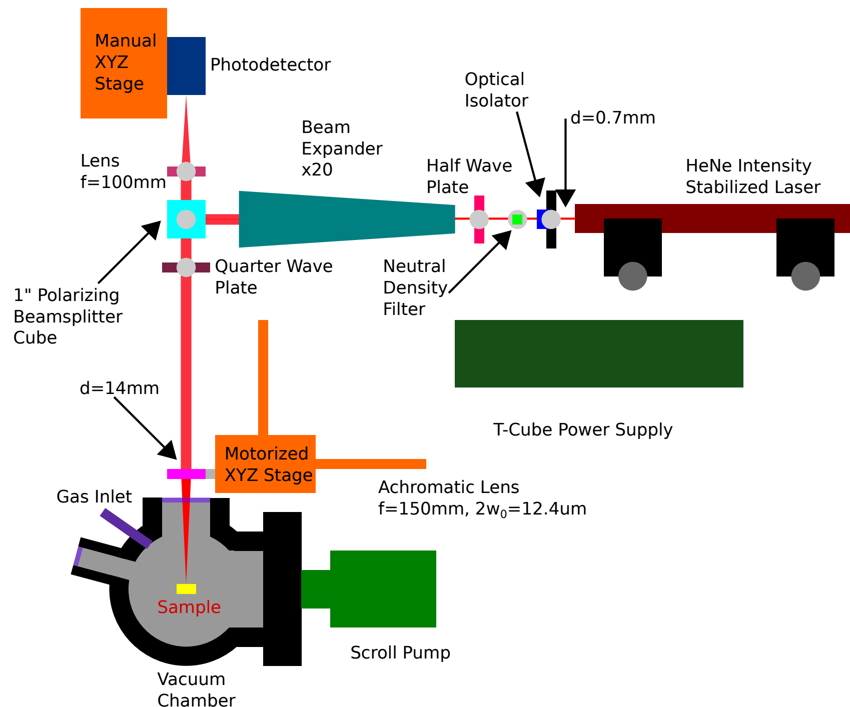

Figure 2.4: Optical Setup

intensity of the laser are indistinguishable from fluctuations caused by a change in the path length; consequently, amplitude stabilization reduces the displacement noise floor for the measurement. Following the laser is an optical isolator, which prevents any light reflected from components further along the beam path from entering the laser; the reflected light could destabilize the laser. The next component is a half wave plate in a rotation mount; the polarization is adjusted for the maximum amount of light to enter the interferometer. Following the half wave plate is a neutral density filter, used to attenuate the beam power. We used a ND=1.5 filter while making measurement for the 500nm and 300nm devices and a ND=1.0 filter while making measurements for the 100nm devices. We chose these levels of attenuation to limit heating of the device under measurement, in order to prevent drift in the resonant frequency. We determined these power levels by increasing the attenuation from the neutral density filter and measuring the resonant frequency. The speed of sound, $c_s = \sqrt{E/\rho}$, is temperature dependent, which leads to the temperature dependency of the resonant frequency. We increased the attenuation until the resonant frequency no longer shifted with an increase in attenuation. A 20x beam expander follows. When the beam exits the laser, it has a $1/e^2$ diameter of 0.7mm. The 20x beam expander increases the $1/e^2$ diameter to 14mm; the beam expander is required to minimize the spot size at the sample. The minimum spot size at the sample, $2w_0$, is set by the diffraction limit. The minimum spot size is given in Eq. 2.19 [16]:

$$2w_0 = 1.83\frac{f\lambda}{D}, \tag{2.19}$$

where f is the focal length of the lens, λ is the wavelength of light, and D is the diameter of the input beam. Due to constraints on the diameter of the vacuum chamber, the minimum focal length of the lens is 150mm, which corresponds to a spot size of 12.4μm at the sample.

The next component in the optical setup is the polarizing beam splitter (PBS) cube.

The PBS splits the beam into its two orthogonal polarization components. The PBS also prevents ghost reflections, which would occur with a plate beam splitter. Following the PBS is a quarter wave plate in a rotation mount; the quarter wave plate is required to rotate the polarization of the beam by 90° so that the beam reflected from the sample is directed to the photodetector. The light is then focused through an achromatic lens mounted in a kinematic mirror mount on a motorized XYZ stage. We have chosen an achromatic lens to reduce aberrations in the beam. The lens is also chosen to ensure the highest numerical aperture possible. The XYZ stage is used to move the beam along the device during alignment.

The beam then enters the vacuum chamber through a quartz window with an anti-reflective coating. A portion of the beam hits the device and is reflected back along the optical path until it reaches the PBS, where it is directed to the photodetector. The remainder of the beam is reflected by the piezoshaker underneath the chip containing the cantilevers. Prior to entering the photodetector, the beam traverses a lens with a focal length of 100mm, to reduce the beam size, since the diameter of the active area of the photodetector is 0.8mm. The photodetector used is a New Focus 1801 photodetector, which has a bandwidth of DC-125MHz and a noise floor of 3.3 $\mathrm{pW}/\sqrt{\mathrm{Hz}}$. The photodetector is mounted on an XYZ translation stage for alignment with the beam. The noise floor is set by the shot noise on the detector and the device responsivity.

2.6 Measurements

We measured the quality factors of the devices over a range of pressures. We measured two quantities: the intrinsic quality factor of the devices and the quality factor due to gas damping. We used the optical setup to detect the motion of the devices and a piezoshaker to actuate them. We mounted a piezoshaker with silver paste onto a PCB and then mounted the chip containing the cantilevers to the

piezoshaker with superglue. We then wire bonded the piezoshaker to the PCB. We placed the device in a vacuum chamber pumped with a scroll pump with a base pressure of $\approx$ 3 mTorr. We varied the pressure in the chamber by adding N_2 gas through a needle valve attached to the chamber; the pump was separated from the chamber by a valve. We measured the pressure with a MKS 317 Pirani gauge, accurate to 1% of the indicated decade, with two digits of precision.

We measured the intrinsic Q of each device at a few mTorr with an Agilent 4395A Network/Spectrum/Impedance Analyzer in network analyzer mode. We drove the devices with the piezoshaker and measured the photodetector output. We used a network analyzer to measure the intrinsic Q because measurements of the thermomechanical noise spectrum with the 4395A in spectrum analyzer mode had a variance of about 10%-15% of the measured Q. Such inconsistent measurements would require several (about 10) measurements to acquire an accurate value for Q. An accurate value for the quality factor is required to convert from the measured Q to the Q due to gas damping. The measurements made with the network analyzer had a variance of less than 1%, leading to significantly faster measurements. We fitted the resonance peak to the expected response of a simple damped harmonic oscillator using a non-linear least squares fit in MATLAB.

However, we were unable to use the network analyzer (NA) to make the pressure vs Q measurements because laser noise and the response of the piezoshaker at higher pressures altered the shape of the response, rendering it no longer a Lorentzian. The thermomechanical noise spectrum measured with the spectrum analyzer (SA) was always Lorentzian, occasionally with peaks from the laser noise present. The laser noise is present even when the beam splitter is replaced with a mirror to directly send the beam to the photodetector. The laser has noise peaks at the following frequencies in kHz: 36.7, 73.3, 110, 147, 183, 220, 257, 293, 330, 367, 403, 440, 477. A fast Fourier transform of a ring down measurement collected with an

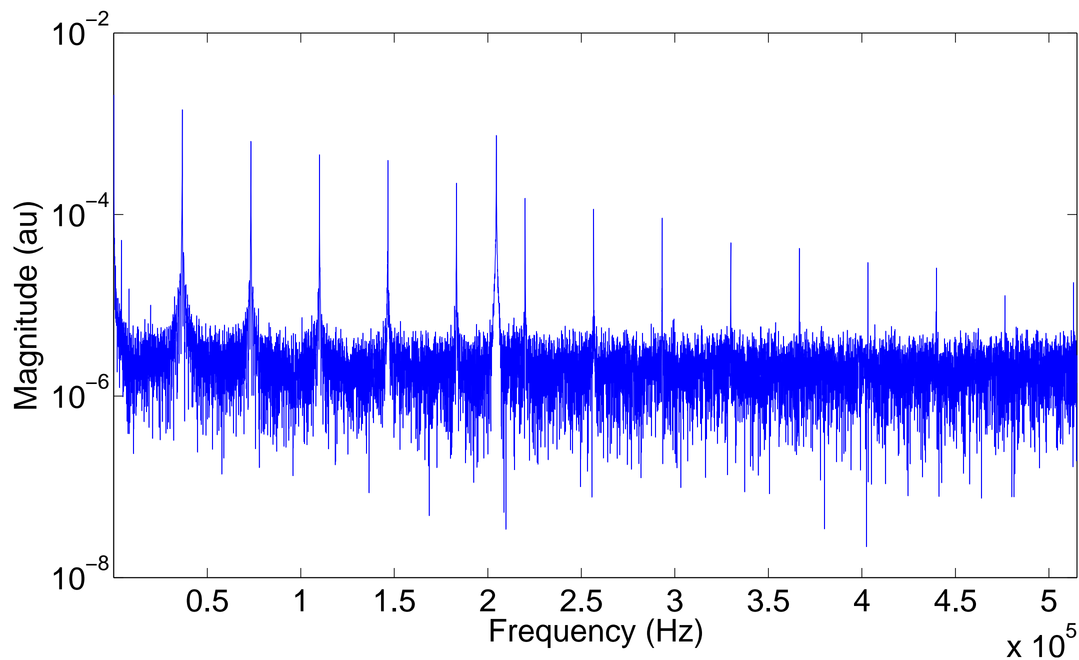

Figure 2.5: Frequency spectrum of laser noise. The peak at 204.6kHz corresponds to the resonant frequency of the device.

Agilent 54845A oscilloscope for a cantilever with a resonant frequency of 204.6kHz is shown in Figure 2.5; the laser noise peaks are clearly visible. We could easily remove the peaks from the laser noise during the fitting of the thermomechanical noise spectrum. The thermomechanical displacement noise spectral density for a cantilever is given by Eq. 2.20 [17].

$$S_x^{th}(\omega) = \frac{\omega_0}{(\omega_0^2 - \omega^2)^2 + (\omega_0\omega/Q)^2} \frac{4k_BT}{M_{eff}Q}, \tag{2.20}$$

where ω_0 is the resonant frequency of the cantilever, Q is the quality factor, k_B is Boltzmann's constant, T is the temperature, and M_{eff} is the effective mass of the cantilever. For a cantilever with an aspect ratio $(L/b) > 3$, $M_{eff} \approx 0.24M$ [18]. Shown in Figure 2.6 is the thermomechanical noise peak for 500nm Die A Device #1.1 at P=3.7 mTorr. Figure 2.7a shows pressure vs quality factor for a measurement run. Figure 2.7b shows ω_R/ω_{vac} for these devices, where ω_{vac} is the

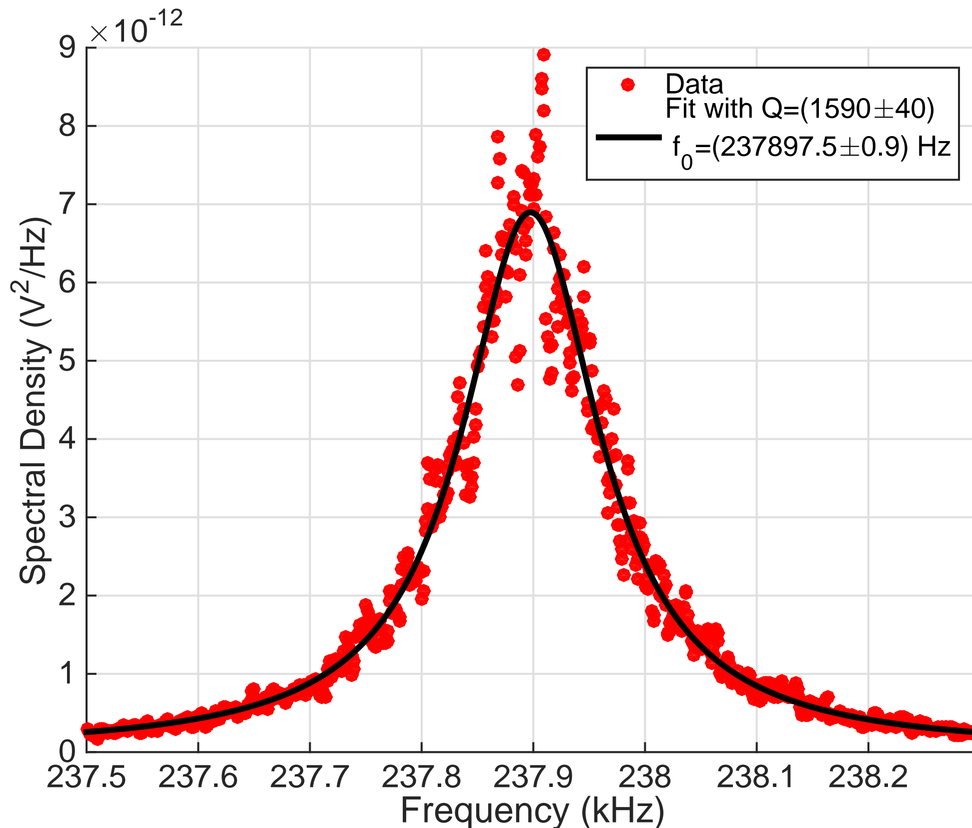

Figure 2.6: Thermomechanical noise peak.

resonant frequency measured at the lowest pressure. $\omega_R/\omega_{vac} \approx 1$, validating our earlier assumption.

We fitted the thermomechanical noise peak to Eq. 2.20 using a non-linear least squares fit in MATLAB. We measured pressure vs Q for each device with the spectrum analyzer, with three measurements below 10 mTorr. The rest of the measurements were logarithmically spaced for four measurements each decade, with the exception of 100 Torr-1000 Torr; the measurement was terminated at 760 Torr. For the 500nm devices, a measurement was made at 150 Torr instead of 170 Torr to enable comparison with the quality factor of the 100nm devices at 760 Torr. For the 300nm devices, an additional measurement was made at 250 Torr for the same reason. We plotted pressure vs measured quality factor for each

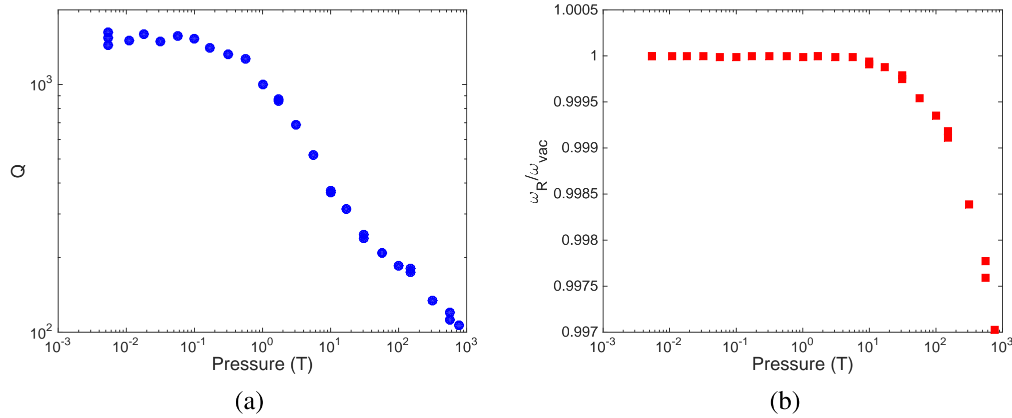

Figure 2.7: Data for measurement run #3.1 on 500 nm 10:1 aspect ratio device. (a) Pressure vs quality factor. (b) Pressure vs ω_R/ω_{vac}.

device in Figures 2.8-2.13. For each thickness and device shape, we performed the measurement on two devices. We performed each measurement on each device twice. In the figures, each device is labeled by device thickness (100nm, 300nm, or 500nm), position on the wafer (#1-#6), and measurement run (#x.1 or #x.2). We group the measurements by either aspect ratio for the Die A devices or shape for the Die C devices. For these measurements, the uncertainty in the measurement is smaller than the markers used to display the data.

2.7 Analysis

We wish to validate the dynamic similarity by used the measurements on the 300 nm and 500 nm devices to predict the quality factor of the 100 nm devices at atmosphere, which corresponds to a pressure of 760 Torr. We rewrite Equation 2.18 in terms of gas pressure, instead of gas density, and the measured quality factor due to gas damping, $Q_{GAS}(\text{Kn})$, as given by Equation 2.22.

$$Q_{scaled}(\text{Kn}) = \frac{P}{760\text{Torr}} Q_{GAS}(\text{Kn}), \tag{2.21}$$

where P is the pressure.

$$Q_{GAS}(P) = \left[\frac{1}{Q(P)} - \frac{1}{Q_0}\right]^{-1}, \tag{2.22}$$

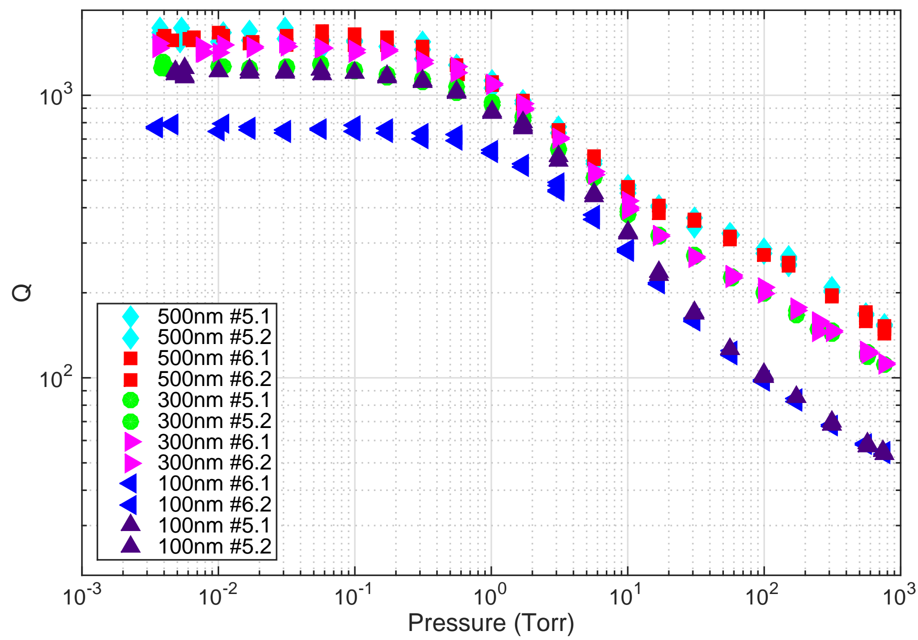

Figure 2.8: Plot of Pressure vs Q for Die A Cantilevers with Aspect Ratio 10:3

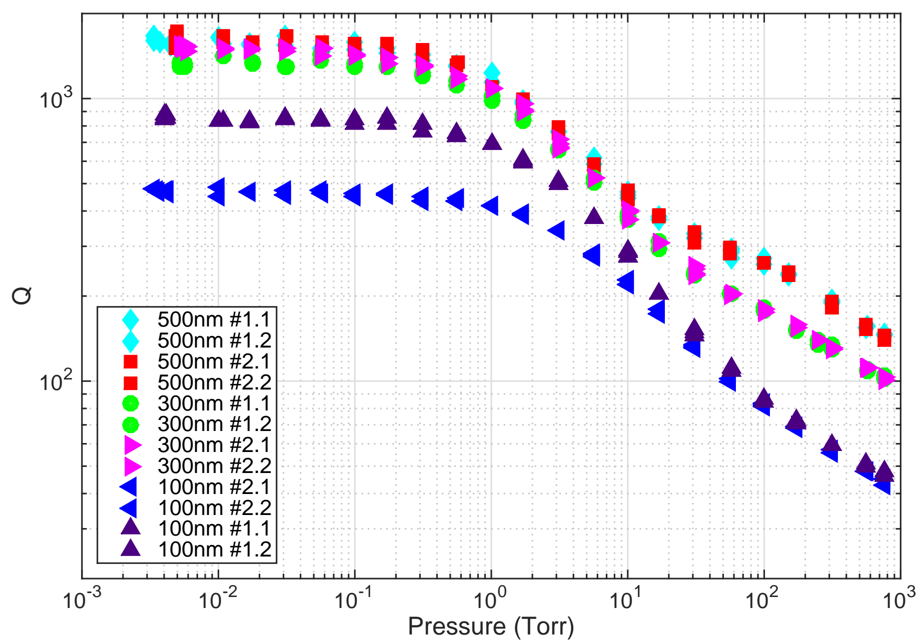

Figure 2.9: Plot of Pressure vs Q for Die A Cantilevers with Aspect Ratio 5:1

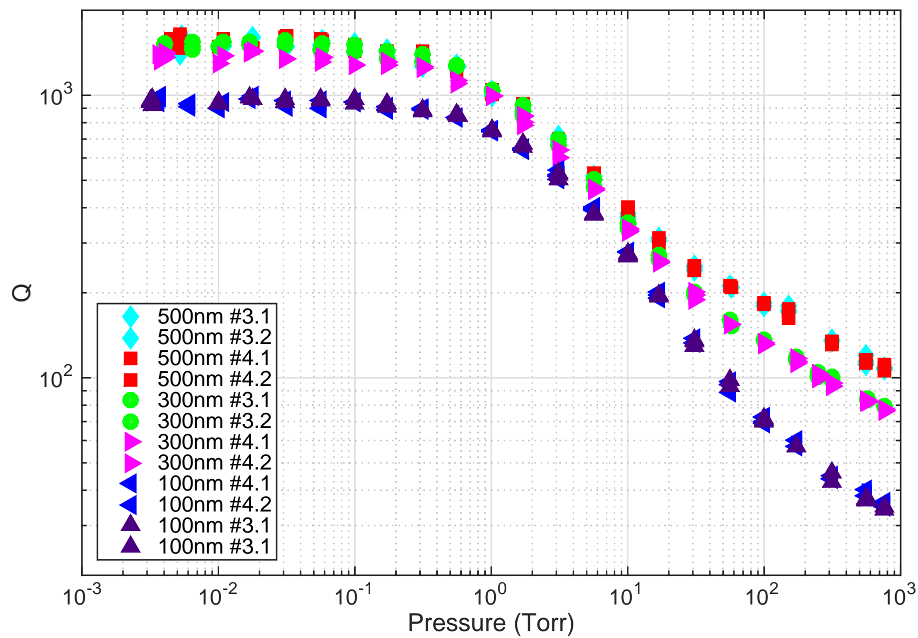

Figure 2.10: Plot of Pressure vs Q for Die A Cantilevers with Aspect Ratio 10:1

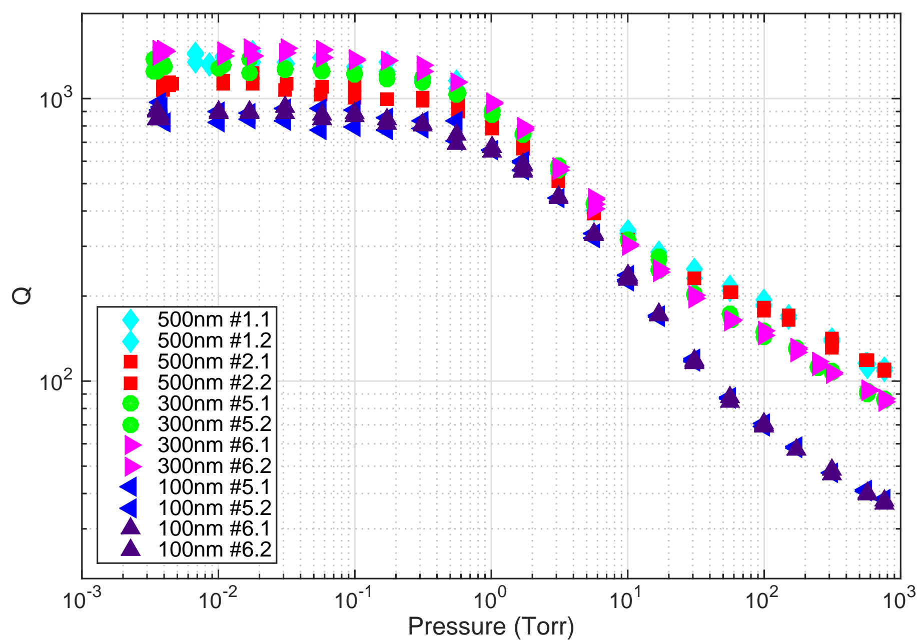

Figure 2.11: Plot of Pressure vs Q for Die C Cantilevers with Legs

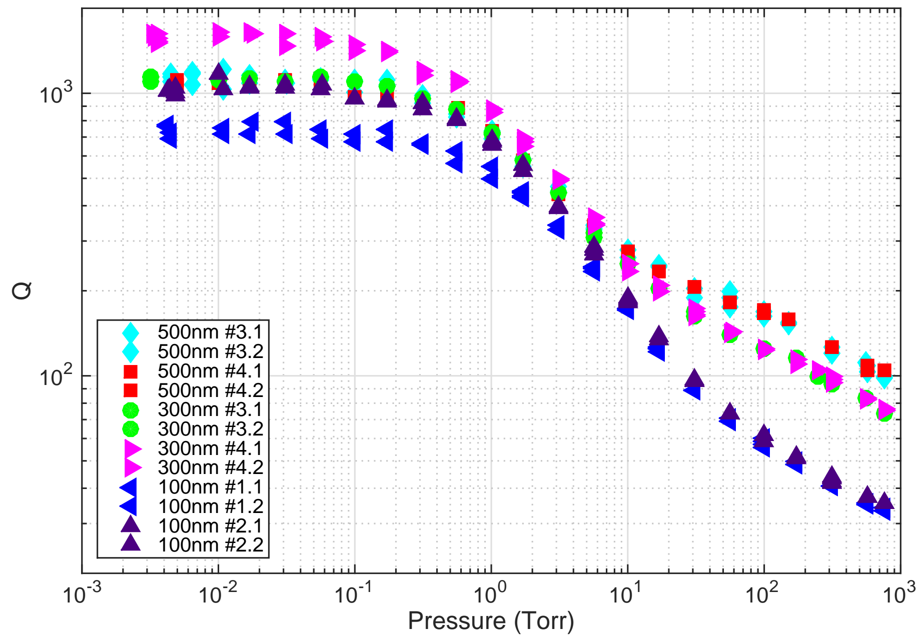

Figure 2.12: Plot of Pressure vs Q for Die C Square Headed Cantilevers

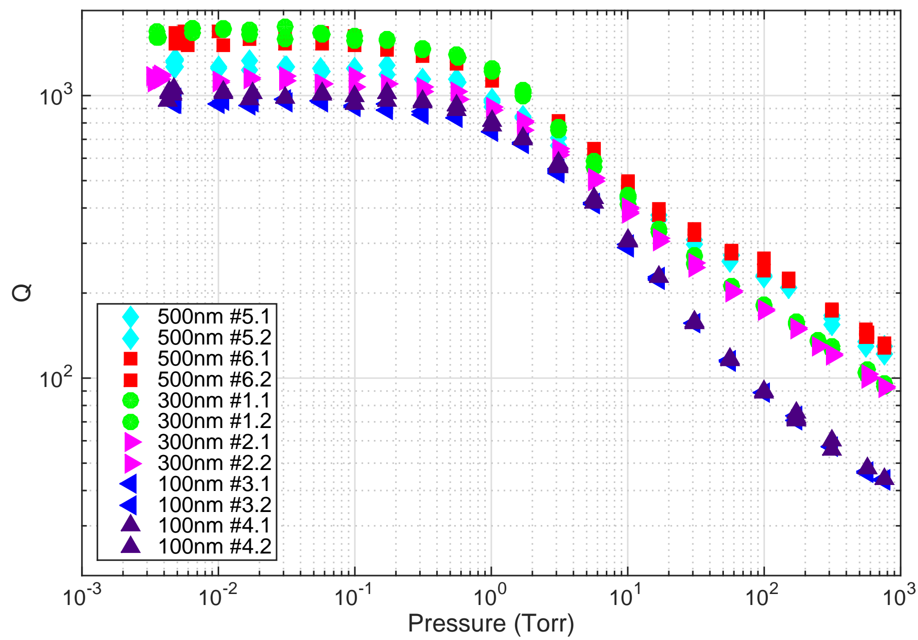

Figure 2.13: Plot of Pressure vs Q for Die C Triangular Cantilevers

where Q is the quality factor measured at P and Q_0 is the intrinsic quality factor of the device. The scaled quality factor, Q_{scaled} provides the predicted quality factor for the 100 nm devices from the 300 nm and 500 nm devices. We chose a reference of 760 Torr because we wish to predict the quality factor of the devices at 760 Torr. We then plotted the data in terms of Kn vs Q_{scaled}, which are shown in Figures 2.14-2.19.

The Die A plots, Figures 2.14-2.16, also show the free molecular flow estimate for the quality factor due to gas damping, Q_{FMF}, as a solid black line and the continuum theory estimate for the quality factor due to gas damping, Q_{Visc}, as a dashed black line. We used the parameters for one of the 500 nm devices to calculate the estimates for both flow regimes and plot both estimates in terms of the corresponding scaled quality factor. We used the parameters of the 500 nm devices to estimate the scaled quality factor in order to verify the dynamic similarity principle; if the dynamic similarity principle holds, the data from all of the devices should fall along the asymptotes for estimate of the scaled quality factor for the 500 nm device.

The quality factor in the free molecular flow regime is given in Eq. 2.23 [19]:

$$Q_{FMF} = \frac{K(\epsilon)\rho_{dev}t\omega_{vac}}{P} \times \left(\frac{2R_0T}{M_0}\right)^{1/2}, \tag{2.23}$$

where R_0 is the gas constant, 8314J-(kg-mole-K)$^{-1}$, T is the temperature in K, M_0 is the molar mass of N_2 gas in kg/mol, ρ_{dev} is the density of the device, and t is the thickness of the device. $K(\epsilon) = \sqrt{\pi}/(4 + \pi + [4 - \pi]\epsilon)$, where ϵ is the coefficient of specular reflection at the surface of the cantilever. $\epsilon = 1$ corresponds to specular reflection and $\epsilon = 0$ corresponds to diffuse reflection. For the simulation, we use $\epsilon = 0$, which provides the best fit to the data. For the continuum flow regime, the quality factor is given by Eq. 2.24 [12].

$$Q_{Visc} = \frac{\frac{4\mu}{\pi\rho_{gas}b^2} + \Gamma_r(\omega_R)}{\Gamma_i(\omega_R)}, \tag{2.24}$$

where μ is the mass per length of the cantilever, ρ_{gas} is the density of the gas surrounding the cantilever, $\Gamma_r(\omega)$ is the real part of the hydrodynamic function, $\Gamma_i(\omega)$ is the imaginary part of the hydrodynamic function, and ω_R is the resonant frequency of the cantilever in the absence of dissipation. For $Q >> 1$, $\omega_R \approx \omega_0$.

For a cantilever with a circular cross-section, the hydrodynamic function has an exact analytic result [12], given in Eq. 2.25:

$$\Gamma_{circ}(\omega) = 1 + \frac{4iK_1\left(-i\sqrt{i\text{Re}}\right)}{\sqrt{i\text{Re}}K_0\left(-i\sqrt{i\text{Re}}\right)}, \tag{2.25}$$

where K_i are modified Bessel functions of the second kind and Re is the Reynolds number. For a cantilever of width b and radial resonant frequency ω_R, the Reynolds number is given by Eq. 2.26 [12].

$$\text{Re} = \frac{\rho_g \omega_R b^2}{4\eta}, \tag{2.26}$$

where η is the viscosity of the gas. For N_2, η=16.58μP-s [9]. For Re $\in \left[10^{-6}, 10^{4}\right]$, we can approximate the hydrodynamic function for a rectangular cantilever, $\Gamma_{rect}(\omega)$, to within 0.1% using the expressions in Eq. 2.27 [12]:

$$\Gamma_{rect}(\omega) = \Omega(\omega)\,\Gamma_{circ}(\omega), \tag{2.27a}$$

$$\begin{aligned}\Omega_r(\omega) = &\left(0.91324 - 0.48274\tau + 0.46842\tau^2\right.\\ &\left.-0.12886\tau^3 + 0.044055\tau^4 - 0.0035117\tau^5 + 0.00069085\tau^6\right)\\ &\times\left(1 - 0.56964\tau + 0.48690\tau^2 - 0.13444\tau^3\right.\\ &\left.+0.045155\tau^4 - 0.0035862\tau^5 + 0.00069085\tau^6\right)^{-1}\end{aligned} \tag{2.27b}$$

$$\begin{aligned}\Omega_i(\omega) = &\left(-0.024134 - 0.029256\tau + 0.016294\tau^2\right.\\ &\left.-0.00010961\tau^3 + 0.000064577\tau^4 - 0.000044510\tau^5\right)\\ &\times\left(1 - 0.59702\tau + 0.55182\tau^2 - 0.18357\tau^3\right.\\ &\left.+0.079156\tau^4 - 0.014369\tau^5 + 0.0028361\tau^6\right)^{-1},\end{aligned} \tag{2.27c}$$

$$\tau = \log_{10} \mathrm{Re}. \tag{2.27d}$$

We now combine Equations 2.24, 2.25, and 2.27 to numerically evaluate the quality factor due to gas damping for a given rectangular cantilever. We use the expression in Eq. 2.23 to calculate Q_{FMF} for Kn>1 and combine Equations 2.24, 2.25, and 2.27 to calculate Q_{Visc} for Kn $<$ 1.

In Figures 2.14-2.16, the data for all devices is in reasonable agreement with the predicted asymptotes in the free molecular flow regime and in the viscous flow regime. The majority of the data is within one to two standard deviations of the predicted value. There is more variation in the data at large Kn values due to the subtraction process used to calculate Q_{scaled}, as well as the fluctuations in the measurement of the quality factor made with the spectrum analyzer. For the data at small Kn values, the error bars on the data are smaller than the markers used to plot the data. In addition, for each of the devices, the majority of the data is within one standard deviation of the line defined by $Q_{scaled}(\mathrm{Kn})$ validating the dynamic similarity principle as applied to NEMS.

We also validate the dynamic similarity by comparing the measured value of Q for each 100 nm thick device at 760 Torr with the values predicted by the 300 nm and 500 nm thick devices. These measurements correspond to Knudsen numbers between 0.1 and 0.01, depending upon the width of the 100nm device. We provide the measured values for Q at P_0=760 Torr for the 100 nm Die A devices in Table 2.1, in the row labeled 100 nm. We provide the value for Q at P_0 for the 100 nm thick device predicted by the measurement of Q at $P_0/3 \approx 250T$ for the 300 nm thick device in the row labeled 300nm. We provide the value for Q at P_0 for the 100 nm thick device predicted by the measurement of Q at $P_0/5 \approx 150T$ for the 500 nm thick device in the row labeled 500 nm. The columns contain the data for each aspect ratio. The data for each device shape from Die C is similarly presented in Table 2.2.

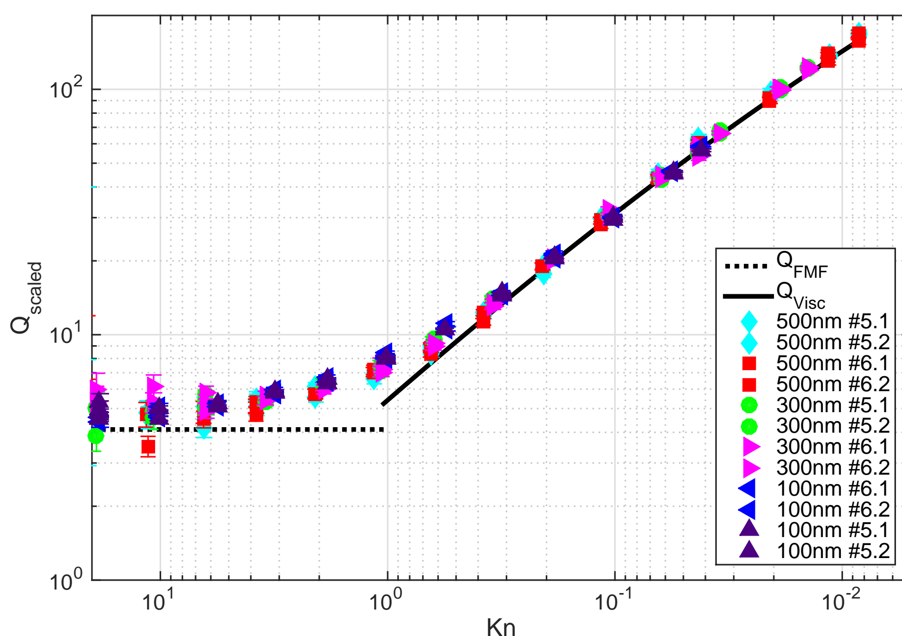

Figure 2.14: Plot of Kn vs Q_{SCALED} for Die A Cantilevers with Aspect Ratio 10:3

In each case, the predicted values are roughly within 10% of the measured value.

Die A			
Scaling	10:3	5:1	10:1
Thickness	Q		
100 nm	58	49	36
300 nm	56	50	36
500 nm	60	55	38

Table 2.1: Measured and predicted quality factors due to gas damping for Die A devices. Each column corresponds to a different aspect ratio.

Die C			
Type	Cantilever	Square Head	Triangular
Thickness	Q		
100 nm	39	36	46
300 nm	41	36	48
500 nm	38	36	50

Table 2.2: Measured and predicted quality factors due to gas damping for Die C devices. Each column corresponds a different device shape.

2.8 Conclusion

We demonstrate that the dynamic similarity principle accurately predicts nanoscale flows, obviating the need for complex and time consuming numerical simulation

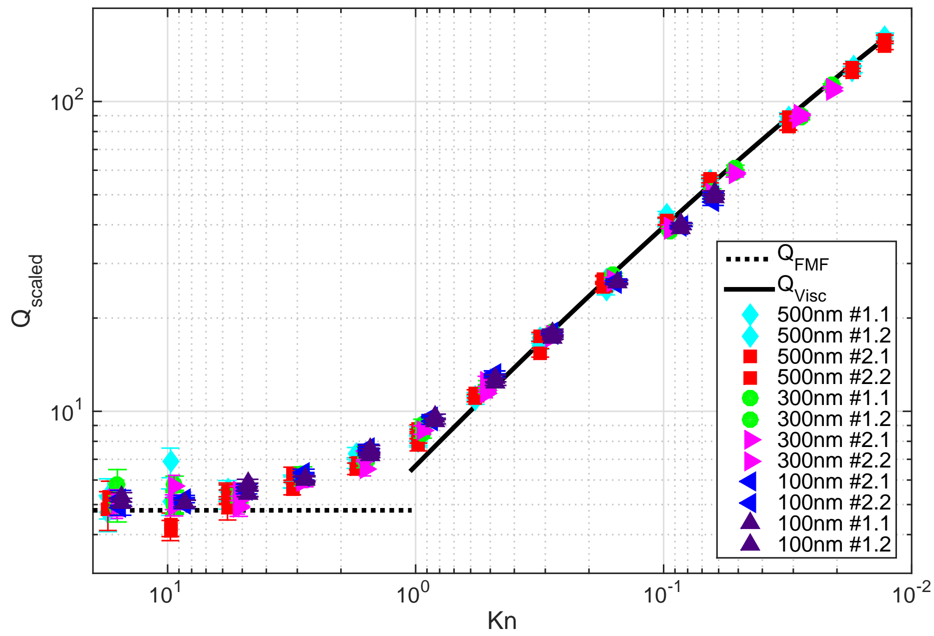

Figure 2.15: Plot of Kn vs Q_{SCALED} for Die A Cantilevers with Aspect Ratio 5:1

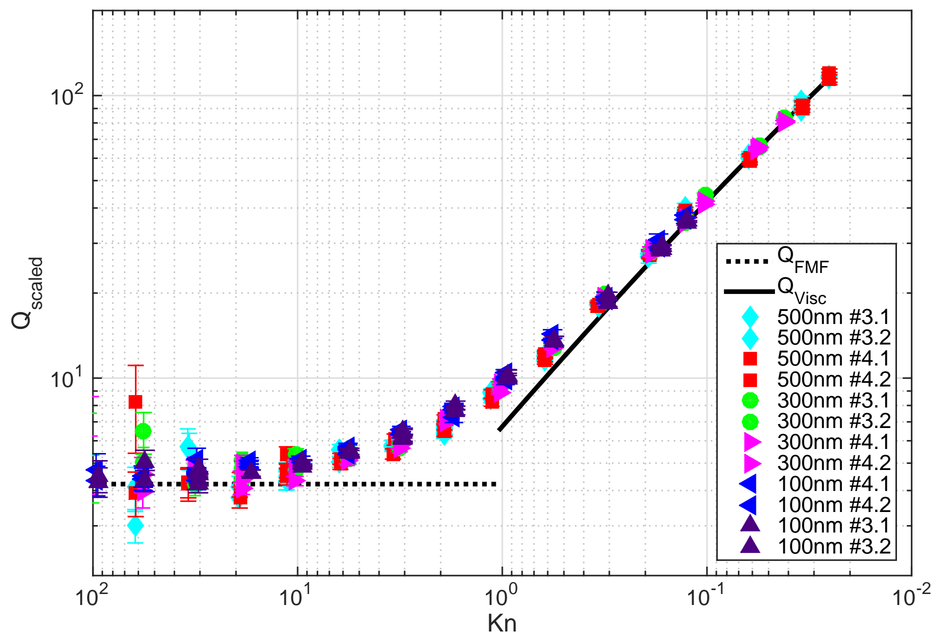

Figure 2.16: Plot of Kn vs Q_{SCALED} for Die A Cantilevers with Aspect Ratio 10:1

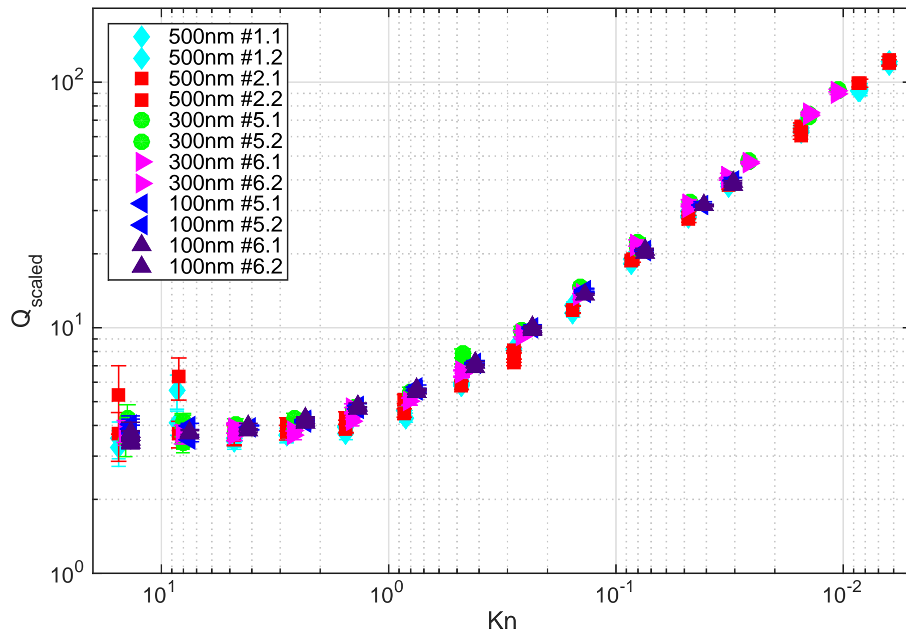

Figure 2.17: Plot of Kn vs Q_{SCALED} for Die C Cantilevers with Legs

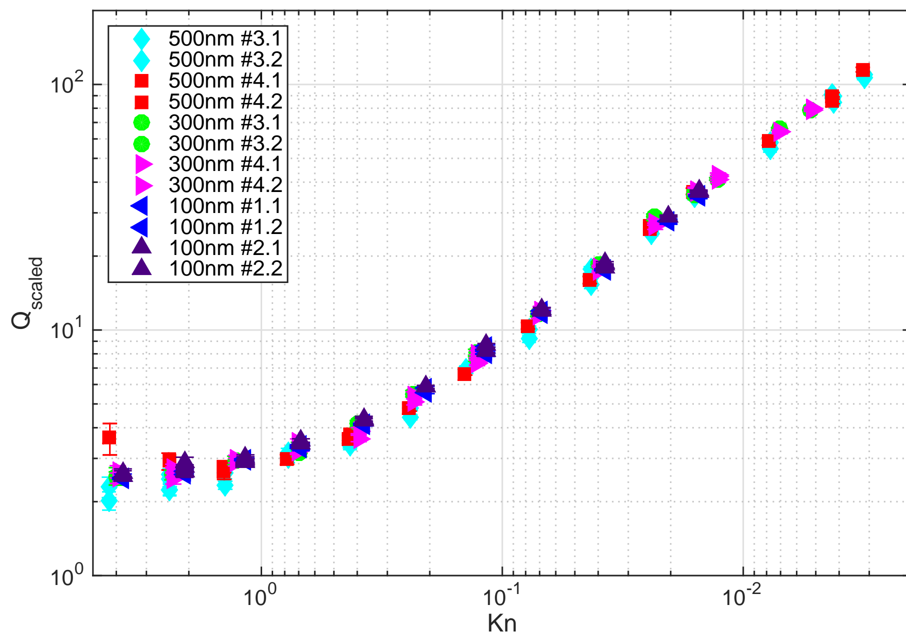

Figure 2.18: Plot of Kn vs Q_{SCALED} for Die C Square Headed Cantilevers

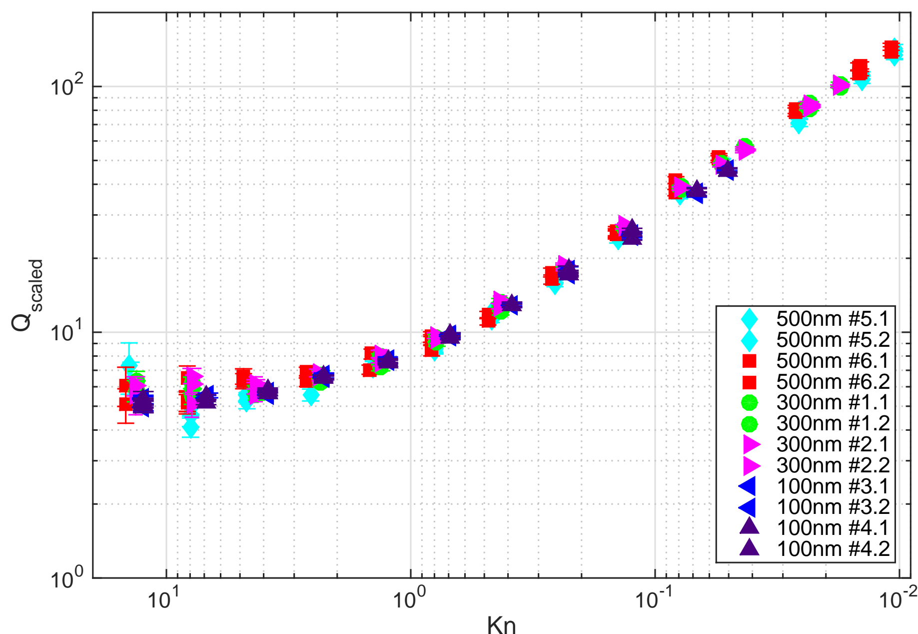

Figure 2.19: Plot of Kn vs Q_{SCALED} for Die C Triangular Cantilevers

to predict the quality factor of nanoscale devices. We have applied the dynamic similarity principle to accurately predict the quality factor of 100nm thick devices, from measurements made on scaled prototype devices, as shown in Tables 2.1 and 2.2. As shown in Figures 2.14-2.16, the quality factors measured agree reasonable well with the quality factor predicted by the analytical expression for the quality factor in the free molecular flow regime and the viscous damping regime. Thus, we have demonstrated that the dynamic similarity principle accurately describes the variations of the quality factor due to gas damping for a wide range of devices of various shapes and aspect ratios.

Chapter 3

PHASE NOISE IN OSCILLATORS

Among their many applications, NEMS and MEMS are employed as frequency shift sensors and as frequency sources. Specifically, they are used as frequency shift sensors in applications such as magnetic resonance force microscopy (MRFM) [20], NEMS gas chromatography [21], and NEMS mass spectrometry [4]. They are also used as frequency sources in timing applications [22–24] and communications [25]. For frequency shift sensors and for oscillators, the principle figure of merit is the frequency stability of the device. The theoretical limit to frequency stability is set by thermomechanical noise, or ultimately, quantum fluctuations for nanomechanical resonators. However, the frequency stability is currently limited by an unknown noise source in the mechanical domain, which we refer to as anomalous phase noise (APN). Anomalous phase noise has been observed by many researchers in a wide variety of MEMS and NEMS [26–34].

In this chapter, we begin with an overview of oscillators. We discuss the methods used to characterize noise in oscillators: amplitude noise, phase noise, fractional frequency noise, and Allan deviation. We compare the two measurement techniques used to quantify phase noise: open loop measurements and closed loop measurements. We discuss the frequency dependence of various physical noise sources. We also discuss the power law dependence of various phase noise sources and link them to noise sources in the oscillator feedback loop and the NEMS or MEMS resonator. We end with a discussion of the current state of our knowledge of APN.

3.1 Overview of Oscillators

In this section, we provide an overview of oscillators and the effects of phase and frequency fluctuations on the oscillator. Following Rubiola [35], an oscillator delivers a periodic signal. We model the oscillator as a loop composed of a lossy resonator with a transfer function $H(j\omega)$ and an amplifier with gain A, as shown in Figure 3.1. The resonator has a resonant frequency of Ω_0; we choose to operate the

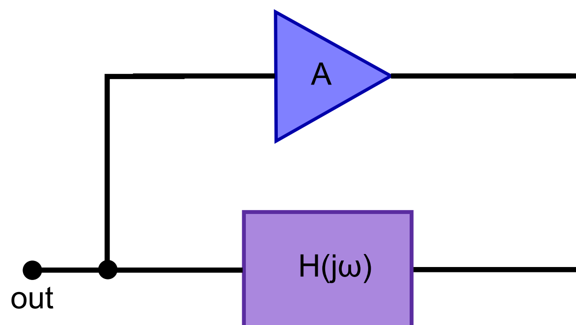

Figure 3.1: Diagram of a feedback oscillator.

oscillator at Ω_0. The feedback conditions required for the resonator to oscillate are given by the Barkhausen condition:

$$|AH(j\omega)| = 1, \tag{3.1a}$$

$$\arg AH(j\omega) = 0. \tag{3.1b}$$

In order to determine the effect of noise on the oscillator, we first consider an ideal oscillator and then add amplitude and phase fluctuations and find the resulting noise. An ideal oscillator delivers a signal $v(t) = V_0 \cos(\Omega_0 t + \phi)$, where V_0 is the peak amplitude, $\Omega_0 = 2\pi f_0$ is the resonant frequency, and ϕ is the phase shift, as well as higher order harmonics of Ω_0. For an ideal oscillator, we choose $\phi = 0$. A real oscillator has fluctuations in both the amplitude and the phase of the signal. Figure 3.2 demonstrates the case of either phase noise or amplitude noise in the signal $v(t)$. We modify our equation for $v(t)$ to include these two noise sources.

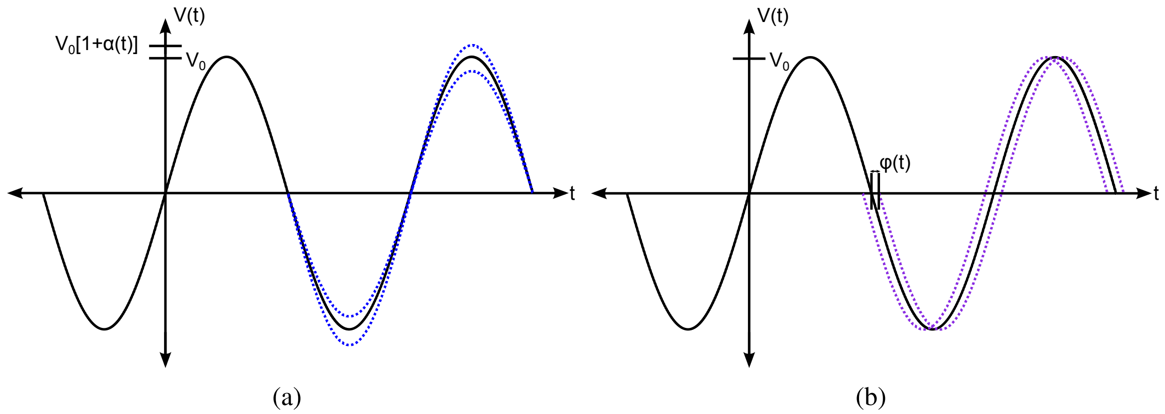

Figure 3.2: Comparison of phase and amplitude fluctuations. (a) Amplitude fluctuations in $v(t)$ shown in blue. (b) Phase fluctuations in $v(t)$ shown in purple.

$$v(t) = V_0 \left[1 + \alpha(t)\right] \cos\left[\Omega_0 t + \phi(t)\right] . \tag{3.2}$$

$\alpha(t)$ is the random fractional amplitude; $|\alpha(t)| \ll 1$. $\phi(t)$ is the random phase in radians; $|\phi(t)| \ll 1$. The phase fluctuations in Equation 3.2 can also be represented as frequency fluctuations:

$$v(t) = V_0 \left[1 + \alpha(t)\right] \cos\left[\Omega_0 t + \int (\Delta\omega)(t) dt\right], \tag{3.3}$$

where $(\Delta\omega)(t) = \dot{\phi}(t)$ is the angular frequency fluctuation. We next determine how to characterize the noise generated by these fluctuations using frequency stability measurements.

3.2 Frequency Stability Measurements

Frequency stability is characterized through two measurements: measurements of the amplitude noise and measurements of the phase noise. Phase noise is characterized through direct measurements of the phase noise, and by measurements of the frequency noise and by Allan deviation. Allan deviation provides a method of characterizing long term drifts in phase.

Amplitude Noise

Amplitude noise arises from fluctuations in the amplitude of the signal $v(t)$. Amplitude noise is defined as the spectral density of the fractional amplitude fluctuations, $S_a(f)$ [36].

$$S_a(f) = \alpha_{RMS}^2(f)\frac{1}{BW}, \tag{3.4}$$

where $\alpha_{RMS}(f)$ is the measured root mean square (rms) value of fractional amplitude fluctuations in a bandwidth of BW containing the frequency f.

We do not consider amplitude noise in the remainder of this thesis. Generally, feedback oscillators and phase locked loops intentionally include amplitude limiters, which suppress amplitude noise [37]. As we will discuss in Chapter 5, we employ an automatic gain control circuit in the implementation of the oscillator. The AGC circuit provides a constant output over a range of input powers, eliminating amplitude noise.

Phase Noise

We next consider phase noise, $S_\phi(f)$. Phase noise is the power spectral density of $\phi(t)$.

$$S_\phi(f) = \lim_{T\to\infty}\frac{1}{T}\int_0^T\int_0^T \boldsymbol{E}\left[\phi^*(t)\phi(t])\right] e^{i2\pi f(t-t')}dtdt'. \tag{3.5}$$

$\boldsymbol{E}[x]$ is expected value of x. The phase noise is also described by $\mathscr{L}(f)$, where

$$\mathscr{L}(f) = \frac{1}{2}S_\phi(f), \tag{3.6}$$

and $\mathscr{L}(f)$ is measured in dBc/Hz. The units for $\mathscr{L}(f)$ arise from the obsolete definition of $\mathscr{L}(f)$ as the ratio of powers:

$$\mathscr{L}(f) = \frac{\text{SSB noise power in a 1 Hz bandwidth offset from the carrier by } f}{\text{Carrier power}}, \tag{3.7}$$

where the carrier is equal to Ω_0. We use $S_\phi(f)$ to describe phase noise throughout; however, we have included the alternate definition of $\mathscr{L}(f)$ because it is the mea-

surement used by manufactures of oscillators and instrumentation. A phase noise measurement performed using the phase noise application on a signal analyzer such as the Keysight PXA N9030A yields a measurement of $\mathscr{L}(f)$, which we must convert to $S_\phi(f)$ in order to compare with the theoretical sources of phase noise; the conversion is given by Equation 3.6.

Frequency Noise

We next characterize the fluctuations in the oscillator as occurring in the instantaneous frequency, $\Delta f(t)$, instead of the phase, $\phi(t)$.

$$S_{\Delta f}(f) = f^2 S_\phi(f). \tag{3.8}$$

However, the fractional frequency noise, $S_y(f)$, is more commonly used, where $y(t) = \frac{\Delta f(t)}{f_0}$ is the fractional frequency.

$$S_y(f) = \frac{f^2}{f_0^2} S_\phi(f). \tag{3.9}$$

We measure $S_\phi(f)$ instead of $S_f(f)$ or $S_y(f)$ due to the ease of the phase noise measurement with instruments such as the Keysight PXA 9030A, which has a dedicated application for phase noise measurement. However, as we will later demonstrate in Chapter 4, it is often easiest to theoretically determine the fractional frequency noise and to then use that expression to find the phase noise.

Allan Variance

Allan variance characterizes phase noise in the time domain. Allan variance measures long term drifts in frequency. However, recent publications in the NEMS community [34] have used Allan variance or Allan deviation to characterize short term drifts in frequency. This measurement usage is contrary to the standard characterization of phase noise, which utilizes $\mathscr{L}(f)$.

Amplitude noise, phase noise, and frequency noise all characterize oscillator noise in the frequency domain. Allan variance characterizes oscillator noise in the time

domain. A frequency counter measures $\bar{f}_k(\tau)$, the average of the instantaneous frequency $f(t)$ over a time interval τ, beginning at time $k\tau$.

$$\bar{f}_k(\tau) = \frac{1}{\tau}\int_{k\tau}^{(k+1)\tau} f(t)dt. \tag{3.10}$$

We rewrite $\bar{f}_k(\tau)$ in terms of the average fractional frequency, $\bar{y}_k(\tau)$, where $\bar{y}_k = (\bar{f}_k - f_0)/f_0$ and $f_0 = \Omega_0/2\pi$.

$$\bar{y}_k(\tau) = \frac{1}{\tau}\int_{k\tau}^{(k+1)\tau} y(t)dt, \tag{3.11}$$

where $y(t) = (f(t) - f_0)/f_0$. We now find the Allan variance, $\sigma_A^2(\tau)$, assuming M contiguous samples of $\bar{y}_k(\tau)$.

$$\sigma_A^2(\tau) = \frac{1}{2(M-1)}\sum_{k=1}^{M}\left(\bar{y}_{k+1} - \bar{y}_k\right)^2. \tag{3.12}$$

The Allan deviation $\sigma_A(\tau)$ is the square root of the Allan variance: $\sigma_A(\tau) = \sqrt{\sigma_A^2(\tau)}$. The Allan variance is related to the fractional frequency noise, $S_y(f)$.

$$\sigma_A^2(\tau) = \int_0^\infty \frac{\sin^4(\pi\tau f)}{(\pi\tau f)^2} S_y(f)df. \tag{3.13}$$

3.3 Comparison of Frequency Stability Measurement Techniques

We next consider the implementation of two of the frequency stability measurement techniques discussed in Section 3.2: Allan deviation and phase noise. Allan deviation measurements [34] correspond to an open loop measurement, as shown in Figure 3.3. The resonator is driven at a constant frequency and a constant amplitude by a frequency source; initially, the driving frequency is equal to the resonant frequency, Ω_0. As time passes, the resonant frequency of the resonator drifts. The in phase and out of phase components of the amplitude of the resonator are tracked with a lock-in amplifier; the phase shift and resulting frequency shift are extracted from the amplitude data. The frequency source is also used to provide a reference frequency input to the lock-in amplifier. The measurement setup required for Allan

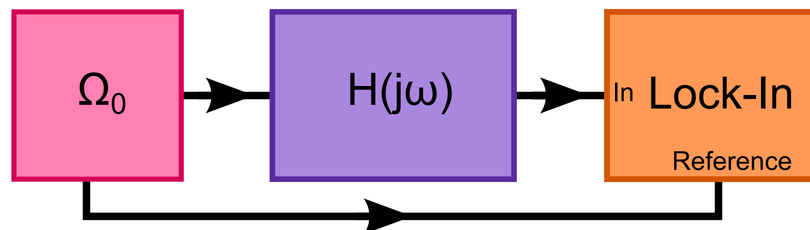

Figure 3.3: Allan deviation measurement setup. The frequency source, shown in pink, drives the resonator, shown in purple, at a constant frequency Ω_0 and a constant drive level; it also provides a reference frequency to the lock-in amplifier. The lock-in, shown in orange, is used to track the amplitude of the resonator.

deviation has fewer components than the measurement setup for phase noise, potentially eliminating sources of noise from the measurement. However, the Allan deviation measurement can only access the linear operating points of the resonator; carefully chosen nonlinear operating points can lead to a reduction in phase noise [31]. Additionally, Allan deviation has historically been used to measure long term drift, on the order of hours to days, by the frequency stability and oscillator community.

Phase noise measurements [31] correspond to a closed loop measurement, as shown in Figure 3.4. Specifically, for a phase feedback oscillator, the phase noise is measured at the out port with an instrument such as the Keysight PXA 9030A Signal Analyzer. The signal from the resonator is split between the out port and the amplifier. The amplifier used is an automatic gain control (AGC) circuit, which has a constant output for a range of inputs. The AGC sets the amplitude of the resonator by setting the amplitude of the signal fed back to the resonator. The output of the AGC is fed to a phase shifter and then back to the resonator. For the closed loop measurement, both linear and non-linear operating points are accessible. In addition, phase noise is the measurement typically used by the frequency stability and oscillator community to characterize the short term stability of oscillators. However, the closed measurement contains more electronics, which can contribute additional sources of noise to the measurement.

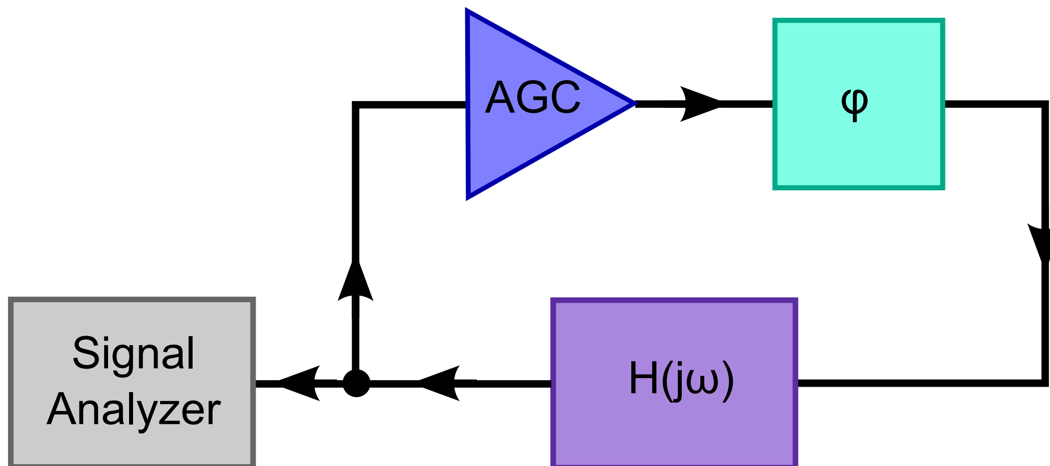

Figure 3.4: Phase noise measurement setup. The resonator, shown in purple, is placed in a loop with an amplifier and a phase shifter. The amplifier, shown in blue, is an automatic gain control circuit (AGC). The phase shifter is shown in green. The output of the resonator is split between the signal analyzer and the amplifier.

3.4 Sources of Frequency Noise

We first consider sources of frequency noise and the frequency dependence of these noise sources. There are three types of frequency noise: white noise, flicker noise, and higher order frequency noise. We discuss how these noise sources translate into phase noise in oscillators in Section 3.5. We conclude with the power law dependence of phase noise.

White Noise

White noise is frequency independent in the frequency domain.

$$S_{\Delta f}(f) = 1. \tag{3.14}$$

Possible sources of white noise include thermal noise and shot noise in the electrical domain, and thermomechanical noise in the mechanical domain. Johnson noise in resistors is an example of thermal noise. The voltage noise power spectral density in a 1 Hz bandwidth is

$$S_{e,n}(f) = 4k_B T R, \tag{3.15}$$

where R is the resistance of the resistor, T is the temperature, and k_B is the Boltzmann constant. Another source of white noise is shot noise. The current noise power spectral density in a 1Hz bandwidth is

$$S_{i,n}(f) = 2qI, \tag{3.16}$$

where q is the charge of the electron and I is the mean current. Amplifiers and photodetectors are both sources of white noise in oscillators. We next consider a source of white force noise in the mechanical domain, arising from thermodynamic fluctuations. Mechanical resonators have dissipation due to damping, which leads to fluctuations through the Fluctuation-Dissipation Theorem[38]. The equivalent force noise power spectral density in a 1Hz bandwidth is

$$S_F(f) = 4k_B T\gamma, \tag{3.17}$$

where γ is the damping of the resonator.

Flicker Noise

Flicker noise is characterized by its f^α with $\alpha \approx 1$ frequency dependence.

$$S_{\Delta f}(f) = \frac{1}{f}. \tag{3.18}$$

Flicker noise is present in the voltage fluctuations observed across resistors [39–41]. Amplifiers are also sources of flicker noise due to the non-linearity of the gain and the modulation of the gain, which lead to parametric up conversion of flicker noise.

3.5 Power Law Dependence of Phase Noise

The power law dependence of phase noise characterizes the type of noise and the physical process underlying the noise. We model $S_\phi(f)$ as a power law function,

$$S_\phi(f) = \sum_{i=-4}^{0} b_i f^i. \tag{3.19}$$

In Table 3.1, we summarize the power law dependence of common phase noise processes in feedback oscillators. Using Equation 3.13, we map the various noises in phase noise to the corresponding power laws in Allan deviation. In Table 3.2, we summarize the corresponding power law dependence for Allan deviation [42]. In Figure 3.5, we plot the frequency dependence of the various phase noise sources. In Figure 3.6, we plot the corresponding dependence for Allan deviation. By considering each power law dependence for phase noise, we will later quantify which sources are viable candidates for APN.

Law	Noise Process
f^0	white phase noise (WPN)
f^{-1}	flicker phase noise (FPN)
f^{-2}	white frequency noise (WFN)
f^{-3}	flicker frequency noise (FFN)
f^{-4}	random walk of frequency noise (RWF)

Table 3.1: Power Law Dependence of Selected Phase Noise Processes

Law	Noise Process
τ^{-1}	white phase noise
$\approx \tau^{-1}$	flicker phase noise
$\tau^{-1/2}$	white frequency noise
τ^0	flicker frequency noise
$\tau^{1/2}$	random walk of frequency

Table 3.2: Power Law Dependence for Allan Deviation

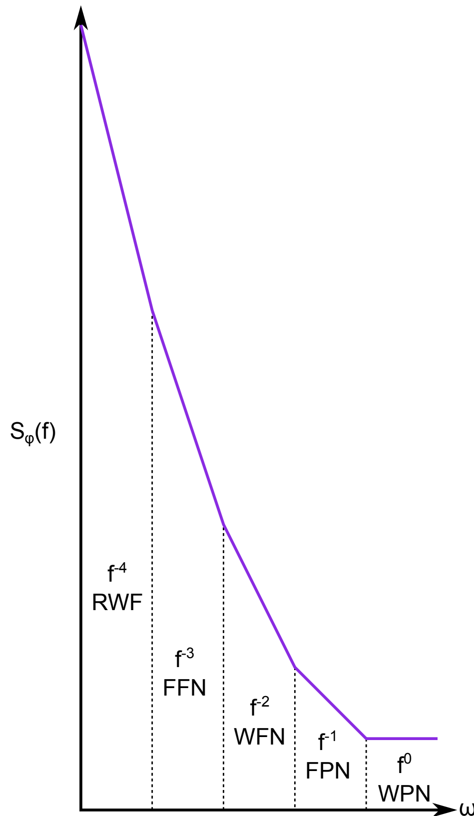

Figure 3.5: Power law dependence of phase noise.

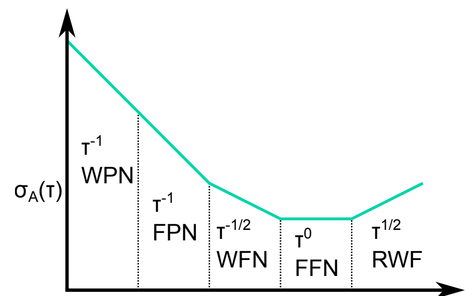

Figure 3.6: Power law dependence of Allan deviation.

White Phase Noise

White phase noise is characterized by its frequency independent spectrum. Typically, white phase noise originates from amplifiers in the oscillator circuit. While the ideal model for an oscillator shown in Figure 3.1 has only one amplifier, the actual implementation used for the measurement in Chapter 5 has several. An additional source of white phase noise is the shot noise from the photodetector used in the measurement. We will further discuss this noise source in Chapter 5.

Flicker Phase Noise

Flicker phase noise is characterized by its f^{-1} frequency dependence. Generally, flicker phase noise arises from amplifiers in the feedback loop. The flicker phase noise of amplifiers is especially important due to the Leeson effect, by which the

oscillator up-converts the flicker phase noise into flicker frequency noise.

Leeson Formula

We use the Leeson formula to relate phase noise in the amplifier, $\psi(t)$, to phase noise in the oscillator, $\phi(t)$. We begin by considering an ideal resonator, one with no phase fluctuations. The resonator has a transfer function $H(j\omega)$ and a quality factor Q, with $Q \geq 10$. The corresponding response time of the resonator is

$$\tau_{Res} = 2\frac{Q}{\Omega_0}. \tag{3.20}$$

The resonator is in a feedback loop with an amplifier, as shown in Figure 3.7. The

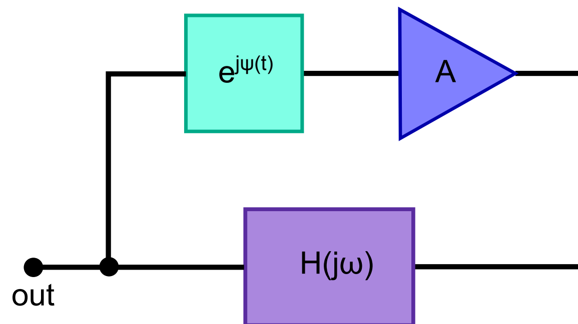

Figure 3.7: Diagram of a feedback oscillator with phase fluctuations.

phase noise in the amplifier is represented by $\psi(t)$, which corresponds to the random phase fluctuations; the power spectral density of these fluctuations is $S_\psi(f)$. The signal produced by this oscillator is $v(t) = V_0 \cos(\Omega_0 t + \psi(t))$. We consider both slow and fast fluctuations in $\phi(t)$, the output phase of the oscillator; the corresponding phase noise is $S_\phi(f)$. Slow fluctuations occur on a frequency scale slower than $1/\tau$. Around the resonant frequency, the resonator has the following relationship between phase and frequency:

$$\Delta f(t) = \frac{f_0}{2Q}\Delta\phi, \tag{3.21}$$

where $\Delta\phi$ is the change in the phase and Δf is the corresponding change in the frequency. For slow fluctuations, the resonator converts the phase shift $\psi(t)$ into a

frequency shift. The corresponding fluctuation in oscillator frequency is given by Equation 3.22.

$$\Delta f\,(t) = \frac{f_0}{2Q}\psi(t). \tag{3.22}$$

The corresponding frequency fluctuation spectral density is given by Equation 3.23.

$$S_{\Delta f}\,(f) = \left(\frac{f_0}{2Q}\right)^2 S_\psi(f), \tag{3.23}$$

where $S_\psi(f)$ is the power spectral density of phase fluctuations. We use Equation 3.8 to find the corresponding phase noise.

$$S_\phi(f) = \frac{1}{f^2}\left(\frac{f_0}{2Q}\right)^2 S_\psi(f). \tag{3.24}$$

We then consider fast fluctuations in $\psi(t)$. The resonator does not respond to the fluctuations; the noise passes through the amplifier to the output. Consequently, the phase noise at the output of the oscillator is equal to the phase noise of the amplifier.

$$S_\phi(f) = S_\psi(f). \tag{3.25}$$

We combine Equations 3.24 and 3.25, yielding Leeson's formula.

$$S_\phi(f) = \left[1 + \frac{1}{f^2}\left(\frac{\nu_0}{2Q}\right)^2\right] S_\psi(f). \tag{3.26}$$

White Frequency Noise

White frequency noise is characterized by its f^{-2} frequency dependence. There are several sources of white frequency noise. The mechanical resonator has several contributions, which we will discuss greater detail in Chapter 4: direct thermomechanical noise, amplitude to phase conversion thermomechanical noise, temperature fluctuation noise, extensional fluctuation noise, adsorption-desorption noise, and higher order mode coupling. The resonator also up converts the white phase noise from the amplifier to white frequency noise through the Leeson effect.

Flicker Frequency Noise

Flicker frequency noise is characterized by its f^{-3} frequency dependence. Flicker noise from the resonator is equivalent to flicker frequency noise in the phase noise domain. As we will demonstrate in Chapter 4, fluctuations in the Young's modulus of the resonator lead to flicker frequency noise in the phase noise domain. Charge fluctuations in the resonator as generate flicker frequency noise in the phase noise domain. $1/f$ noise from the amplifiers is up-converted into f^{-3} phase noise by the resonator.

Random Walk of Frequency

Random walk of frequency noise is characterized by its f^{-4} frequency dependence. The source of random walk frequency noise is the resonator. Possible sources of random walk of frequency noise in NEMS and MEMS resonators are adsorption-desorption noise and diffusion noise, which we will demonstrate in Chapter 4. Random walk of frequency noise is also associated with long term drift; the frequency drift has an exponential dependence [43]:

$$f_0(t) \approx f_0 e^{Dt} \approx f_0(1 + Dt). \tag{3.27}$$

D is on the order of 10^{-11} per day for a 10 MHz quartz crystal oscillator.

3.6 Previous Knowledge of Anomalous Phase Noise

As we noted in the introduction to this chapter, anomalous phase noise has been observed by many researchers in the MEMS and NEMS community [26–33]. In this section, we discuss the APN observed in two specific applications: nonlinear oscillators and NEMS Mass Spectrometry. We then summarize the current knowledge of APN.

APN in Nonlinear Oscillators

The measurements made by Villaneuva et al. [31] during their efforts to reduce phase noise in an oscillator through use of a nonlinear resonator provide what is perhaps the most compelling evidence of APN. They observed an excess phase noise, despite operating the resonator at an optimal point where the susceptibility to many parameter fluctuations became suppressed.

For their phase noise analysis, they used the following framework:

$$S_{\phi}(\delta\nu) = \frac{1}{2\pi}\frac{\nu_c}{Q(\delta\nu)^2}\sum_n I_n D_n, \tag{3.28}$$

where ν_c is the carrier frequency, Q is the quality factor of the resonator, and $\delta\nu$ is the offset from the carrier. I_n is the noise intensity due to a specific source of noise and D_n is the corresponding susceptibility or “diffusion parameter”, which determines how the noise source is transformed into the phase noise. They divided the noise sources into two categories: thermomechanical noise, and parameter fluctuation noise. As we will discuss in Chapter 4, thermomechanical noise, I_{Th}, is due to Brownian motion of the resonator. Thermomechanical noise leads to both amplitude and phase fluctuations and has two contributions to $S_{\phi}(\delta\nu)$: a direct contribution due to thermomechanical phase noise, which corresponds to D_{direct}, and a conversion of the thermomechanical amplitude noise into phase noise, which corresponds to D_a. They considered the noise due to fluctuations in the following parameters: Δ, the phase delay, s, the saturation level, α, a parameter that characterizes the nonlinearity of the resonator, γ, a parameter that characterizes the intrinsic damping of the resonator, and Ω_0, the resonant frequency.

For their measurements, Villaneuva et al. employed a doubly clamped aluminum nitride beam with a resonant frequency of 12.63 MHz and a quality factor of 1600. They operated their nonlinear resonator at a variety of Δ and s parameters and measured the phase noise at an offset of 1kHz. They then measured I_{Th}, I_s, and I_{Δ},

and estimated I_γ and I_α. For most of the parameter space, the measured data agreed with the noise levels predicted. However, around the amplitude detachment point (ADP), where amplitude to phase noise conversion was suppressed, they observed an excess source of phase noise. At the ADP, contributions from D_a and D_Δ are minimized. The contribution from D_{direct} is minimized by operating the oscillator at a high amplitude. For their highest saturation level, they observed an excess phase noise of 10dBc/Hz. Their noise analysis demonstrates that this excess phase noise is not a product of the electronics used in the feedback loop of the oscillator; the excess noise observed corresponds to a mechanical domain noise source.

APN in NEMS Mass Spectrometry

The frequency stability caused by APN also limits frequency shift based mass sensing applications. We consider the simple case of a doubly-clamped beam resonator, vibrating in its fundamental mode at a resonant frequency Ω_0. When a point mass δM lands on the center of the beam, the resonant frequency of the device shifts downwards by an amount $\delta\Omega$. The change in the frequency is directly proportional to the mass deposited on the device.

$$\delta M \approx -2\frac{M_{eff}}{\Omega_0}\delta\Omega. \tag{3.29}$$

M_{eff} is the effective mass, which depends upon the mode shape. The minimum detectable mass, δM_{MIN}, is directly proportional to the minimum detectable frequency shift, $\delta\Omega_{MIN}$.

$$\delta M_{MIN} \approx -2\frac{M_{eff}}{\Omega_0}\delta\Omega_{MIN}. \tag{3.30}$$

The minimum detectable frequency shift, $\delta\Omega_{MIN}$, is set by the thermomechanical noise limit [17].

$$\delta\Omega_{MIN} \approx \frac{1}{Q}\left[\frac{k_B T}{M_{eff}\Omega_0^2\langle x_c^2\rangle}\right]^{1/2}, \tag{3.31}$$

where Q is the quality factor of the device, k_B is the Boltzmann constant, T is the temperature, and $\langle x_c \rangle$ is the rms amplitude at which the resonator is driven. Typically, $\langle x_c \rangle$ is the 1dB compression point [44]; at higher amplitudes, non-linear effects usually lead to larger noise. When we compare the value for $\delta\Omega_{MIN}$ from the thermomechanical noise limit to experimentally measured values of $\delta\Omega_{MIN}$, we obtain a value that is generally 10 to 1000 times smaller than the experimentally measured values [4, 28, 45]. Understanding the source of APN is crucial for MEMS and NEMS frequency shift sensors and oscillators.

Characteristics of Anomalous Phase Noise

Previous measurements of frequency stability across a wide range of devices [26–34, 46] have demonstrated that the frequency stability is limited by a source other than thermomechanical noise; we refer this unknown source of noise to as anomalous phase noise (APN). It is unclear for some of these works whether the excess noise is due to a fundamental noise source or if the noise is due to unoptimized measurement setups. Excess noise is observed in devices fabricated from a wide range of materials, including crystalline materials such as single crystal silicon (SCS) [26, 27, 34] and silicon carbide (SiC) [28], amorphous materials such as highly stressed SiN [29], multi-stack layers of aluminum nitride-molybdenum [30, 31], and single layer materials such as graphene [32] and carbon nanotubes [47]. Excess noise is observed in cantilevers [26], doubly clamped beams [26, 28, 29, 33], and membranes [32]. Excess noise also is observed with a wide variety of detection and actuation methods. Hentz [27] compared the Allan deviation measured with capacitive actuation and either piezoresistive detection or optical interferometric detection; the measured Allan deviation was independent of detection method. The Allan deviation was also similar when either a piezoelectric shaker or capacitive drive was used to actuate the device. No clear dependence on device material, shape, actuation method, or

detection method is observed for APN.

Temperature and frequency power law dependencies have been observed for APN. The temperature dependence appears to be T^{α} with $\alpha \approx 1$. Sage [26] observed a factor of 2.5 decrease in the measured Allan deviation upon cooling the devices from 300K to 100K, which roughly corresponds to a T^{α} dependence with $\alpha \approx 1$. Fong et al. [33] observed a T^{α} dependence with $\alpha = 0.94 \pm 0.10$ from 5K to 296 K, as shown in Figure 3.8. The quantity shown in the figure, $S_0(T)$ is found by multiplying the fractional frequency noise, $S_y(f)$, by the offset from the carrier, f, to find a parameter independent of frequency, since they also observed the frequency dependence of the phase noise to be f^{β} with $\beta \approx -3$.

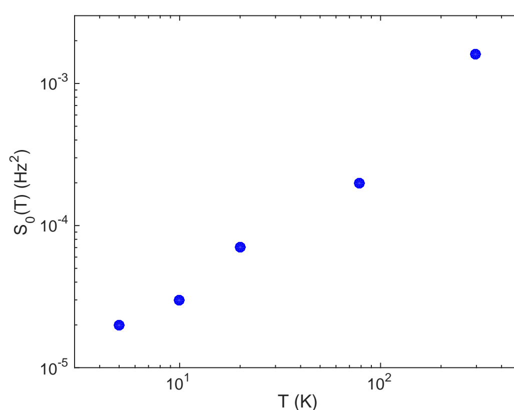

Figure 3.8: Temperature versus $S_0(T) = S_y(f)f$.

Hentz [27] and Sage [26] both observe an Allan deviation roughly independent of integration time, which corresponds to phase noise with a frequency dependence of f^{β} with $\beta \approx -3$. Gavartin et al. [29] also observe an Allan deviation roughly independent of integration time. Villanueva et al. [30] also measure phase noise with a roughly $1/f^3$ frequency dependence. Zhang et al. [47] observe a frequency noise with a $f^{-1/2}$ dependence, which corresponds to a $1/f^{5/2}$ phase noise. Their phase noise dependence is different than that of other works. However, the rest

of the references dealt with bulk materials at temperature greater than 4K; this measurement employed a carbon nanotube with a measurement temperature of 1K.

3.7 Summary

In summary, APN has a frequency dependence of f^{β} with $\beta \approx -3$ and a temperature dependence of T^{α} with $\alpha \approx 1$. APN does not appear to have a material or mode shape dependency. Understanding the source of APN and suppressing it is crucial for attaining the ultimate limits of performance for applications of NEMS and MEMS.

Chapter 4

SOURCES OF PHASE NOISE IN MEMS AND NEMS

As shown in Chapter 3, anomalous phase noise (APN) limits the performance of MEMS and NEMS. In this chapter, we provide a theoretical framework for sources of phase noise in oscillators using high-Q weakly nonlinear resonators, as formulated by Kenig et al. in [31, 48, 49]. Specifically, we divide the sources of phase noise into two categories: thermomechanical noise and parameter noise. Thermomechanical noise is a result of the finite Q of the mechanical resonator; the resonator dissipates energy, which leads to noise through the Fluctuation-Dissipation theorem. Thermomechanical noise has two contributions to phase noise: a direct contribution and a contribution from amplitude to phase ($A - \phi$) conversion. Parameter noise encompasses phase noise caused by fluctuations in the parameters that control the operating point of the oscillator, such as the quality factor of the resonator, the nonlinear coefficient of the spring constant, the phase of the feedback, the saturation level of the amplifier used to sustain the oscillator, and fluctuations in the resonant frequency Ω_0. We consider the following sources of fluctuations in the resonant frequency: temperature fluctuations, extensional fluctuations, charge fluctuations, mass fluctuations of the device due to adsorption-desorption or diffusion, fluctuations from higher order mode coupling, and fluctuations in Young's modulus due to defect reorientation. We provide expressions for both the phase noise and Allan deviation for each source. We calculate the phase noise from each noise source for a prototype device, similar to the device used for measurements in Chapter 6 and plot the phase noise. We then assess each noise source as a potential candidate for APN. We end the chapter with a summary table containing formulae for the phase noise and Allan deviation due to each source.

4.1 Noise Analysis of a Phase Feedback Oscillator

Following Kenig et al. [31, 48, 49], we consider the phase noise in an oscillator containing a high-Q weakly nonlinear resonator. We begin by finding the dynamics of the resonator. We then add noise to the system and determine how the noise generates phase noise in the oscillator. We consider two types of noise: noise from thermomechanical motion and noise from fluctuations in the parameters that control the operating point of the oscillator. Figure 4.1 contains a diagram of the oscillator components and the parameters associated with each component.

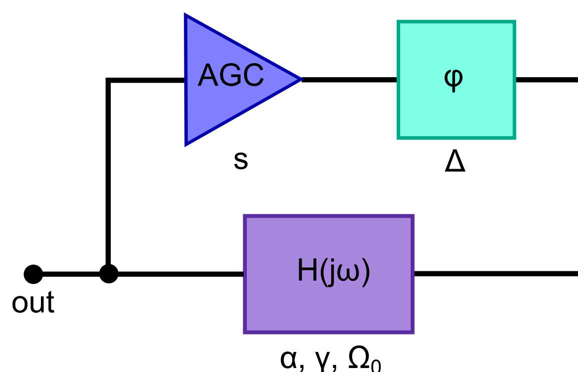

Figure 4.1: Diagram of a phase feedback oscillator with operating parameters. s is the saturation level of the automatic gain control (AGC). Δ is the phase shift induced by the phase shifter. α, γ, and Ω_0 are all parameters associated with the weakly nonlinear resonator with transfer function $H(j\omega)$. α characterizes the nonlinearity of the resonator. γ characterizes the intrinsic damping of the resonator, which is proportional to the quality factor of the resonator. Ω_0 is the frequency of the resonator.

We begin the analysis by finding the time evolution of $A(T) = a(T)e^{i\phi(T)}$, the complex amplitude of the resonator, where $T = \epsilon\Omega_0 t$ is a dimensionless time scale. ϵ is an small expansion factor that will be chosen later in the analysis. Ω_0 is the resonant frequency of the oscillator. $a(T)$ is the magnitude of the amplitude and $\phi(T)$ is the phase of the amplitude. We are interested in the case of a phase feedback oscillator [50, 51], which employs an element such as automatic gain control (AGC) to maintain a constant drive level to the resonator, independent of the output of the resonator. The dimensionless equation of motion for $A(T)$ for a phase feedback

oscillator is given in Equation 4.1:

$$\frac{dA}{dT} = -\frac{\gamma}{2}A + i\frac{3}{8}\alpha|A|^2 A - i\frac{s}{2}e^{i\phi}e^{i\Delta}, \tag{4.1}$$

where s is the saturation level. The saturation level of the amplifier controls the magnitude of the power fed back to the resonator. γ characterizes the linear damping of the resonator.

$$\gamma = \frac{1}{Q\epsilon}, \tag{4.2}$$

where ϵ is a scale factor. α characterizes the nonlinearity of the resonator through the nonlinear spring coefficient $\tilde{\alpha}$, where the spring constant is defined as $k = M_{eff}\Omega_0^2 + \tilde{\alpha}x^2$, and M_{eff} is the effective mass of the resonator. M_{eff} is a mode dependent parameter.

$$\alpha = \frac{\tilde{\alpha}x_0^2}{M_{eff}\Omega_0^2\epsilon}, \tag{4.3}$$

where x_0^2 is a scale factor. We choose the following scale factors:

$$x_0^2 = \frac{M_{eff}\Omega_0^2}{\tilde{\alpha}Q}, \tag{4.4a}$$

$$\epsilon = Q^{-1}. \tag{4.4b}$$

This scaling leads to a consistent perturbation theory because γ and α are $\mathcal{O}(1)$. We separate Equation 4.1 into equations for the time evolution of the amplitude and the phase.

$$\frac{da}{dT} = -\frac{\gamma}{2}a + \frac{s}{2}\sin\Delta \equiv f_a, \tag{4.5}$$

$$\frac{d\phi}{dT} = \frac{3}{8}\alpha a^2 - \frac{s}{2}\frac{\cos\Delta}{a} \equiv f_\phi. \tag{4.6}$$

We now consider steady state oscillations. For that case,

$$\frac{da}{dT} = 0, \quad \text{and} \tag{4.7a}$$

$$\frac{d\phi}{dT} = \Omega = Q\frac{\omega}{\Omega_0}, \tag{4.7b}$$

where ω is the frequency offset from the carrier frequency Ω_0. Ω is the scaled, dimensionless frequency offset from the carrier frequency. We solve Equations 4.5 and 4.6 for the oscillation amplitude and frequency offset.

$$a = \frac{s}{\gamma}\sin(\Delta), \tag{4.8}$$

$$\Omega = \frac{3}{8}\alpha a^2 - \frac{s}{2}\frac{\cos(\Delta)}{a}. \tag{4.9}$$

The oscillation amplitude, a, depends upon both the saturation level, s, and the phase shift, Δ. We next determine how noise generates phase noise in the feedback-sustained oscillator. We model the noise by adding the stochastic term $v_{a,n}\Xi_n(T)$ to Equation 4.5 and the stochastic term $v_{\phi,n}\Xi_n(T)$ to Equation 4.6. $v_{a,n}$ and $v_{\phi,n}$ provide the strength of the noise vector in the amplitude and phase quadrature, respectively, for a specific noise source n. $\Xi_n(T)$ characterizes the noise from noise source n. We now find the variance of the phase deviation. We neglect da/dT when calculating the amplitude fluctuations for small frequency offsets compared to the resonator linewidth. In addition, f_a and f_ϕ are independent of ϕ, as shown by Equations 4.5-4.6. The long time phase diffusion is

$$[\delta\phi(T+\tau) - \delta\phi(T)]^2 = \left(\sum_n D_n I_n\right)\tau. \tag{4.10}$$

The diffusion susceptibility D_n is

$$D_n = \left(v_{\phi,n} - \frac{\partial f_\phi/\partial a}{\partial f_a/\partial a} v_{a,n}\right)^2. \tag{4.11}$$

The noise intensity I_n is

$$\langle \Xi_n(T)\Xi_n(T')\rangle = I_n\delta\left(T - T'\right). \tag{4.12}$$

The first component of D_n corresponds to the direct contribution of a noise source to the phase noise. The second contribution corresponds to the conversion of amplitude noise into phase noise. The phase noise is

$$S_\phi(\omega) = \frac{1}{2\pi Q}\frac{\sum_n I_n D_n \Omega_0}{\left(\frac{\sum_n I_n D_n \Omega_0}{2Q}\right)^2 + \omega^2}. \tag{4.13}$$

For $|\omega| \gg |\sum_n I_n D_n| \frac{\Omega_0}{2Q}$, Equation 4.13 simplifies to

$$S_\phi(\omega) = \frac{1}{2\pi Q} \frac{\Omega_0}{\omega^2} \sum_n I_n D_n \tag{4.14}$$

We now have a method for finding the phase noise due to thermomechanical noise and parameter fluctuations.

We next find the phase noise due to the various noise sources in the oscillator. The first source of noise, thermomechanical noise, arises from a stochastic driving term that is added to the governing equation for the oscillator. Additional stochastic driving terms depend upon the experimental setup used to measure the phase noise; shot noise from a photodetector used for optical detection is another stochastic driving term. For clarity, we will only consider the stochastic driving term that arises from thermomechanical motion. The second source of noise, parameter noise, arises from fluctuations in the parameters that control the operating point of the oscillator: Δ, s, α, and γ.

From the fluctuation-dissipation theorem, mechanical resonators with finite Q dissipate energy and, consequently, experience force fluctuations [6, 17, 52]. Thermomechanical noise affects both the amplitude and the phase of the oscillator. The contribution to phase noise from thermomechanical noise is always present; we refer to this contribution as the direct thermomechanical noise. The corresponding noise vector is $(v_{a,direct}, v_{\phi,direct}) = (0, 1/a)$; the noise is only in the phase component. The corresponding diffusion coefficient, D_{direct}, is

$$D_{direct} = \frac{1}{a^2}. \tag{4.15}$$

The thermomechanical noise contribution to amplitude noise contributes to the phase noise through amplitude to phase conversion. The corresponding noise vector is $(v_{a,a}, v_{\phi,a}) = (1, 0)$; the noise is only in the amplitude component. The

corresponding diffusion coefficient, D_a, is

$$D_a = \left(\frac{\partial f_\phi}{\partial a} \Big/ \frac{\partial f_a}{\partial a}\right) \equiv \left(\frac{3}{2}a + \frac{1}{a^2}\cos(\Delta)\right)^2. \tag{4.16}$$

We set $\gamma = \alpha = 1$, the value previously chosen for both variables for the given scalings. We next find I_{Th}.

$$I_{Th} = \frac{k_B T Q \tilde{\alpha_0}}{M_{eff}\Omega_0^2} \tag{4.17}$$

The total contribution from thermomechanical noise is given by Equation 4.18, where $D_{Th} = D_{direct} + D_a$.

$$S_\phi(\omega) = \frac{1}{2\pi Q} \frac{I_{Th} D_{Th} \Omega_0}{\left(\frac{I_{Th} D_{Th} \Omega_0}{2Q}\right)^2 + \omega^2}. \tag{4.18}$$

We have not assumed $|\omega| \gg |\sum_n I_n D_n| \frac{\Omega_0}{2Q}$; we are interested in $S_\phi(\omega)$ close to the carrier in Chapter 6. We defer calculation of $S_\phi(\omega)$ for a test device until Section 4.3.

The second category of noise corresponds to fluctuations in the parameters that determine the operation point of the oscillator: Δ, s, α, γ, and Ω_0. We now find D_n for each of these parameters; we will not consider values of I_n for Δ, s, α, and γ until Chapter 6, where we experimentally determine their values. Noise fluctuations in a parameter p_i have the following noise vector: $(v_a, v_\phi) = (\partial f_a/\partial p_i, \partial f_\phi/\partial p_i)$. We employ the stationary amplitude approximation $f_a = 0$ when calculating the noise vectors, which leads to the simplification of Equation 4.11.

$$D_n = \left(\frac{df_\phi}{dp_i}\right)^2. \tag{4.19}$$

We begin by rewriting Equation 4.6.

$$f_\phi = \frac{3}{8}\frac{\alpha s^2}{\gamma^2}\sin^2(\Delta) - \frac{\gamma}{2}\cot(\Delta). \tag{4.20}$$

We first consider fluctuations in Δ.

$$\frac{df_\phi}{d\Delta} = \frac{3}{4}\frac{\alpha s^2}{\gamma^2}\sin(\Delta)\cos(\Delta) + \frac{\gamma}{2}\sec^2(\Delta). \tag{4.21}$$

We rewrite Equation 4.21 in terms of a and use Equation 4.19 to find D_Δ.

$$D_\Delta = \left(\frac{3}{4}a^2\cot(\Delta) + \frac{1}{2}\csc^2(\Delta)\right)^2. \tag{4.22}$$

We next consider fluctuations in s.

$$\frac{df_\phi}{ds} = \frac{3}{4}\frac{\alpha s}{\gamma^2}\sin^2(\Delta). \tag{4.23}$$

We rewrite Equation 4.23 in terms of a and use Equation 4.19 to find D_s.

$$D_s = \left(\frac{3}{4}a\sin(\Delta)\right)^2. \tag{4.24}$$

We next consider fluctuations in α.

$$\frac{df_\phi}{d\alpha} = \frac{3}{8}a^2, \tag{4.25}$$

$$D_\alpha = \left(\frac{3}{8}a^2\right)^2. \tag{4.26}$$

We consider fluctuations in γ.

$$\frac{df_\phi}{d\alpha} = -\frac{3}{4}\frac{\alpha s^2}{\gamma^3}\sin^2(\Delta) - \frac{1}{2}\cot(\Delta). \tag{4.27}$$

We rewrite Equation 4.27 in terms of a and use Equation 4.19 to find D_γ.

$$D_\gamma = \left(\frac{3}{4}a^2 + \frac{1}{2}\cot(\Delta)\right)^2. \tag{4.28}$$

We finally consider fluctuations in the resonant frequency.

$$D_{\Omega_0} = \frac{1}{4}. \tag{4.29}$$

We summarize diffusion coefficients in Table 4.1.

In the remainder of this chapter, we calculate the phase noise for a prototype device described in Section 4.2. We choose an operating point at 300 K of ($a = 0.85, \Delta = \pi/2$), which corresponds to an average of the operating parameters for the two devices measured in Chapter 6 at 297 K. In the interest of clarity, we assume the

usage of an ideal AGC and an ideal phase shifter; consequently, $I_\Delta = I_s = 0$. In Chapter 6, we measure I_Δ and estimate I_s; in that case, both are significantly smaller than I_{Th}. For the chosen operating point, $D_a > D_{direct} > D_s > D_\Delta$. Thus, the contributions from direct and $A - \phi$ thermomechanical noise dominate. We also assume that neither the quality factor of the resonator nor the nonlinear spring constant fluctuates; $I_\alpha = I_\gamma = 0$. Thus, we only consider phase noise from the following sources: direct thermomechanical noise, amplitude to phase conversion thermomechanical noise, and fluctuations in the resonant frequency, Ω_0. In Chapter 6, we measure the fluctuations in s and Δ and include them in the analysis of the measured phase noise.

Table 4.1: Diffusion Coefficients

Type of noise	Diffusion coefficient	Noise intensity
Thermomechanical direct	$D_{direct} = \frac{1}{a^2}$	I_{Th}
Thermomechanical-A-ϕ conversion	$D_a = \left(\frac{3}{2}a + \frac{1}{a^2}\cos(\Delta)\right)^2$	I_{Th}
Parameter Noise-Δ	$D_\Delta = \left(\frac{3}{4}a^2\cot(\Delta) + \frac{1}{2}\csc^2(\Delta)\right)^2$	I_Δ
Parameter Noise-s	$D_s = \left(\frac{3}{4}a\sin(\Delta)\right)^2$	I_s
Parameter Noise-α	$D_\alpha = \left(\frac{3}{8}a^2\right)^2$	I_α
Parameter Noise-γ	$D_\gamma = \left(\frac{3}{4}a^2 + \frac{1}{2}\cot(\Delta)\right)^2$	I_γ
Parameter Noise-Ω_0	$D_{\Omega_0} = \frac{1}{4}$	I_{Ω_0}

4.2 Prototype Device

In order to determine whether each source of phase noise is a potential candidate for APN, we compute the phase noise due to each source for a prototype device, similar to the device used for measurements in Chapter 6. The prototype device is a silicon doubly clamped beam. We provide the properties of the prototype device in Table 4.2 and the material properties used for all calculations in Table 4.3; all properties are provided at 300 K. Figure 4.2 contains an SEM image of a Si doubly clamped

This is a SEM image
of a silcon doubly
clamped beam.

Figure 4.2: Colorized image of a Si doubly clamped beam. **The beam dimensions are [insert numbers after imaging].**

beam with dimensions similar to that of the prototype.

Table 4.2: Prototype Device Properties

Property	Symbol	Value
Length	L	50 μm
Width	w	5 μm
Thickness	t	285 nm
Effective Mass	M_{eff}	64.7 pg
Resonant Frequency	$\Omega_0/(2\pi)$	1 MHz
Quality Factor	Q	23000

Table 4.3: Material Properties

Property	Symbol	Value
Young's Modulus [53]	$E_{\langle 110 \rangle}$	169 MPa
Poisson's ratio [53]	ν_{xz}	0.364
Density of Si [54]	ρ	2329 kg/m^3
Linear Coefficient of Thermal Expansion [54]	α	2.6×10^{-6} 1/K
Heat Capacity at Constant Pressure [54]	C_P	702 J/(kg·K)
Temperature	T_0	300 K
Thermal Conductivity [54]	κ	124 W/(m·K)
Fractional Temperature Dependence of Speed of Sound [55]	$\frac{1}{c_s}\frac{\partial c_s}{\partial T}$	-5$\times10^{-5}$/K

We use the following nomenclature throughout the discussion of the various noise sources. When referring to the resonant frequency of the device, we use Ω_0. When referring to the offset from carrier in fractional frequency noise, phase noise, or frequency fluctuations, we use ω. We label all noise sources with subscripts for clarity.

4.3 Thermomechanical Noise

From the fluctuation-dissipation theorem, mechanical resonators with finite Q dissipate energy and consequently are subject to force fluctuations [6, 17, 52]. As discussed in Section 4.1, the thermomechanical noise engenders two contributions to phase noise: a direct contribution and a contribution from amplitude to phase $(A-\phi)$ conversion. We previously found the phase noise due to these two contributions. Before finding the phase noise, we first find $\lambda_{1,1} = \tilde{\alpha}/(M_{eff}\Omega_0^2)$. Following Matheny et al. [56], the square of the total frequency shift due to nonlinear mode coupling is $\Omega^2_{p,mod}$.

$$\Omega^2_{p,mod} = \Omega_p^2 \left(1 + 2\lambda_{p,p}A_p^2 + 2\lambda_{p,q}A_q^2\right), \tag{4.30}$$

where $\lambda_{p,p}$ corresponds to the nonlinear spring coefficient for mode p, and $\lambda_{p,q}$ corresponds to nonlinear mode coupling from mode q to mode p. We treat the contribution from $\lambda_{p,q}$ in Section 4.4. Both $\lambda_{p,p}$ and $\lambda_{p,q}$ are defined by Equation 4.31.

$$\lambda_{p,q} = \left(2-\delta_{pq}\right)\frac{\chi_p}{8}\left(\frac{X_{pp}X_{qq}}{2} + X_{pq}^2\right). \tag{4.31}$$

δ_{pq} is the Kronecker delta function. χ_p and η_p are defined in Equation 4.32.

$$\chi_p = \frac{\eta_p}{1+\eta_p X_{pp}\frac{\tau L^2}{E}}, \tag{4.32a}$$

$$\eta_p = \frac{tw}{I\int_0^1 \Phi_p(\xi)\Phi_p^{(IV)}(\xi)\mathrm{d}\xi}. \tag{4.32b}$$

τ is the tension and I is the areal moment of inertia. $\Phi_p(\xi)$ is the mode amplitude; the length scale has been normalized such that $\xi = 1$ at L. $\Phi_p(\xi)$ has the following normalization: $\int_0^1 \Phi_p(\xi)\Phi_q(\xi)\mathrm{d}\xi \equiv \delta_{pq}$. $X_{pq} = \int_0^1 \Phi_p'(\xi)\Phi_q'(\xi)\mathrm{d}\xi$. $\Phi^{(IV)}(\xi)$ is the 4th spatial derivative. Thus, given a device, we can calculate the nonlinear coefficients.

Before finding the fractional frequency noise, we find $\Phi_1(\xi)$. $\Phi_n(\xi)$, the nth mode of a doubly clamped beam, has the mode shape given in Equation 4.34 [57].

$$\Phi_n(\xi) = C_n\Bigg[\cosh(k_n\xi) - \cos(k_n\xi) + \frac{\cosh(k_n\xi) - \cos(k_n\xi)}{\sinh(k_n) - \sin(k_n)}\left(\sin(k_n\xi) - \sinh(k_n\xi)\right)\Bigg], \tag{4.33}$$

(4.34)

where C_n is defined such that $\int_0^1 \Phi_p(\xi)\Phi_q(\xi)\mathrm{d}\xi = 1$. k_n is defined by the following boundary condition: $\cos(k_n)\cosh(k_n) = 1$. We list the value for C_1 and k_1 for the first mode of a doubly clamped beam in Table 4.4.

Mode Number	C_n	k_n
1	1	4.730

Table 4.4: Mode Shape Parameters

Using these parameters and the properties of the prototype device, we find $\lambda_{1,1} = 8.38 \times 10^{12}$ m^{-2}. However, for the calculations we use the measured value from Chapter 6 of $(-3.6 \pm 0.2) \times 10^{12}$ m^{-2}.

In order to calculate the phase noise, we chose an operating point for the oscillator. We choose $a = 0.85$, which is the approximate operating point for the measurements performed on two oscillators at 297 K in Chapter 6. We next calculate $I_{Th}D_{Th}\Omega_0/(2Q) = 9.5 \times 10^{-8}$. We find that $I_{Th}D_{Th}\Omega_0/(2Q) \ll \omega$ in the region of interest; we use Equation 4.14 to calculate the phase noise.

$$S_\phi(\omega) = S_{\phi,direct}(\omega) + S_{\phi,A-\phi}(\omega) \tag{4.35a}$$

$$S_{\phi,direct}(\omega) = \frac{1}{2\pi}\frac{\Omega_0}{\omega^2}\frac{1}{a^2}\frac{k_B T\tilde{\alpha}_0}{\left(M_{eff}\Omega_0^2\right)^2} \tag{4.35b}$$

$$S_{\phi,A-\phi}(\omega) = \frac{1}{2\pi}\frac{\Omega_0}{\omega^2}\left(\frac{3}{2}a + \frac{1}{a^2}\cos(\Delta)\right)^2\frac{k_B T\tilde{\alpha}_0}{\left(M_{eff}\Omega_0^2\right)^2} \tag{4.35c}$$

We next plot the phase noise due to each contribution.

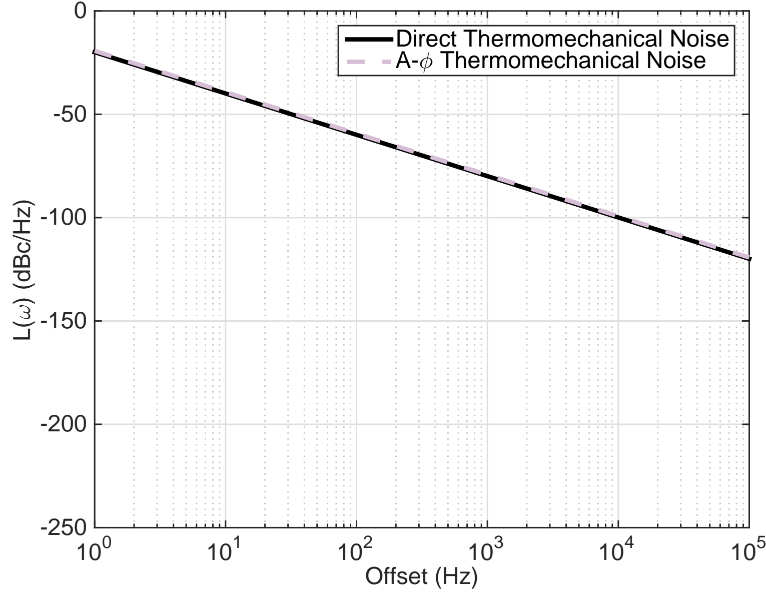

Figure 4.3: Comparison of phase noise from direct thermomechanical noise and amplitude to phase conversion thermomechanical noise for $a = \sqrt{2/3}$ and $\Delta = \pi/2$.

We also consider the phase noise for different values of a: 0.5, $\sqrt{2/3}$, 1, and 2, as shown in Figure 4.4. $a = \sqrt{2/3}$ corresponds to the amplitude for which the contributions from direct thermomechanical noise and A-ϕ thermomechanical noise are equal, for $\Delta = \pi/2$. For $a < \sqrt{2/3}$, direct thermomechanical noise dominates. For $a = \sqrt{2/3}$, the two contributions are equal. For $a > \sqrt{2/3}$, A-ϕ thermomechanical noise dominates.

We next find the Allan deviation due to each contribution. For a phase noise of the form $S_\phi(\omega) = C\left(\frac{\Omega_0}{\omega}\right)^2$ [52], the corresponding Allan deviation is

$$\sigma_A(\tau_A) = \sqrt{\frac{\pi C}{\tau_A}}. \tag{4.36}$$

The Allan deviation due to direct thermomechanical noise is

$$\sigma_{A,direct}(\tau_A) = \sqrt{\frac{1}{2\tau_A}\frac{1}{a^2}\frac{k_B T\tilde{\alpha}_0}{\left(M_{eff}\Omega_0^2\right)^2}}. \tag{4.37}$$

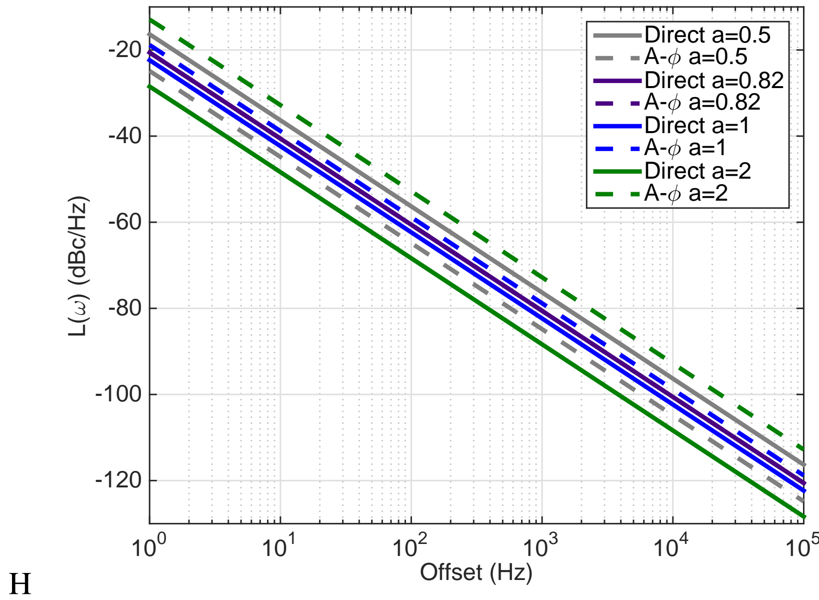

H

Figure 4.4: Comparison of phase noise from direct thermomechanical noise and amplitude to phase conversion thermomechanical noise for $a = 0.5,\ \sqrt{2/3},\ 1,\ 2$ and $\Delta = \pi/2$.

The Allan deviation due to A$-\phi$ conversion thermomechanical noise is

$$\sigma_{A,A-\phi}(\tau_A) = \sqrt{\frac{1}{2\tau_A}\left(\frac{3}{2}a + \frac{1}{a^2}\cos(\Delta)\right)^2 \frac{k_B T \tilde{\alpha}_0}{\left(M_{eff}\Omega_0^2\right)^2}}. \tag{4.38}$$

Neither component of thermomechanical noise, direct and A-ϕ conversion, is a candidate for anomalous phase noise. The magnitude of the phase noise is too small for APN. In addition, the frequency dependence of both is $1/f^2$, while the frequency dependence of APN is $1/f^3$.

4.4 Parameter Fluctuations: Ω_0

We now consider contributions to phase noise due to fluctuations in Ω_0. We consider contributions from several sources: temperature fluctuations, extensional fluctuations, charge fluctuations, gas interactions, higher order mode coupling, and defect motion. Temperature fluctuation noise arises from the finite heat capacity and finite thermal conductivity of the device. Extensional fluctuations noise arises from

fluctuations in the length of the device. Charge fluctuations lead to a fluctuating electrostatic spring softening. Gas adsorbing and desorbing from the surface of the device and gas diffusing along the surface of the device lead to fluctuations in the mass of the device. Thermomechanical noise in the amplitude quadrature from higher order modes leads to frequency fluctuations through nonlinear mode coupling. Stochastic defect reorientation leads to fluctuations in the Young's modulus.

Temperature Fluctuation Noise

The device has a finite thermal conductance and a finite heat capacity that together lead to temperature fluctuations in the device when coupled to an external reservoir. The resonant frequency has multiple parameters with temperature dependence: Young's modulus, density, length, thickness, and stress. Fluctuations in temperature thus lead to fluctuations in these parameters and consequently frequency fluctuations.

We begin by finding the spectral density of the temperature fluctuations. The heat capacity and thermal conductance of the device are distributed in space. Following Cleland and Roukes [52], we divide the device into chunks of length ℓ, where ℓ is the mean free phonon path of Si, and cross-section $A = w \times t$. At room temperature, $\ell \approx 50$ nm. Each chunk has a heat capacity, $c_i = C_V A\ell$, and a thermal conductance, $g_i = \kappa A/\ell$. The thermal model for the beam is shown in Figure 4.5.

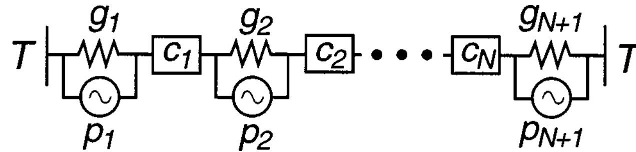

Figure 4.5: Thermal model for a doubly clamped beam. Figure taken from [52].

The temperature fluctuation of the nth chunk is $S_{T,n}(\omega)$:

$$S_{T,n}(\omega) = \frac{2}{\pi} \frac{k_B T^2/g_n}{1 + \omega^2 \tau_{T,n}^2}, \tag{4.39}$$

where $\tau_{T,n} = c_n/g_n$. As we will show later in this section, $\tau_{T,n} = 43$ ps at 300 K with $\ell = 50$ nm for the prototype device. Thus, $\omega\tau_{T,n} \ll 1$ for $\omega < 10^9$, which is much higher than the offset frequencies considered. For $\omega\tau_{T,n} \ll 1$, which applies for the prototype in the offset frequencies considered, the temperature fluctuations from the thermal conductance in the beam cancel each other out. However, the thermal conductances at the ends of the beam do cause temperature fluctuations. The sum of the two contributions is

$$S_T(\omega) = \frac{4}{\pi}\frac{k_B T^2/g}{1+\omega^2\tau_T^2} \quad \text{for} \quad \omega\tau_T \ll 1, \tag{4.40}$$

where $\tau_T = c/g$.

We now find $S_{TF}(\omega)$ by determining the temperature dependence of the resonant frequency, $\Omega(T)$. The relationship between the spectral density of temperature fluctuations and fractional frequency noise is

$$S_{y,TF}(\omega) = \left(\frac{1}{\Omega}\frac{\partial\Omega}{\partial T}\right)^2 S_T(\omega), \tag{4.41}$$

where Ω is the resonant frequency of the device. Changes in temperature lead to changes in the speed of sound in the material, $c_s = \sqrt{E/\rho}$. Changes in temperature also cause changes in the device length through thermal expansion. For doubly clamped beams, this change in device length leads to stress. We rewrite Ω in terms of c_s:

$$\Omega = \frac{\beta^2 t}{L^2}\sqrt{\frac{c_s}{12}}, \tag{4.42}$$

where β is a constant that depends upon the mode number and whether the device is a cantilever or a doubly clamped beam. We take the partial derivative of Ω with respect to T and only consider the contribution from c_s.

$$\frac{\partial\Omega}{\partial T} = \frac{\partial\Omega}{\partial c_s}\frac{\partial c_s}{\partial T} = \frac{1}{2}\frac{\Omega}{c_s}\frac{\partial c_s}{\partial T} \tag{4.43}$$

Rearranging Equation 4.43 yields:

$$\frac{1}{\Omega}\frac{\partial\Omega}{\partial T} = \frac{1}{2}\frac{1}{c_s}\frac{\partial c_s}{\partial T}. \tag{4.44}$$

Next, we consider the effect of thermal expansion on the resonant frequency directly, through changes in t and L.

$$\frac{\partial\Omega}{\partial T} = \frac{\partial\Omega}{\partial L}\frac{\partial L}{\partial T} + \frac{\partial\Omega}{\partial t}\frac{\partial t}{\partial T} = -2\frac{\Omega}{L}\frac{\partial L}{\partial T} + \frac{\Omega}{t}\frac{\partial t}{\partial T} \tag{4.45}$$

We can simplify Equation 4.45 by using the definition of the coefficient of thermal expansion: $\alpha_T = \frac{1}{L}\frac{\partial L}{\partial T} = \frac{1}{t}\frac{\partial t}{\partial T}$.

$$\frac{1}{\Omega}\frac{\partial\Omega}{\partial T} = -\alpha_T \tag{4.46}$$

Finally, we consider the contribution from stress for doubly clamped beams. A change in temperature dT causes a change in device length. The change in device length induces a longitudinal extensional stress $\tau = -E\alpha_T dT$. The stress leads to a change in resonant frequency $\Omega(\tau)$.

$$\Omega^2(\tau) = \Omega^2(\tau = 0) + \frac{\tau}{\rho}\left(\frac{\beta}{L}\right)^2 \tag{4.47}$$

Taking the square root of Equation 4.47 yields:

$$\Omega(\tau) = \sqrt{\Omega^2(\tau = 0) + \frac{\tau}{\rho}\left(\frac{\beta}{L}\right)^2}. \tag{4.48}$$

We now take the derivative with respect to T.

$$\frac{\partial\Omega}{\partial T} = \frac{\partial\Omega}{\partial\tau}\frac{\partial\tau}{\partial T} = -\frac{1}{2}\frac{E}{\rho}\frac{\beta^2}{L^2}\frac{1}{\Omega}\alpha_T \tag{4.49}$$

Dividing both sides of Equation 4.49 by Ω yields:

$$\frac{1}{\Omega}\frac{\partial\Omega}{\partial T} = -\frac{1}{2}\frac{E}{\rho}\left(\frac{\beta}{\Omega L}\right)^2\alpha_T. \tag{4.50}$$

We combine Equations 4.44, 4.46, and 4.50 to find the total dependence on change in frequency due to change in temperature.

$$\frac{1}{\Omega}\frac{\partial\Omega}{\partial T} = \frac{1}{2}\frac{1}{c_s}\frac{\partial c_s}{\partial T} - \alpha_T - \frac{1}{2}\frac{E}{\rho}\left(\frac{\beta}{\Omega L}\right)^2\alpha_T \tag{4.51}$$

We combine Equations 4.40, 4.41, and 4.51:

$$\begin{aligned} S_{y,TF}(\omega) &= \left(\frac{1}{\Omega}\frac{\partial\Omega}{\partial T}\right)^2 S_T(\omega) \\ &= \left[\frac{1}{2}\frac{1}{c_s}\frac{\partial c_s}{\partial T} - \alpha_T - \frac{1}{2}\frac{E}{\rho}\left(\frac{\beta}{\Omega L}\right)^2 \alpha_T\right]^2 \frac{4}{\pi}\frac{k_B T^2/g}{1+\omega^2\tau_T^2}. \end{aligned} \tag{4.52}$$

We now find the phase noise due to temperature fluctuations, $S_{\phi,TF}(\omega)$.

$$S_{\phi,TF}(\omega) = \left(\frac{\Omega}{\omega}\right)^2 \left[\frac{1}{2}\frac{1}{c_s}\frac{\partial c_s}{\partial T} - \alpha_T - \frac{1}{2}\frac{E}{\rho}\left(\frac{\beta}{\Omega L}\right)^2 \alpha_T\right]^2 \frac{4}{\pi}\frac{k_B T^2/g}{1+\omega^2\tau_T^2} \tag{4.53}$$

We find the Allan deviation.

$$\sigma_{A,TF}(\tau_A) = \left|\frac{1}{2}\frac{1}{c_s}\frac{\partial c_s}{\partial T} - \alpha_T - \frac{1}{2}\frac{E}{\rho}\left(\frac{\beta}{\Omega L}\right)^2 \alpha_T\right| \sqrt{\frac{4}{\pi}\frac{k_B T^2}{g\tau_A}} \quad \text{for} \quad \tau_A \gg \tau_T \tag{4.54}$$

In order to accurately model temperature fluctuations in MEMS and NEMS, we must also consider how the properties of bulk Si change as the device layer becomes thinner. For silicon with a thickness of 300nm, the thermal conductivity is 90W/(m·K) [58] at room temperature, which is about 75% of the bulk value. Thinner layers have lower values of thermal conductivity. Using the lower thermal conductivity for thinner Si, we plot the phase noise due to thermomechanical motion and temperature fluctuation in Figure 4.6.

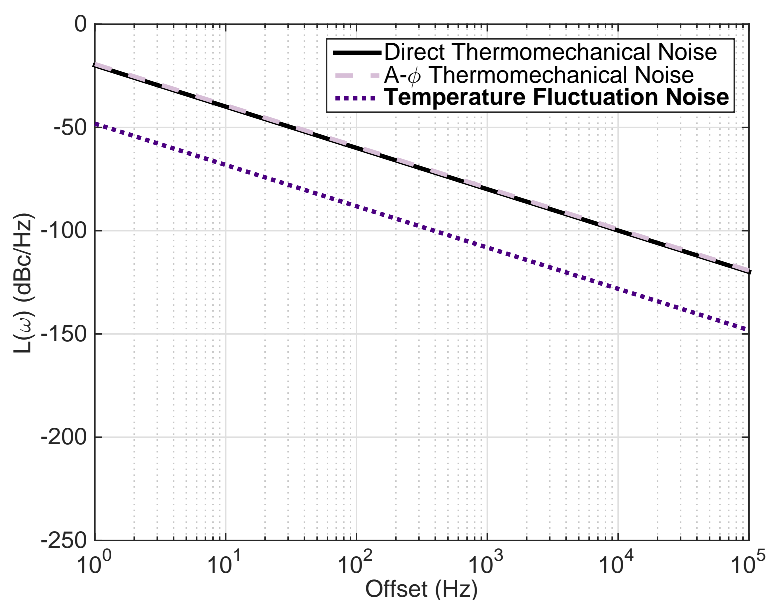

Figure 4.6: Comparison of phase noise from direct thermomechanical noise, amplitude to phase conversion thermomechanical noise, and temperature fluctuations.

Temperature fluctuation noise has a smaller magnitude than both contributions to thermomechanical noise, as well as a f^{-2} dependence, ruling it out as a candidate for APN.

Extensional Fluctuation Noise

Fluctuations in the geometry of the resonator due to finite temperature[1] are another possible source of frequency fluctuations. We find the fluctuations in the width of the device, which lead to fluctuations in the length of the device through Poisson's ratio. For a doubly clamped beam, we assume perfect clamping at the ends, which excludes extensional modes. However, we note that for a cantilever, the extensional modes would contribute. We begin by finding the mode shape and resonant frequencies of the extensional modes along the width of the doubly clamped beam. The governing

[1] unpublished work from J. Sader

equation [59] for the nth extensional mode is

$$ES\frac{\partial^2 u}{\partial y^2} - \mu\frac{\partial^2 u}{\partial t^2} = 0, \tag{4.55}$$

where E is the Young's modulus, $S = t \times L$ is the cross-sectional area, and $\mu = M/w = \rho S$ is the mass per unit length. The nth extensional mode has the following mode shape and resonant frequency:

$$u_n(y) = A_n \cos(\pi n y/w) \tag{4.56a}$$

$$\Omega_{e,n} = \sqrt{\frac{E}{\rho}}\frac{\pi n}{w}. \tag{4.56b}$$

We next find the frequency fluctuations due to fluctuations in the length of the nth extensional mode, $S_{A_n}(\omega)$. $S_{A_n}(\omega)$ has units of m^2/Hz. We follow a procedure similar to that used by Cleland and Roukes [52] to find the frequency fluctuations due to thermomechanical motion noise. From the Equipartition of Energy Theorem, the potential energy in the nth extensional mode is equal to $\frac{1}{2}k_B T$.

$$\langle \mathrm{PE_n} \rangle = \frac{1}{2}k_B T = \frac{ES}{2}\int_0^\infty \int_0^w \left(\frac{dv_n}{dy}\right)^2 S_{A_n}(\omega) dx d\omega, \tag{4.57}$$

where $v_n(y) = \cos(\pi n y/w)$. We first integrate over y.

$$\frac{1}{2}k_B T = (n\pi)^2 \frac{ES}{4w}\int_0^\infty S_{A_n}(\omega) d\omega \tag{4.58}$$

We assume that the extensional fluctuations of each mode are driven by a force noise with a spectral density of $S_{F_n}(\omega)$; we also assume that this noise is white. We use the simple harmonic oscillator approximation for the motion. $S_{A_n}(\omega)$ is then equal to the product of the SHO transfer function and the force noise.

$$S_{A_n}(\omega) = \frac{1}{(\Omega_{e,n}^2 - \omega^2)^2 + \left(\Omega_{e,n}^2/Q_{e,n}\right)^2}\frac{S_{F_n}(\omega)}{M_{eff,e}^2} \tag{4.59}$$

$Q_{e,n}$ is the quality factor of the nth extensional mode and $M_{eff,e}$ is the effective mass of the nth extensional mode. $M_{eff,e} = \frac{1}{2}M$ for all modes. We rewrite Equation

4.58.

$$\frac{1}{2}k_BT = (n\pi)^2\,\frac{ES}{w}\frac{S_{F_n}}{M_{eff,e}^2}\int_0^\infty \frac{1}{(\Omega_{e,n}^2-\omega^2)^2+\left(\Omega_{e,n}^2/Q_{e,n}\right)^2}d\omega \tag{4.60}$$

We integrate over ω to determine S_{F_n}.

$$\frac{1}{2}k_BT \approx (n\pi)^2\,\frac{ES}{w}\frac{S_{F_n}}{M_{eff,e}^2}\frac{\pi}{2}\frac{Q_{e,n}}{\Omega_{e,n}^3} \tag{4.61}$$

For $Q_{e,n} > 10$, the error due to the approximation is less than one percent. The approximation becomes exact in the limit of infinite $Q_{e,n}$. We find $S_{F_n}(\omega)$.

$$S_{F_n}(\omega) = \frac{k_BTwM_{eff,e}^2\Omega_{n,e}^3}{\pi^3n^2ESQ_{e,n}} \tag{4.62}$$

We combine Equations 4.59 and 4.62.

$$S_{A_n}(\omega) = \frac{1}{(\Omega_{e,n}^2-\omega^2)^2+\left(\Omega_{e,n}^2/Q_{e,n}\right)^2}\frac{4k_BT\Omega_{e,n}}{\pi MQ_{e,n}} \tag{4.63}$$

We next determine how the fluctuations in the width of the device lead to fluctuations in the frequency of the device. Since the ends of the beam are perfectly clamped, the change in width of the device leads to tension along the width of the device. The relationship between the strain along the width and the induced stress (tension) along the length of the beam is given by Equation 4.64 [53].

$$\tau = \sigma_{xx} = c_{xxyy}\epsilon_{yy}, \tag{4.64}$$

where c_{xxyy} =35.7 GPa. We previously determined the relationship between tension and Ω_0 during the discussion of temperature fluctuation noise.

$$\Omega(\tau) = \sqrt{\Omega^2(\tau=0)+\frac{\tau}{\rho}\left(\frac{\beta}{L}\right)}. \tag{4.65}$$

We find the change in resonant frequency due to fluctuations in the width of the device.

$$\frac{1}{\Omega}\frac{\partial\Omega}{\partial y} = \frac{\partial\Omega}{\partial\tau}\frac{\partial\tau}{\partial y} = \frac{1}{2}\frac{c_{xxyy}}{E}\frac{1}{w} \tag{4.66}$$

We find the fractional frequency noise and phase noise due to these extensional fluctuations.

$$S_{y,EF}(\omega) = \sum_{n=1}^{\infty} \left(\frac{1}{\Omega_0} \frac{\partial \Omega_0}{\partial w} \right)^2 S_{A,n}(\omega) \tag{4.67}$$

The fractional frequency noise is

$$S_{y,EF}(\omega) = \sum_{n=1}^{\infty} \frac{1}{(\Omega_{e,n}^2 - \omega^2)^2 + \left(\Omega_{e,n}^2/Q_{e,n}\right)^2} \frac{16 k_B T \Omega_{e,n} c_{xxyy}^2}{\pi M Q_{e,n} w^2 E^2}. \tag{4.68}$$

We use Equation 4.68 to find the phase noise, $S_{\phi,EF}(\omega) = \frac{\Omega_0^2}{\omega^2} S_{y,EF}(\omega)$.

$$S_{\phi,EF}(\omega) = \frac{16 k_B T \Omega_0^2 c_{xxyy}^2}{\pi M w^2 \omega^2 E^2} \sum_{n=1}^{\infty} \frac{\Omega_{e,n}}{Q_{e,n}} \frac{1}{(\Omega_{e,n}^2 - \omega^2)^2 + \left(\Omega_{e,n}^2/Q_{e,n}\right)^2} \tag{4.69}$$

No simple closed form expression exists for $S_{\phi,EF}(\omega)$. We consider two variables to determine a suitable approximation for $S_{\phi,EF}(\omega)$: the number of terms to include in the sum and the value for $Q_{e,n}$. We assume that all modes have the same quality factor, $Q_{e,n} = Q_e$. In Figure 4.7, we consider three different values of $Q_{e,n}$: 15, 100, and 1000. From Figure 4.7, we determine that the largest noise occurs with smallest Q. Also, the first three terms of the sum are sufficient to approximate $S_{\phi,EF}(\omega)$. Thus, we choose $Q_e = 15$ and limit the sum to the first three terms of $S_{\phi,EF}(\omega)$. Figure 4.8 compares the phase noise due to thermomechanical motion, temperature fluctuations, and extensional fluctuations.

We now find the Allan deviation due to extensional fluctuations. We choose to approximate the sum for $S_{\phi,e}(\omega)$ with just the first term of the sum.

$$S_{\phi,EF}(\omega) = \frac{16 k_B T \Omega_0^2 c_{xxyy}^2}{\pi M w^2 \omega^2 E^2} \frac{\Omega_{e,1}}{Q_{e,1}} \frac{1}{(\Omega_{e,1}^2 - \omega^2)^2 + \left(\Omega_{e,1}^2/Q_{e,1}\right)^2} \tag{4.70}$$

We further approximate $S_{\phi,e}(\omega)$ to simplify the calculation.

$$S_{\phi,EF}(\omega) \approx \frac{16 k_B T c_{xxyy}^2}{\pi Q_{e,1} M w^2 \Omega_{e,1}^3 E^2} \left(\frac{\Omega_0}{\omega} \right)^2 \quad \text{for} \quad \omega \ll \Omega_{e,1} \tag{4.71}$$

We then find the Allan deviation.

$$\sigma_{A,EF}(\tau_A) = \sqrt{\frac{16 k_B T c_{xxyy}^2}{Q_{e,1} M w^2 \Omega_{e,1}^3 E^2 \tau_A}} \tag{4.72}$$

$S_{\phi,EF}(\omega)$ has some of the qualities required for a candidate for APN. It is proportional to $k_B T$ and the noise is correlated between modes. However, it lacks the $1/f$ dependence required. Also, it is significantly smaller than the phase noise due to thermomechanical motion, ruling it out as a candidate for APN.

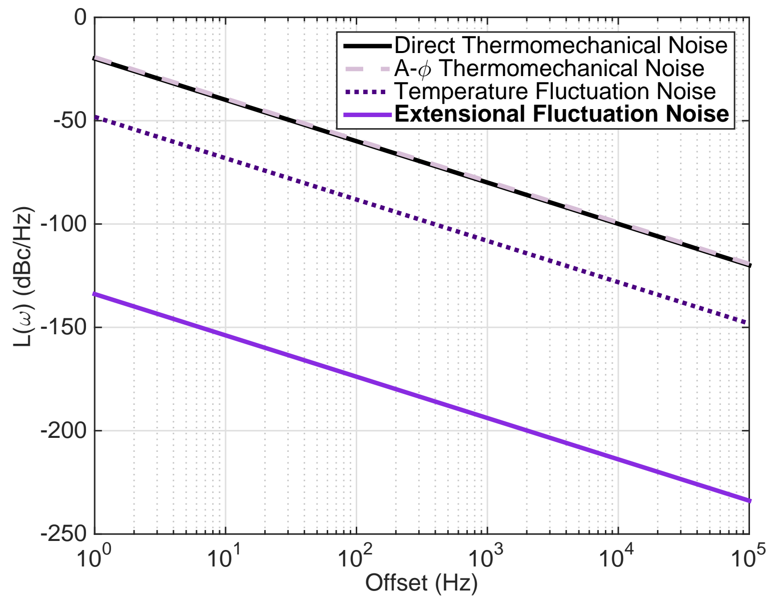

Figure 4.8: Comparison of phase noise from direct thermomechanical noise, amplitude to phase conversion thermomechanical noise, temperature fluctuations, and extensional fluctuations.

Charge Fluctuation Noise

Fluctuations in charges trapped in the device lead to frequency fluctuations through the electrostatic spring softening. We first find the electrostatic spring softening due to the trapped charges. Figure 4.9 shows the device geometry for the spring softening calculation.

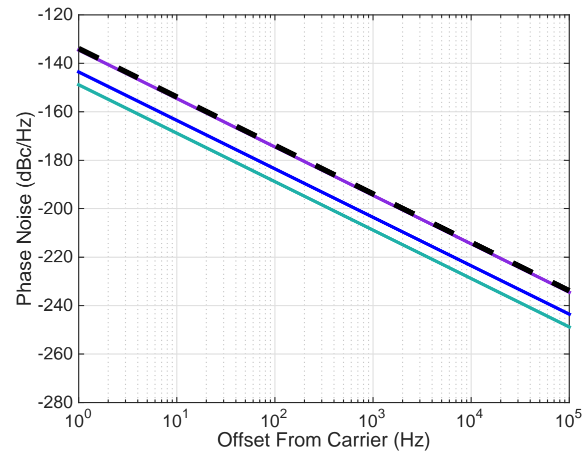

(a) $S_{\phi,EF}(\omega)$ for $Q_{e,n} = 15$

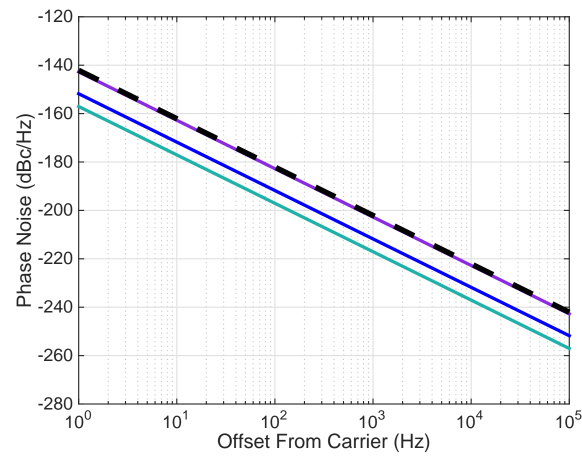

(b) $S_{\phi,EF}(\omega)$ for $Q_{e,n} = 100$

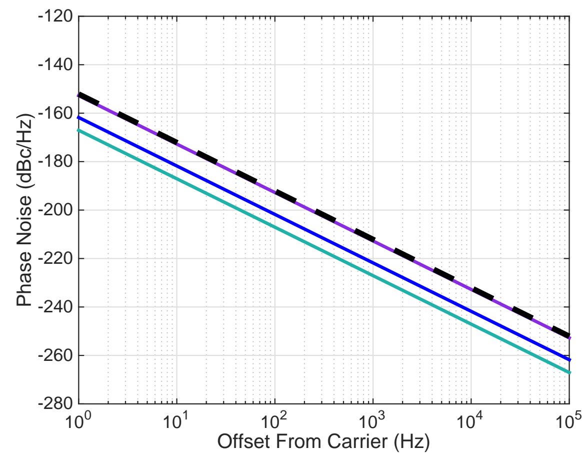

(c) $S_{\phi,EF}(\omega)$ for $Q_{e,n} = 1000$

Figure 4.7: Comparison of $Q_{e,n}$ values.

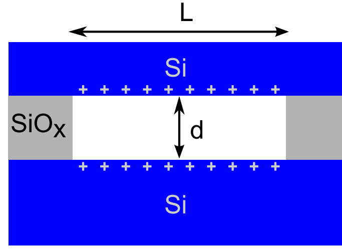

Figure 4.9: Silicon DCB of dimensions $L \times w \times t$ separated by a distance d from the silicon substrate.

Charges are trapped in the silicon-silicon oxide interface [60]. To determine the capacitance between the beam and the substrate, we model it as a parallel plate capacitor with a bias voltage V_{BIAS} applied.

$$C = \epsilon_0 \frac{wL}{d}, \tag{4.73}$$

where ϵ_0 is the permittivity of free space. The total voltage V across the plate is the sum of the bias voltage, V_{BIAS}, and the voltage due to the trapped charges, V_{TC}. The energy U_e stored in the capacitor is $\frac{1}{2}CV^2$. The electrostatic spring constant softening, k_e, is equal to $\frac{\partial^2 U_e}{\partial x^2}$.

$$k_e = \epsilon_0 \frac{wL}{2d^3} V^2 \tag{4.74}$$

We now find the frequency shift due to the trapped charges.

$$\Omega_0' = \Omega_0 \left(1 - \frac{k_e}{k_{eff}}\right)^{1/2} \tag{4.75}$$

We perform the Taylor series expansion of Equation 4.75:

$$\Omega_0' = \Omega_0 \left(1 - \frac{k_e}{2k_{eff}}\right) = \Omega_0 \left(1 - V^2 \frac{\epsilon_0 LW}{4k_{eff} d^3}\right) = \Omega_0 \left(1 - \xi V^2\right), \tag{4.76}$$

with $\xi = \frac{\epsilon_0 Lw}{4k_{eff} d^3}$.

We find the fractional frequency noise due to trapped charges using the Wiener-Khinchin theorem [38]; the Fourier transform of the autocorrelation of fluctuations

in the fractional frequency is equal to the spectral density of fractional frequency fluctuations. We first find the fractional frequency.

$$\frac{\partial \Omega_0'}{\partial V} = -2\Omega_0'\xi V \tag{4.77}$$

$$\frac{\delta \Omega_0'}{\Omega_0'} = -2\xi V \delta V \tag{4.78}$$

We then find the autocorrelation function.

$$G_{CF}(\tau) = 4\xi^2 \left\langle V(t)\delta V(t) V(t+\tau)\delta V(t+\tau)\right\rangle \tag{4.79}$$

We assume that the bias voltage applied is constant and that $V_{BIAS} \gg V_{TC}$. V_{TC} is determined by sweeping V_{BIAS} and measuring the resulting frequency shift. The vertex of the resulting parabola corresponds to V_{TC}. For native oxide, $\langle V_{TC}\rangle \approx -1.8$ mV [60]. We rewrite $G(\tau)$:

$$G_{CF}(\tau) = \left\langle \frac{\delta \Omega_0'(t)\delta\Omega_0'(t+\tau)}{\left(\Omega_0'\right)^2}\right\rangle = 4\xi^2 V_{BIAS}\left\langle \delta V_{TC}(t)\delta V_{TC}(t+\tau)\right\rangle \tag{4.80}$$

$$G_{CF}(\tau) = 4\xi^2 V_{BIAS} H(\tau) \tag{4.81}$$

where $H(\tau)$ is the autocorrelation function of $\langle \delta V_{TC}(t)\delta V_{TC}(t+\tau)\rangle$. We then take the Fourier transform to determine the fractional frequency noise.

$$S_{y,CF}(\omega) = 4\xi^2 V_{BIAS}^2 \int_{-\infty}^{\infty} H(\tau)e^{-i\omega\tau}d\tau \tag{4.82}$$

We then find the phase noise.

$$S_{\phi,CF}(\omega) = 4\xi^2 V_{BIAS}^2 \left(\frac{\Omega_0}{\omega}\right)^2 \int_{-\infty}^{\infty} H(\tau)e^{-i\omega\tau}d\tau \tag{4.83}$$

Up to this point, we have made no assumptions about $H(\tau)$. We now assume that the noise has a $1/f$ dependence. We also assume that there is no bias voltage applied; only the built in voltage is present, which corresponds to the actuation and detection methods used in Chapter 6. We also assume that the magnitude of the fluctuation is equal to the mean built in voltage; this represents a worst case scenario.

$$S_{\phi,CF}(\omega) = 4\xi^2 V_{TC}^4 \frac{\Omega_0^2}{\omega^3} \tag{4.84}$$

We then find the Allan deviation.

$$\sigma_{A,CF}(\tau_A) = \sqrt{8\xi^2 V_{TC}^4 \ln(2)} \tag{4.85}$$

We plot $S_{\phi,CF}(\omega)$ for the test device in Figure 4.10. While $S_{\phi,CF}(\omega)$ does have the $1/f$ dependence of APN, the magnitude is not large enough. Also, APN should be proportional to V_{BIAS}^2 for devices driven electrostatically; however, the measured Allan deviation is independent of V_{BIAS} [26].

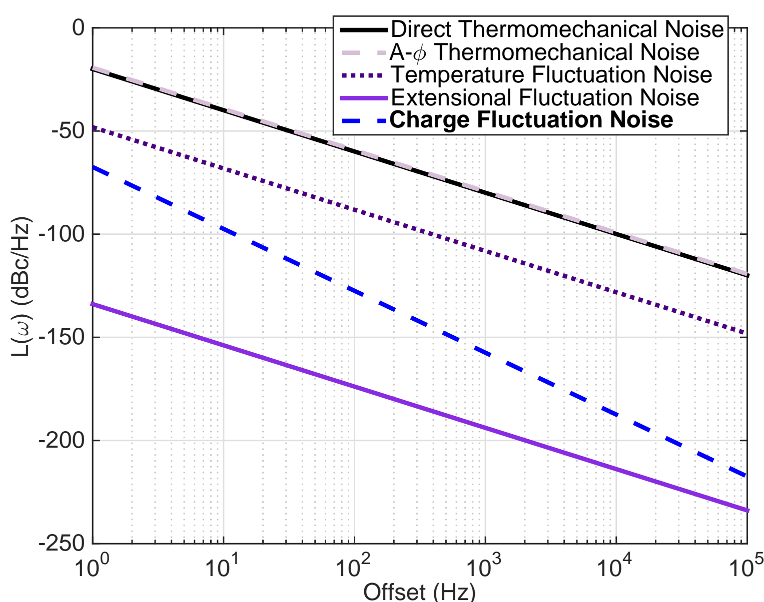

Figure 4.10: Comparison of phase noise from direct thermomechanical noise, amplitude to phase conversion thermomechanical noise, temperature fluctuations, extensional fluctuations, and charge fluctuations.

Gas Interaction Noise

Gas adsorbing or desorbing from the device surface and gas diffusing along the device surface both lead to frequency fluctuations by changing the instantaneous mass of the device. These processes occur simultaneously. However, we model them as two separate processes.

Adsorption Desorption Noise

Following Yong and Vig [61] and Cleland and Roukes [52], we treat the adsorption-desorption process as a two state Markov chain. The surface of the resonator has N_{AD} sites available for adsorption. We find the fractional frequency change due to adsorption desorption at one site and then extrapolate to the whole device. We assume that each site contributes equally to the phase noise. We begin by finding the adsorption rate, r_A, and desorption rate, r_D. We assume only one species of atom or molecule is producing the noise. The species has a binding energy ϵ_B, a mass m, and a pressure p. For this calculation, we assume that the primary species of gas in the vacuum chamber is H_2, because we baked out the chamber, as described in Chapter 5. We assume a pressure of 10^{-9} Torr. The surface involved in both adsorption-desorption and diffusion noise is native oxide on Si. We assume an ϵ_B of 1 eV [62], which corresponds to chemisorption, and $\nu_D = 10^{13}$ Hz. The molecular diameter of H_2 is 0.274 nm [9]. The molecular weight of H_2 is m =2.016 amu [9]. The adsorption rate [63] is

$$r_A = sI\frac{A_D}{N_{AD}}, \tag{4.86}$$

where s is the sticking coefficient, I is the flux of molecules impinging on the device, and $A_D = L \times w$ is the area of the device exposed to the gas. We rewrite Equation 4.86 in terms of the flux, $I = p/\sqrt{2\pi m k_B T}$.

$$r_A = s\frac{A_D}{N_{AD}}\frac{p}{(2\pi m k_B T)^{1/2}} \tag{4.87}$$

For this calculation, we assume a worst case scenario of $s = 1$. $N_{AD} = \frac{A_D}{A_{AD}}$, where A_{AD} is the area occupied by an adsorbed gas molecule. The desorption rate is

$$r_D = \nu_D e^{\left(-\frac{\epsilon_B}{k_B T}\right)}, \tag{4.88}$$

where ν_D is the attempt frequency. For the given parameters, $r_A = 1.1 \times 10^{-3}$ Hz and $r_D = 1.6 \times 10^{-4}$ Hz. The probability that a site is occupied is p_{occ}.

$$p_{occ} = \frac{r_A}{(r_A + r_D)} \tag{4.89}$$

The variance in the occupation probability is σ_{occ}^2.

$$\sigma_{occ}^2 = \frac{r_A r_D}{(r_A + r_D)^2} \tag{4.90}$$

The autocorrelation for a two state Markov chain is

$$G_{AD,site}(\tau) = \sigma_{occ}^2 e^{-|\tau|/\tau_r}, \tag{4.91}$$

where $\tau_R = (r_A + r_D)^{-1} = 810$ s. The fractional frequency noise at one site is equal to the Fourier transform of Equation 4.91.

$$S_{AD,site}(\omega) = \frac{2\sigma_{occ}^2 \tau_R}{1 + (\omega\tau_R)^2} \tag{4.92}$$

We determine the fractional frequency noise for the device by multiplying $S_{AD,site}$ by the number of sites N_{AD} and the fractional change in frequency induced by a molecule, $\delta\omega/\Omega_0 = -(m/2M_{eff})$.

$$S_{y,AD}(\omega) = \frac{2N_{AD}\sigma_{occ}^2 \tau_R}{1 + (\omega\tau_R)^2} \left(\frac{m}{2M_{eff}}\right)^2 \tag{4.93}$$

We now find the phase noise due to adsorption-desorption noise.

$$S_{\phi,AD}(\omega) = \frac{2N_{AD}\sigma_{occ}^2 \tau_R}{1 + (\omega\tau_R)^2} \left(\frac{m}{2M_{eff}}\right)^2 \left(\frac{\Omega_0}{\omega}\right)^2 \tag{4.94}$$

We note that since $\omega\tau_R \gg 1$, $S_{\phi,AD}(\omega) \propto \omega^{-4}$. The Allan deviation due to adsorption-desorption has two asymptotes.

$$\sigma_{A,AD}(\tau_A) = \frac{1}{2}\sigma_{occ}\sqrt{N_{AD}}\left(\frac{m}{M}\right)\left(\frac{\tau_R}{\tau_A}\right)^{\frac{1}{2}} \quad \text{for} \quad \tau_A \gg \tau_R \tag{4.95a}$$

$$\sigma_{A,AD}(\tau_A) = \frac{1}{2\sqrt{3}}\sigma_{occ}\sqrt{N_{AD}}\left(\frac{m}{M}\right)\left(\frac{\tau_A}{\tau_R}\right)^{\frac{1}{2}} \quad \text{for} \quad \tau_A \ll \tau_R \tag{4.95b}$$

We plot the phase noise due to adsorption-desorption in Figure 4.11. We conclude that noise due to adsorption-desorption is not a valid candidate for APN. The magnitude is smaller than that of thermomechanical motion. In addition, it has the wrong power-law dependence in frequency.

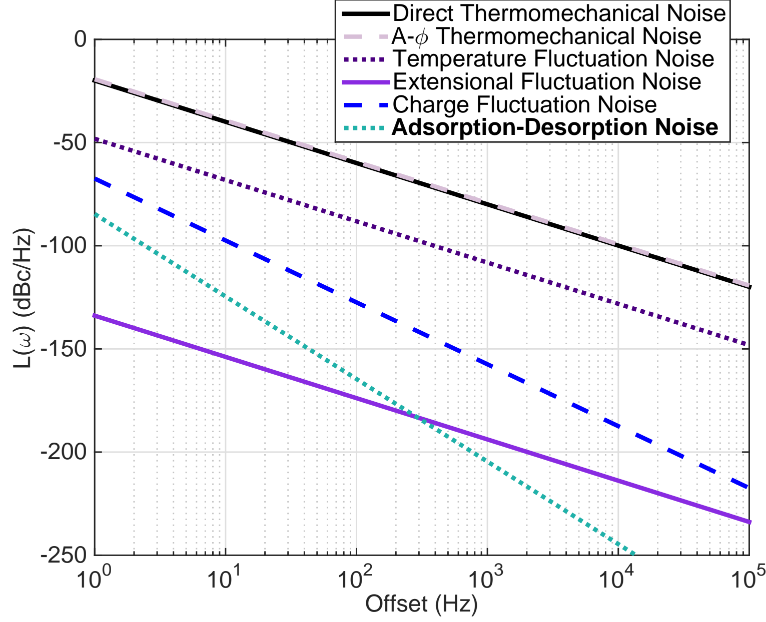

Figure 4.11: Comparison of phase noise from direct thermomechanical noise, amplitude to phase conversion thermomechanical noise, temperature fluctuations, extensional fluctuations, charge fluctuations, and adsorption-desorption.

Diffusion Noise

Following Yang et al. [64], we find the phase noise due to atoms diffusing along the surface of the resonator. We first determine how the diffusion of atoms along the surface of the device changes the fractional frequency, $y(t)$.

$$y(t) = \frac{\delta f(t)}{f_0} = -\frac{1}{2}\frac{m}{M_{eff}}\frac{\int_{-L/2}^{L/2} [u(x)]^2 \, \delta C(x,t) dx}{\frac{1}{L}\int_{-L/2}^{L/2} [u(x)]^2 \, dx}, \tag{4.96}$$

where $u(x)$ is the mode shape and $\delta C(x,t)$ is the concentration fluctuation due to diffusion. $\delta C(x,t)$ is governed by the one-dimensional diffusion equation.

$$\frac{\partial \delta C(x,t)}{\partial t} = D\frac{\partial^2 \delta C(x,t)}{\partial x^2}, \tag{4.97}$$

where D is the diffusion constant. From Zangwill [62], $D = D_0 e^{-\epsilon_m/k_BT}$, where D_0 is on the order of 10^{-3} cm^2/s and ϵ_m ranges between 5% and 20% of ϵ_B for chemisorption. We choose $E_m = 0.1$ eV. We then find the autocorrelation of $y(t)$.

$$G_{DF}(\tau) = \frac{aN}{\sqrt{2\pi}} \left(\frac{m}{2M_{eff}}\right)^2 \frac{1}{\sqrt{1+\tau/\tau_{DF}}} \tag{4.98}$$

where $a = 4.428$, N is the average number of atoms diffusing across the device, and $\tau_{DF} = L^2/(2a^2D)$ =0.031 s is the diffusion time.[2] a is a numerical constant that comes from approximating the mode shape as a Gaussian to simplify the calculations. We use the Wiener-Khinchin Theorem to find the fractional frequency noise by taking the Fourier transform of Equation 4.98.

$$S_{y,DF}(\omega) = \frac{aN}{2} \left(\frac{m}{M_{eff}}\right)^2 \tau_{DF}\psi(\omega\tau_{DF}) \tag{4.99}$$

$$\psi(x) = \frac{g(\sqrt{x})}{\sqrt{x}} \tag{4.100}$$

$$g(\sqrt{x}) = \cos(x) + \sin(x) - 2C_1(\sqrt{X})\cos(x) - 2S_1(\sqrt{x})\sin(x) \tag{4.101}$$

$$C_1(x) = \sqrt{\frac{2}{\pi}} \int_0^x \cos\left(u^2\right) du \tag{4.102}$$

$$S_1(x) = \sqrt{\frac{2}{\pi}} \int_0^x \sin\left(u^2\right) du \tag{4.103}$$

$C_1(x)$ and $S_1(x)$ are Fresnel integrals. $\psi(x)$ has two asymptotes:

$$\psi(x) \approx \begin{cases} \dfrac{1}{\sqrt{x}} & \text{for } x \ll 1, \\ \dfrac{1}{\sqrt{2\pi}}\dfrac{1}{x^2} & \text{for } x \gg 1. \end{cases} \tag{4.104}$$

Figure 4.12 shows $\psi(x)$ and its asymptotes.

[2] τ_{DF} is usually referred to as τ_D in the literature. We have chosen to use τ_{DF} instead in order to reserve τ_D for defect reorientation time, as will be discussed in Section 4.4.

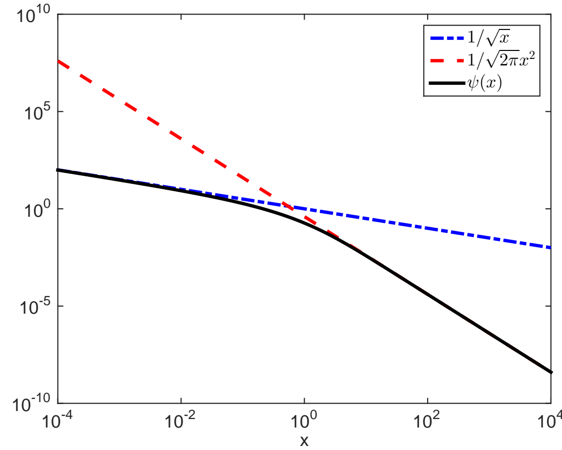

Figure 4.12: Asymptotes of $\psi(x)$.

We now consider the two asymptotes for $S_{y,DF}(\omega)$.

$$S_{y,DF}(\omega) = \begin{cases} \dfrac{aN}{2}\left(\dfrac{m}{M_{eff}}\right)^2 \sqrt{\dfrac{\tau_{DF}}{\omega}} & \text{for } \omega \gg 1/\tau_{DF} \\ \dfrac{aN}{2\sqrt{2\pi}}\left(\dfrac{m}{M_{eff}}\right)^2 \dfrac{1}{\omega^2 \tau_{DF}} & \text{for } \omega \ll 1/\tau_{DF} \end{cases} \tag{4.105}$$

The phase noise for diffusion noise has the following two asymptotes:

$$S_{\phi,DF}(\omega) = \begin{cases} \dfrac{aN}{2}\left(\dfrac{m}{M_{eff}}\right)^2 \left(\dfrac{\Omega_0}{\omega}\right)^2 \sqrt{\dfrac{\tau_{DF}}{\omega}}, & \text{for } \omega \gg 1/\tau_{DF} \\ \dfrac{aN}{2\sqrt{2\pi}}\left(\dfrac{m}{M_{eff}}\right)^2 \dfrac{\Omega_0^2}{\omega^4 \tau_{DF}} & \text{for } \omega \ll 1/\tau_{DF}. \end{cases} \tag{4.106}$$

The Allan deviation for diffusion noise has the following two asymptotes:

$$\sigma_{A,DF}(\tau_A) \approx \begin{cases} 0.83\sqrt{N}\left(\dfrac{m}{M}\right)\left(\dfrac{\tau_{DF}}{\tau_A}\right)^{\frac{1}{4}} & \text{for } \tau_A \gg \tau_{DF}, \\ 0.26N\left(\dfrac{m}{M}\right)^2\left(\dfrac{\tau_A}{\tau_{DF}}\right) & \text{for } \tau_A \ll \tau_{DF}. \end{cases} \tag{4.107}$$

We plot the phase noise due to diffusion in Figure 4.13. We conclude that diffusion noise is not a valid candidate for APN. It is not larger than thermomechanical motion noise. It also lacks the f^{-3} frequency dependence in phase noise expected for a candidate for APN.

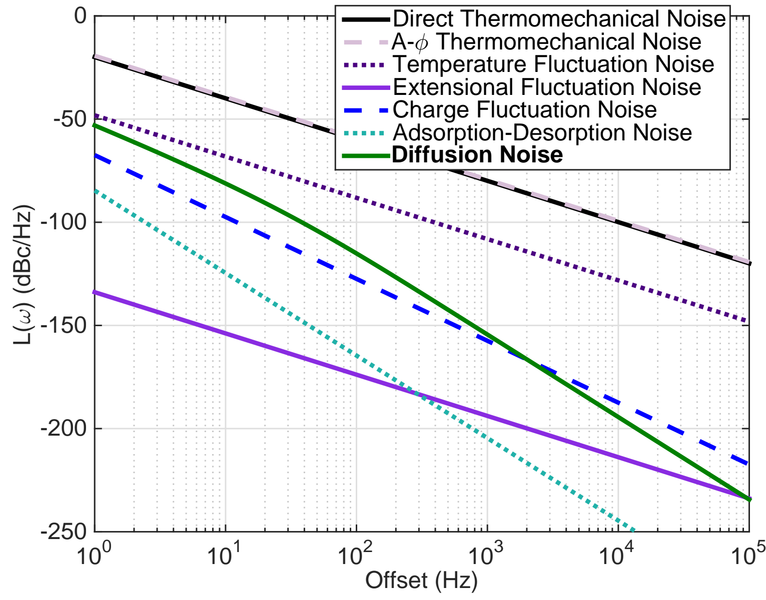

Figure 4.13: Comparison of phase noise from direct thermomechanical noise, amplitude to phase conversion thermomechanical noise, temperature fluctuations, extensional fluctuations, charge fluctuations, adsorption-desorption, and diffusion.

Noise from Higher Order Mode Coupling

In Section 4.3, we described the phase noise due to the nonlinear spring constant, $\lambda_{1,1}$. In this section, we describe the phase noise due to thermomechanical amplitude noise from higher modes. The thermomechanical amplitude noise couples into the first mode through the nonlinear coupling coefficient, $\lambda_{1,q}$. We are interested in the noise from the second mode. We begin by finding $\Phi_1(\xi)$ and $\Phi_2(\xi)$. $\Phi_n(\xi)$, the nth mode of a doubly clamped beam, has the following mode shape [57]:

$$\Phi_n(\xi) = C_n \left[\cosh(k_n\xi) - \cos(k_n\xi) + \frac{\cosh(k_n\xi) - \cos(k_n\xi)}{\sinh(k_n) - \sin(k_n)} \left(\sin(k_n\xi) - \sinh(k_n\xi)\right) \right]. \tag{4.108}$$

C_n is defined such that $\int_0^1 \Phi_p(\xi)\Phi_q(\xi)\mathrm{d}\xi = 1$. k_n is defined by the following boundary condition: $\cos(k_n)\cosh(k_n) = 1$. We list the values for C_n and q_n for the first two modes of a doubly clamped beam in Table 4.5. Using these parameters, we find $\lambda_{1,2} = 2.09 \times 10^{13}\ \mathrm{m}^{-2}$.

Mode Number	C_n	k_n
1	1	4.730
2	1	7.853

Table 4.5: Mode Shape Parameters

We now find the fractional frequency noise. The fractional frequency is

$$y(t) = \frac{\Delta\Omega(t)}{\Omega_0} = \lambda_{1,2} A_2^2(t), \tag{4.109}$$

where $A_2^2(t)$ is the amplitude squared for the second mode. We find the autocorrelation function.

$$\begin{aligned} G_{MC}(\tau) &= \langle y(t) y(t+\tau) \rangle \\ &= \lambda_{1,2}^2 \langle A_2^2(t) A_2^2(t+\tau) \rangle \end{aligned} \tag{4.110}$$

We use the Wiener-Khinchin theorem to find the fractional frequency noise by taking the Fourier transform of Equation 4.110.

$$S_{y,MC}(\omega) = \lambda_{1,2}^2 \int_{-\infty}^{\infty} \langle A_2^2(t) A_2^2(t+\tau) \rangle e^{-i\omega\tau} \mathrm{d}\tau \tag{4.111}$$

We assume that the motion in the second mode is driven by thermomechanical noise. For the experiments performed in Chapter 6, this is a reasonable assumption. However, for mass spectrometry measurements employing multi-mode imaging [4, 65, 66], the amplitudes in the higher order modes are often large; the amplitudes should be measured and an autocorrelation performed. We rewrite Equation 4.111, using the expression for $S_x^{th}(\omega)$ from Equation 2.20.

$$S_{y,MC}(\omega) = \left(\frac{4 k_B T Q \lambda_{1,2}}{M_{eff,2} \Omega_2^3} \right)^2 \tag{4.112}$$

$\Omega_2/(2\pi) = 2.756$ MHz is the resonant frequency of the second mode. $M_{eff,2} = 0.439M$ is the effective mass of the second mode. We then find the phase noise.

$$S_{\phi,MC}(\omega) = \left(\frac{\Omega_0}{\omega} \right)^2 \left(\frac{4 k_B T Q \lambda_{1,2}}{M_{eff,2} \Omega_2^3} \right)^2 \tag{4.113}$$

We plot the phase noise in Figure 4.14.

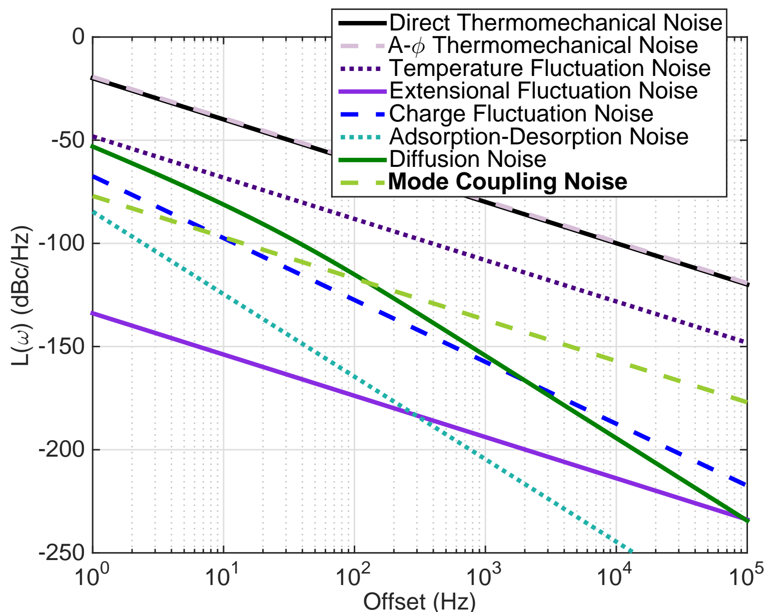

Figure 4.14: Comparison of phase noise from direct thermomechanical noise, amplitude to phase conversion thermomechanical noise, temperature fluctuations, extensional fluctuations, charge fluctuations, adsorption-desorption, diffusion, and non-linear mode coupling.

Non-linear mode coupling is not a viable candidate for APN for several reasons. It has a magnitude much smaller than that of thermomechanical noise. It also lacks the correct temperature and frequency dependencies.

Defect Motion Noise

The reorientation of point defects leads to fluctuations in the local Young's modulus and, consequently, fluctuations in the frequency. Cleland and Roukes [52] provided an initial model for noise from point defects. They treated the defects as elastic dipoles, as first discussed by Nowick and Berry [67]. Cleland and Roukes modeled the dipoles with a single activation energy, ϵ_D[3]. We summarize their results in Section 4.4 and then expand their model to include a range of activation ener-

[3] We have chosen use ϵ to denote energy avoid confusion with the Young's modulus, E

gies in Section 4.4. We first discuss elastic dipoles before considering how their reorientation leads to phase noise.

Elastic Dipoles

Following Nowick and Berry [67], a point defect causes local distortions in the strain field. The change in strain field due to an elastic dipole is

$$\epsilon_{ij}^{d} - \epsilon_{ij}^{0} = \sum_{p=1}^{n_{\mathrm{d}}} \lambda_{ij}^{(p)} C_{P}. \tag{4.114}$$

ϵ_{ij}^{d} is the strain tensor for a crystal with defects and ϵ_{ij}^{0} is the strain tensor for a crystal without defects. n_{d} is the number of equivalent orientations for a defect; n_{d} depends upon both the defect type and the crystal symmetry. $\lambda_{ij}^{(p)}$ characterizes the elastic dipole; the definition of $\lambda_{ij}^{(p)}$ is given in Equation 4.115. Defects can have equivalent orientations; p labels which equivalent orientation of n_{d} that the defect occupies. C_p denotes the mole fraction of defects with orientation p.

$$\lambda_{ij}^{(p)} \equiv \frac{\partial \epsilon_{ij}}{\partial C_p} \tag{4.115}$$

Defect Motion Noise with One Activation Energy

Roukes and Cleland treat point defects as elastic dipoles with one activation energy, ϵ_D. The defects are randomly oriented in the crystal. Thermal motion induces reorientation of the defects, with a reorientation time of τ_D.

$$\tau_D = \tau_0 \exp(\epsilon_D / k_B T), \tag{4.116}$$

where τ_0 is the attempt time, and ϵ_D is energy required for reorientation. For silicon, τ_0 is on the order of 10^{-12} s and ϵ_D ranges from 0.1 – 0.4 eV [68]. Roukes and Cleland limit the defect to two orientations, + and -, which both have the same reorientation energy. The probability that a defect is in either orientation is $\frac{1}{2}$; the mean reorientation time is τ_D.

Roukes and Cleland next determine the effect of the point defects on the bulk Young's modulus. When the defect is in the + orientation, the local Young's modulus is $E_s + E_+$, where E_s is the defect free modulus. The Young's modulus corresponding to the − orientation is $E_s + E_-$. They assume that a total mole faction C_0 of identical defects exist in the device. The average Young's modulus is $\langle E \rangle \approx E_s + \frac{1}{2}C_0\left(E_- + E_+\right)$. The variance is $\sigma_E^2 \approx \frac{1}{4}C_0\left(E_+ - E_-\right)^2$. The corresponding variance in frequency is $\sigma_\Omega^2 = \frac{1}{8}C_0\left(\Omega_+ - \Omega_-\right)^2$, where $\Omega_\pm$ is calculated using $E = E_s + C_0 E_\pm$. The fractional frequency noise is

$$S_{y,RC}(\omega) = \frac{2}{\pi}\frac{\sigma_\Omega^2}{\langle \Omega \rangle^2}\frac{\tau_D}{1 + \omega^2\tau_D^2}. \tag{4.117}$$

The corresponding phase noise is

$$S_{\phi,RC}(\omega) = \left(\frac{\Omega_0}{\omega}\right)^2 \frac{2}{\pi}\frac{\sigma_\Omega^2}{\langle \Omega \rangle^2}\frac{\tau_D}{1 + \omega^2\tau_D^2}. \tag{4.118}$$

In order to find the Allan deviation, they assume that $\tau_D \ll \tau_A$.

$$\sigma_A(\tau_A) = \sqrt{\frac{2\sigma_\Omega^2}{\langle \Omega \rangle^2}}\sqrt{\frac{\tau_D}{\tau_A}} \quad \text{for} \quad \tau_A \gg \tau_D \tag{4.119}$$

The model for defect motion postulated by Roukes and Cleland does not produce a noise source consistent with APN. However, their model is not realistic because defects have a range of activation energies. We consider a model for defect motion that incorporates a range of activation energies in the next section.

Defect Motion with a Range of Activation Energies

We modify Roukes and Cleland's model to include a range of reorientation times through the Dutta-Dimon-Horn model [39, 40]. Following Scofield et al. [69], we treat defect reorientation as a superposition of thermally activated processes. We begin by modeling the fluctuation in the local Young's modulus due to the reorientation of one elastic dipole, $\delta\tilde{E}$. We use $\tilde{E}$ to refer to the local Young's

modulus for one defect. We reserve E for the Young's modulus for the entire sample. We find the autocorrelation of $\delta\tilde{E}$, $G_{\tilde{E}}(t)$.

$$G_{\tilde{E}}(t) = \langle \delta\tilde{E}(0)\delta\tilde{E}(t)\rangle = \langle \delta\tilde{E}^2\rangle e^{-|t|/\tau_D}, \tag{4.120}$$

where τ_D is the is the relaxation time and $\langle \delta\tilde{E}^2\rangle$ is the variance. We use the Wiener-Khinchin Theorem to find the power spectral density, $S_{\tilde{E}}(\omega)$.

$$S_{\tilde{E}}(\omega) = \langle \delta\tilde{E}^2\rangle \frac{2\tau_D}{1+\omega^2\tau_D^2} \tag{4.121}$$

We now find the fluctuations due to linear superposition of all of the defects.

$$S_E(\omega) = \sum_j \langle \delta\tilde{E}_j^2\rangle \frac{2\tau_{D,j}}{1+\omega^2\tau_{D,j}^2} \tag{4.122}$$

$\langle \delta\tilde{E}_j^2\rangle$ is the variance of the jth elastic dipole and $\tau_{D,j}$ is the relaxation time of that dipole. The fractional frequency dependence due to changes in E is

$$\frac{1}{\Omega_0}\frac{\partial\Omega_0}{\partial E} = \frac{1}{2}\frac{1}{E}. \tag{4.123}$$

The fractional frequency noise is $S_{y,E}(\omega) = \left(\frac{1}{\Omega_0}\frac{\partial\Omega_0}{\partial E}\right)^2 S_E(\omega)$.

$$S_{y,E}(\omega) = \frac{1}{4}\frac{1}{E^2}\sum_j \langle \delta\tilde{E}_j^2\rangle \frac{2\tau_{D,j}}{1+\omega^2\tau_{D,j}^2} \tag{4.124}$$

We use Equation 4.124 to find the phase noise, $S_{\phi,E}(\omega) = \frac{\Omega_0^2}{\omega^2}S_{y,E}(\omega)$.

$$S_{\phi,E}(\omega) = \frac{1}{4}\frac{1}{E^2}\frac{\Omega_0^2}{\omega^2}\sum_j \langle \delta\tilde{E}_j^2\rangle \frac{2\tau_{D,j}}{1+\omega^2\tau_{D,j}^2} \tag{4.125}$$

Up to this point, we have made no assumptions about the distribution of $\tau_{D,j}$. We first consider the temperature dependence of $S_E(\omega)$ through $\tau_{D,j}$ and $\langle \delta\tilde{E}_j^2\rangle$. The temperature dependence of $\tau_{D,j}(T)$ is

$$\tau_{D,j}(T) = \tau_{0,j}e^{\epsilon_{D,j}/k_BT}. \tag{4.126}$$

Scofield et al. choose to factor out the temperature dependence of $\langle \delta \tilde{E}_j^2 \rangle$, by writing $\langle \delta \tilde{E}_j^2 \rangle$ as the product of the temperature dependent variance of Young's modulus, $\langle \delta E^2(T) \rangle$ and the dimensionless variance of the jth fluctuator, $\langle \delta s_j^2 \rangle$.

$$\langle \delta \tilde{E}_j^2 \rangle = \langle \delta E^2(T) \rangle \langle \delta s_j^2 \rangle, \tag{4.127}$$

By factoring out the temperature dependence of $\langle \delta \tilde{E}_j^2 \rangle$, we focus on the temperature dependence due to the thermally activated process. We normalize $S_E(\omega)$ to remove the dependence on $\langle \delta \tilde{E}_j^2 \rangle$.

The normalized spectrum is $S_{E,n}(\omega)$.

$$S_{E,n}(\omega) = \sum_j \langle \delta s_j^2 \rangle \frac{2\tau_{D,j}}{1 + \omega^2 \tau_{D,j}^2} \tag{4.128}$$

We next define a temperature dependent distribution of relaxation times, $F(\tau, T)$, in order to remove the sum over $\langle \delta s_j^2 \rangle$ from Equation 4.128.

$$F(\tau, T) = \sum_j \langle \delta s_j^2 \rangle \delta \left(\tau - \tau_j \left(T \right) \right) \tag{4.129}$$

We rewrite $S_{E,n}(\omega)$ in terms of $F(\tau, T)$.

$$S_{E,n}(\omega, T) = \int_0^\infty F(\tau, T) \frac{2\tau}{(1 + \omega^2 \tau^2)} d\tau \tag{4.130}$$

$F(\tau, T)$ arises from a distribution of activation energies, $D(\epsilon)$, where $\epsilon = k_B T \ln \left(\frac{\tau}{\tau_0} \right)$.

$$D(\epsilon) = \sum_j \langle \delta s_j^2 \rangle \delta \left(\epsilon - \epsilon_j \left(T \right) \right) \tag{4.131}$$

We rewrite $F(\tau, T)$ in terms of $D(\epsilon)$.

$$F(\tau, T) = \frac{k_B T D(\epsilon)}{\tau}, \tag{4.132}$$

where $\tau = \tau_0 e^{\epsilon / k_B T}$. We limit the distribution by allowing one activation time, τ_0, and a range of activation energies. Given a distribution of energies and an attempt time, we can calculate $S_{E,n}(\omega)$. Before finding the phase noise due to defect

reorientation, we consider the inverse problem: extracting $D(\epsilon)$ and τ_0 from a phase noise spectrum.

We find $D(\epsilon)$ and τ_0 by determining $F(\tau, T)$ from the measured phase noise, $S_\phi(\omega)$. Following Scofield et al. [69], we first convert $S_\phi(\omega)$ into a fractional frequency noise spectrum and normalize it, which yields $S_{E,n}(\omega)$. We find $F(\tau, T)$ by inverting Equation 4.130.

$$F(\tau, T) = -\frac{1}{\pi\tau^2} \operatorname{Im}\left[S_{E,n}\left(\frac{i}{\tau}\right)\right] \tag{4.133}$$

At this point, we assume that $S_{E,n}(\omega)$ has the form $\omega^{-\alpha}$, with $\alpha \approx 1$.

$$\frac{\omega}{\pi} S_{E,n}(\omega) \approx \tau F\left(\tau, T\right), \tag{4.134}$$

with $\tau = 1/\omega$. This approximation is valid when the product of ω and $S_{E,n}(\omega)$ varies by less than 50% per decade; the error introduced is less than 50%. Thus, for a given $S_\phi(\omega)$, it is possible to determine $S_{E,norm}(\omega)$, $F\left(\tau, T\right)$, and $D(\epsilon)$. $D(\epsilon)$ could then be compared with the known defects in Si and determine if the spectrum represents defect motion.

To model $S_{\phi,E}(\omega)$ for comparison with the other sources of phase noise, we choose a defect with a reorientation energy of 0.056eV, a reorientation time of 1×10^{-13}s, a concentration of 0.001, and $E_\pm = \pm 0.0001$E. The reorientation time and reorientation energy correspond to the divacancy in Si[70]. The defect concentration is a guess based upon material choice of single crystal silicon; the total number of defects should be relatively low. The change in the Young's modulus is an educated guess. The defect concentration and value for $E_\pm$ do not change the shape of $S_{\phi,E}(\omega)$; they only change the magnitude. We model $D(\epsilon)$ as a Gaussian with a standard deviation of 0.05eV. The resulting phase noise is shown in Figure 4.15. The magnitude of $S_{\phi,E}(\omega)$ is significantly less than the other sources of phase noise and does not show up on the plot. A defect with a longer reorientation time, on the order of a few microseconds, does produce phase noise on the order of the other

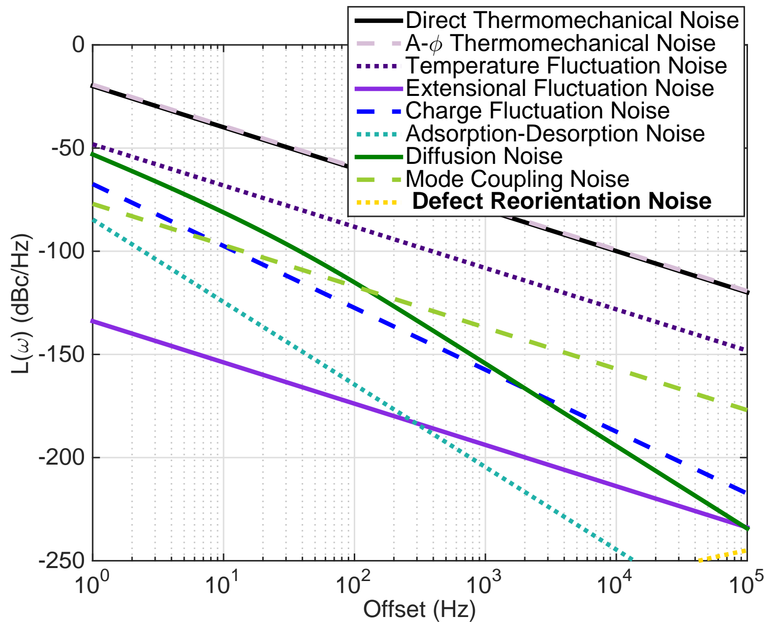

Figure 4.15: Comparison of phase noise from direct thermomechanical noise, amplitude to phase conversion thermomechanical noise, temperature fluctuations, extensional fluctuations, charge fluctuations, adsorption-desorption, diffusion, non-linear mode coupling, and defect reorientation noise.

noise sources. Due to the complicated nature of $S_{\phi,E}(\omega)$, we do not calculate the Allan deviation; however, in regions where $S_{\phi,E}(\omega) \propto \omega^{-3}$, the Allan deviation is independent of the integration time, τ_A. Defect reorientation noise is a potential candidate for anomalous phase noise, with the caveat that both the magnitude and frequency of defect reorientation noise are highly dependent upon the parameters chosen.

4.5 Summary of Phase Noise Sources

In summary, we have considered several sources of phase noise in NEMS resonators in this chapter. Table 4.6 contains equations for the phase noise for the various sources. Table 4.7 contains equations for the Allan deviation for the various sources. The majority of the sources of phase noise considered in this chapter are not viable candidates for APN. Direct thermomechanical and amplitude to phase $(A-\phi)$ thermomechanical noise are intrinsic noise sources. Temperature fluctuation

noise lacks the expected frequency dependence; it is also smaller than direct thermomechanical noise over the region of interest. Length fluctuation lacks the expected frequency dependence; it is smaller than direct thermomechanical noise as well. While charge fluctuation noise does have the expected frequency dependence, it is significantly smaller than direct thermomechanical noise. Neither gas interaction noise source has the expected frequency dependence; both are smaller than direct thermomechanical noise over the majority of the region of interest. Mode coupling noise lacks the expected frequency dependence; its magnitude is also significantly smaller than that of direct thermomechanical noise. Defect reorientation noise is a potential candidate for anomalous phase noise due to its temperature dependence ($S_{\phi,E}(T) \propto T$) and its frequency dependence ($S_{\phi,E}(\omega) \propto \omega^{-3}$).

Table 4.6: Summary of Sources of Phase Noise

Noise Source		Equation	ω dependence
Thermomechanical-Direct	$S_{\phi,direct}(\omega)$	$= \frac{1}{2\pi}\frac{\Omega_0}{\omega^2}\frac{1}{a^2}\frac{k_B T\tilde{\alpha}_0}{\left(M_{eff}\Omega_0^2\right)^2}$	-2
Thermomechanical $A-\phi$	$S_{\phi,A-\phi}(\omega)$	$\frac{1}{2\pi}\frac{\Omega_0}{\omega^2}\left(\frac{3}{2}a+\frac{1}{a^2}\cos(\Delta)\right)^2\frac{k_B T\tilde{\alpha}_0}{\left(M_{eff}\Omega_0^2\right)^2}$	-2
Temperature Fluctuations	$S_{\phi,TF}(\omega)$	$= \left(\frac{\Omega_0}{\omega}\right)^2\left[\frac{1}{2}\frac{1}{c_s}\frac{\partial c_s}{\partial T}-\alpha_T-\frac{1}{2}\frac{E}{\rho}\left(\frac{\beta}{\Omega L}\right)^2\alpha_T\right]^2\frac{4}{\pi}\frac{k_B T^2/g}{1+\omega^2\tau_T^2}$	-2[a]
Extensional Fluctuations	$S_{\phi,EF}(\omega)$	$\approx \frac{16k_B T c_{xxyy}^2}{\pi Q_{e,1} M E^2 w^2 \Omega_{e,1}^3}\left(\frac{\Omega_0}{\omega}\right)^2$	-2
Charge Fluctuations	$S_{\phi,CF}(\omega)$	$= 4\xi^2 V_{TC}^4\frac{\Omega_0^2}{\omega^3}$	-3
Adsorption-Desorption	$S_{\phi,AD}(\omega)$	$= \frac{2N_{AD}\sigma_{occ}^2\tau_R}{1+(\omega\tau_R)^2}\left(\frac{m}{2M_{eff}}\right)^2\left(\frac{\Omega_0}{\omega}\right)^2$	-2
Diffusion	$S_{\phi,DF}(\omega)$	$= \frac{aN}{2}\left(\frac{m}{M_{eff}}\right)^2\left(\frac{\Omega_0}{\omega}\right)^2\sqrt{\frac{\tau_{DF}}{\omega}}$	$-\frac{1}{2}$[b]
Higher Order Mode Coupling	$S_{\phi,MC}(\omega)$	$= \left(\frac{\Omega_0}{\omega}\right)^2\left(\frac{4k_B T Q\lambda_{1,2}}{M_{eff,2}\Omega_2^3}\right)^2$	-2
Defect Motion	$S_{\phi,D}(\omega)$	$\propto \frac{k_B T}{\omega^3}$	-3

[a] $\omega\tau_T \ll 1$
[b] $\omega \gg 1/\tau_{DF}$

Table 4.7: Summary of Allan Deviation

Noise Source		Equation	τ dependence
Thermomechanical Direct	$\sigma_{A,TM}(\tau_A)$	$= \sqrt{\frac{1}{2\tau_A}\frac{1}{a^2}\frac{k_B T\tilde{\alpha}_0}{\left(M_{eff}\Omega_0^2\right)^2}}$	$-\frac{1}{2}$
Thermomechanical $A-\phi$	$\sigma_{A,A-\phi}(\tau_A)$	$= \sqrt{\frac{1}{2\tau_A}\left(\frac{3}{2}a + \frac{1}{a^2}\cos(\Delta)\right)^2 \frac{k_B T\tilde{\alpha}_0}{\left(M_{eff}\Omega_0^2\right)^2}}$	$-\frac{1}{2}$
Temperature Fluctuations	$\sigma_{A,TF}(\tau_A)$	$= \left\lvert \frac{1}{2}\frac{1}{c_s}\frac{\partial c_s}{\partial T} - \alpha_T - \frac{1}{2}\frac{E}{\rho}\left(\frac{\beta}{\Omega L}\right)^2 \alpha_T \right\rvert \sqrt{\frac{4}{\pi}\frac{k_B T^2}{g\tau_A}}$	$-\frac{1}{2}$[a]
Extensional Fluctuations	$\sigma_{A,EF}(\tau_A)$	$= \sqrt{\frac{16 k_B T c_{xxyy}^2}{Q_{e,1} M E^2 w^2 \Omega_{e,1}^3 \tau_A}}$	$-\frac{1}{2}$
Charge Fluctuations	$\sigma_{A,CF}(\tau_A)$	$= \sqrt{8\xi^2 V_{TC}^4 \ln(2)}$	none
Adsorption-Desorption	$\sigma_{A,AD}(\tau_A)$	$= \frac{1}{2\sqrt{3}}\sigma_{occ}\sqrt{N_{AD}}\left(\frac{m}{M}\right)\left(\frac{\tau_A}{\tau_R}\right)^{\frac{1}{2}}$	$\frac{1}{2}$[b]
Diffusion	$\sigma_{A,DF}(\tau_A)$	$\approx 0.83\sqrt{N}\left(\frac{m}{M}\right)\left(\frac{\tau_{DF}}{\tau_A}\right)^{\frac{1}{4}}$	$-\frac{1}{4}$[c]
Higher Order Mode Coupling	$\sigma_{A,MC}(\tau_A)$	$= \frac{4 k_B T Q \lambda_{1,2}}{M_{eff,2}\Omega_2^3}\sqrt{\frac{\pi}{\tau_A}}$	$-\frac{1}{2}$
Defect Motion	$\sigma_{A,E}$	$=$ constant	none

[a] $\tau_A \gg \tau_T$
[b] $\tau_A \ll \tau_R$
[c] $\tau_A \gg \tau_{DF}$

Chapter 5

EXPERIMENTAL SETUP

In this chapter, we describe the setup used in Chapter 6 to measure the temperature dependence of anomalous phase noise in silicon doubly clamped beams, as well as the fabrication of those devices. The experimental setup consists of five parts: the optics used to detect the motion of the device, the optics used to actuate the motion of the device, the optics used to anneal the device, the vacuum system containing the cryostat and the device, and the cryostat and sample holder used to cool the device.

We begin the chapter with a brief overview of the entire optical setup. We then discuss concepts from optics relevant to the design and operation of the optical setup. We next describe each subsystem of the optical setup in detail. We end with a description of the procedure used to fabricate the devices.

5.1 Overview of Optical Setup

The optical setup consists of three subsystems: the detection system, the actuation system, and the annealing system. The detection system uses a simple interferometer to detect the motion of the device. The actuation system uses an amplitude modulated laser beam to thermoelastically actuate the device. The annealing system uses a laser to anneal the device. All three subsystems and their associated optics are mounted on a 4’x8’x1’ RS4000 Newport optical table, supported by a set of I-2000 isolator legs. The optical setup is shown in Figure 5.1.

5.2 Optical System Design

Before discussing the optical setup in greater detail, we provide a brief overview of topics relevant to the system. First, we discuss Gaussian laser beams and spot

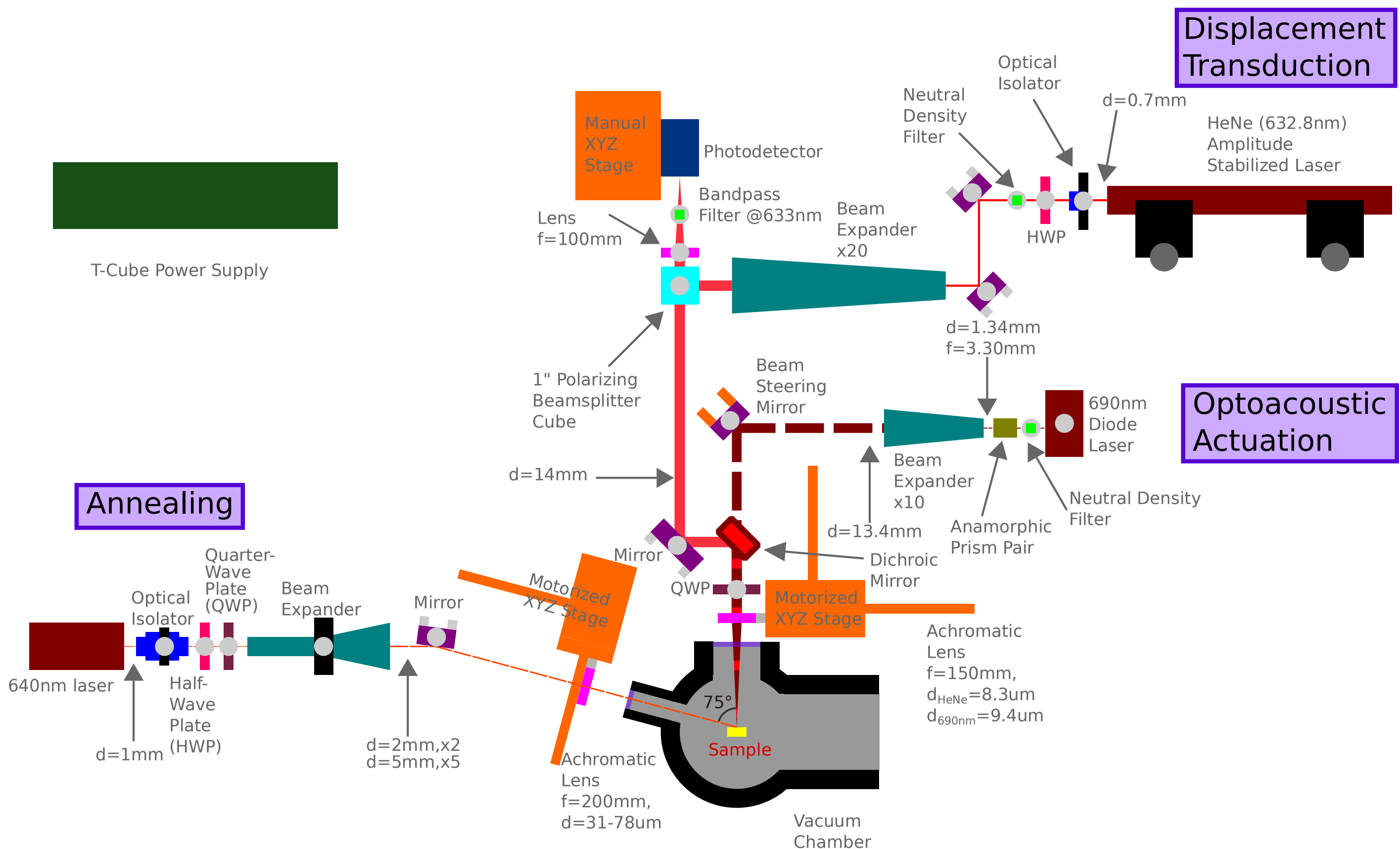

Figure 5.1: Schematic of the optical setup. The optical setup consists of three subsystems: the detection beam from the HeNe (632.8nm) laser, the actuation beam from the 690nm diode laser, and the annealing beam from the 640nm laser. The beam diameters are labeled at various points in the system.

size; the spot size at the device is directly correlated to the responsivity of the simple interferometer. We discuss optical aberrations and how the choice of lens used to focus the beam on the device affects the minimum spot size, as well as the requirements on the flatness of the dichroic mirror. We then discuss polarization optics.

Gaussian Laser Beams

A Gaussian laser beam is defined by its Gaussian intensity profile, given in Equation 5.1 [71]:

$$I(r) = I_o e^{-2r^2/w^2}, \tag{5.1}$$

where w is the beam radius at which $I = I_0 e^{-2}$. The laser beam diverges; the beam waist $w(z)$ depends upon the distance from the exit of the laser, as given in Equation 5.2 [71]:

$$w(z) = w_0 \left[1 + \left(\frac{\lambda z}{\pi w_0^2} \right)^2 \right]^{1/2}, \tag{5.2}$$

where w_0 is the beam radius at the exit of the laser, λ is the wavelength of the beam, and z is the distance from the exit of the laser.

Spot Size

The spot size of the laser at the device is of great interest, for both optical detection and optical actuation. The responsivity of the detection system, the ratio of the voltage measured at the photodetector to the amplitude of the motion of the device, is directly proportional to the spot size for the detection beam. For a constant spot size, the responsivity of the optical system decreases as the device width decreases. We wish for the spot size at the device to be as small as possible, to ensure that a large portion of the beam reflects off of the device, which leads to the best responsivity. As we will show in Section 5.4, the amount of power required for optical actuation depends upon the spot size of the laser.

We first consider the simple case of a circular beam traveling through an ideal lens and then consider the more complicated cases of Gaussian beams and of a lens with aberrations. The circular beam has a diameter D and uniform intensity distribution and passes through a lens with a focal length f. The lens is ideal with no aberrations. In this case, the minimum spot size is set by the diffraction limit. The minimum spot size is given by the diameter of the Airy disk:

$$s = 2.44\frac{\lambda f}{D}, \tag{5.3}$$

where λ is the wavelength of light [71]. For the detection beam, the distance between the exit of the laser and the input to the beam expander is approximately 16″. Using Equation 5.2, the $1/e^2$ beam radius at the input to the beam expander is 0.42mm. The beam radius at the exit is 8.4mm; the beam diameter is 16.8mm. The spot size predicted by Equation 5.3 is $13.8\mu m$, assuming a uniformly illuminated beam of diameter 16.8mm and an ideal lens with a focal length of 150mm. However, the beams used in these experiments have a Gaussian intensity profile. In addition, the beams are clipped; for 100% of the incident power to be passed by any element in the optical system, such as the mirrors or polarizing beam splitter, would require that the element be infinite. A simple criterion for apertures in the system is that they are circular with a diameter of $3w$, where w is the $1/e^2$ beam radius [72]. This condition leads to 98.9% of the incident power being passed through the aperture. Using the $3w$ criterion, the optics in the system should have a diameter of at least 25.2mm, which is a little less than 1". Next, we define the truncation ratio $T = w/b$, where b is the radius of the aperture. For these calculations, we use an aperture of diameter 22.6mm, the clear aperture of the quarter wave plate (QWP). Following Urey [73], the spot size s for a truncated Gaussian beam is

$$s = K\frac{\lambda f}{2b} \quad \text{with} \tag{5.4a}$$

$$K = 1.654 - \frac{0.105}{T} + \frac{0.28}{T^2}. \tag{5.4b}$$

K is defined such that diffraction spot diameter contains $1/e^2$ of the beam intensity. For the given beam $1/e^2$ diameter of 16.8 mm and aperture of 22.6 mm, the predicted spot size is 8.5 μm. The measured spot size is $(9.7 \pm 0.1)\mu m$.

We measured the spot size with the knife edge technique [74]. We used a computer controlled stage to move a razor blade across the beam, with the razor blade perpendicular to the beam, and measured the transmitted power with a photodetector. The coordinate system used is shown in Figure 5.2. The knife edge measurement is shown in Figure 5.3. We rewrite the equation for the intensity of a Gaussian laser

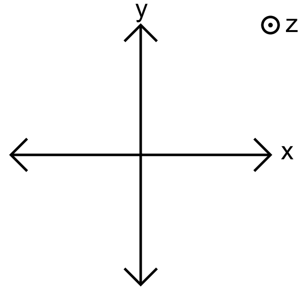

Figure 5.2: The focal plane is the x-y plane. The laser beam travels along the z-axis.

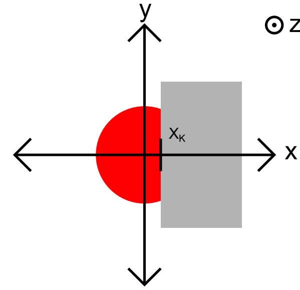

Figure 5.3: The razor blade moves along the x-axis.

beam in terms of x and y instead of r.

$$I(x, y) = I_0 e^{-2\left[\left(\frac{x - x_0}{w_x}\right)^2 + \left(\frac{y - y_0}{w_y}\right)^2\right]}, \tag{5.5}$$

where I_0 is the intensity, w_x is the beam width in the x direction, w_y is the beam width in the y direction, and (x_0, y_0) is the location of the center of the beam. The power, $P(x_K)$, measured at a given knife edge position, x_K, is given by Equation 5.6.

$$P(x_K) = \int_{-\infty}^{x_K} \left[\int_{-\infty}^{\infty} I_0 e^{-2\left[\left(\frac{x-x_0}{w_x}\right)^2 + \left(\frac{y-y_0}{w_y}\right)^2\right]} \mathrm{d}y \right] \mathrm{d}x \tag{5.6}$$

We integrate over y, yielding the following equation:

$$P(x_K) = \frac{\pi}{4} w_x w_y I_0 \left[\operatorname{erf}\left(\frac{\sqrt{2}(x - x_K)}{w_x} \right) + 1 \right], \tag{5.7}$$

where erf(x) is the Gaussian error function. We use Equation 5.7 to fit $P(x_K)$ and thus determine w_x. We took scans along the focal length, x and z or y and z to determine w_x and w_y. The data and fit used to determine w_x and w_y are shown in Figures 5.4 and 5.5.

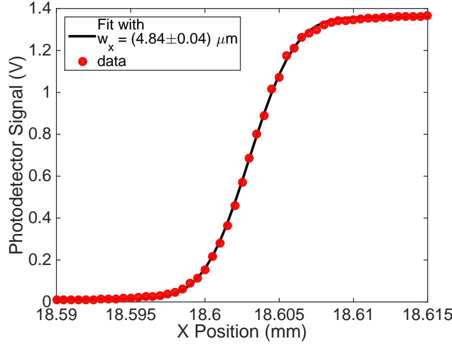

Figure 5.4: Data from knife edge measurement of w_x.

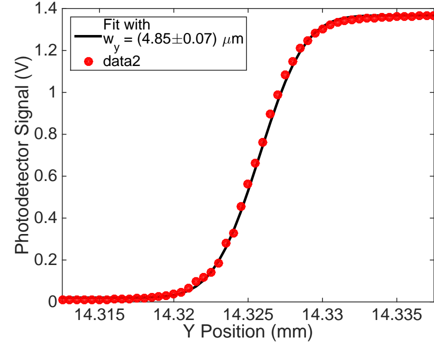

Figure 5.5: Data from knife edge measurement of w_y.

A second parameter of interest is the depth of focus, Δz, the distance over which the image can be moved before an accepted level of blur is produced [75]. Specifically, the depth of focus sets the range over which the device is in best focus and sets the focal length step size used when performing alignment scans to determine the best position for the lens relative to the device. We chose a Strehl ratio of 0.8 as the criterion used to calculate the depth of focus; the ratio is the ratio of the maximum intensity in the observation plane to the maximum intensity at the focal plane. A Strehl ratio of 0.8 corresponds to a peak-valley optical path difference of $\lambda/4$, the Rayleigh criterion. The optical path difference (OPD) is the difference between the real wavefront and an ideal spherical reference wavefront due to aberration [16]. The Rayleigh criterion [75] specifies that if the OPD is less than or equal to $\lambda/4$, the performance of the system will be almost ideal. Following Urey [73],

$$\Delta z = K_2 \lambda \left[\frac{f}{2b}\right]^2 \quad \text{with} \tag{5.8a}$$

$$K_2 = 2.05 + \frac{0.12}{T} - \frac{0.28}{T^2} + \frac{0.22}{T^3}. \tag{5.8b}$$

For the previous parameters, $K_2 = 2.24$ and the depth of focus is $\Delta z = 62\ \mu$ m.

Aberrations

We next consider the various aberrations present in an optical system. In order to generate the smallest spot size possible, we want the system to be diffraction limited; the blur due to diffraction should be much larger than the blur due to geometrical aberrations [16]. Specifically, we wish for the system to meet the Rayleigh criterion discussed in the previous section; the peak-valley optical path difference (OPD) should be less than $\lambda/4$. The majority of the components in the system introduce a wavefront error of less than $\lambda/4$; the OPD is specified for each part as a design parameter. However, two sources of aberration exist in the system: the lens used to focus the HeNe laser and 690nm laser onto the device, as well as the aberration from the dichroic mirror.

There are two types of aberrations [71]: chromatic aberrations and monochromatic aberrations. The chromatic aberrations arise from the wavelength dependence of the index of refraction of the materials used in the lens. The monochromatic aberrations correspond to higher order corrections to the paraxial approximation. The paraxial approximation uses the small angle approximation, $\sin(\phi) \approx \phi$, to simplify the calculation for ray tracing. We consider only the third order corrections to the paraxial approximation, also known as the Seidel aberrations: spherical aberration, coma, astigmatism, Petzval field curvature, and distortion. We do not consider Petvzal field curvature and distortion in the discussion of aberrations; both lead to deformation of the image off of the optical axis and we are primarily interested in the image close to the optical axis. Before considering these aberrations, we show a ray tracing for an ideal lens in Figure 5.6. All of the rays focus at the paraxial focus; the focal position is independent of the aperture at which the rays enter the lens.

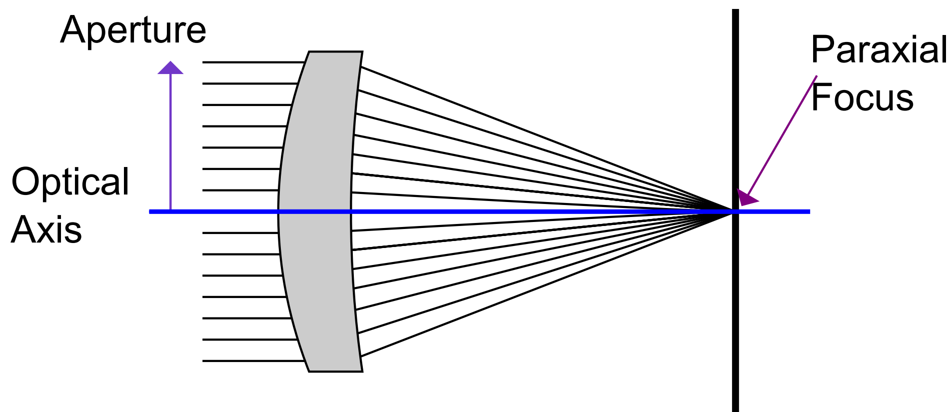

Figure 5.6: A ray trace showing an ideal lens.

Spherical aberration causes the focal length for a ray to depend the aperture, the height above the optical axis at which it enters the lens. A ray trace for a lens with spherical aberration is shown in Figure 5.7.

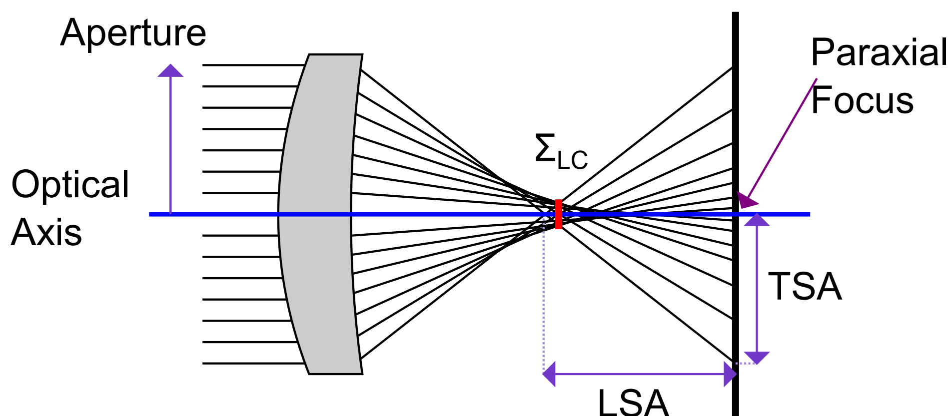

Figure 5.7: A ray trace showing spherical aberration. The optical axis is the blue line. The circle of least confusion, Σ_{LC}, is marked by the red line.

The circle of least confusion is the location of the minimum blur. Spherical aberration is characterized by the longitudinal spherical aberration (LSA) and the transverse spherical aberration (TSA). The longitudinal spherical aberration corresponds to the distance between where the ray crosses the optical axis and the paraxial focus. The transverse spherical aberrations corresponds to height of the ray above the op-

tical axis at the paraxial focus. We wish to minimize spherical aberration because it increases the spot size; we want the system to be diffraction limited.

The next monochromatic aberration is coma, which affects object points off of the optical axis. We are concerned with coma for the 690nm actuation beam, because we move the beam by changing the angle at which it hits the focusing lens; the beam is not parallel to the optical axis of the focusing lens, unlike the HeNe beam. The position above the optical axis at which the ray enters the lens changes the effective focus length, which leads to coma. An example of coma is shown in Figure 5.8.

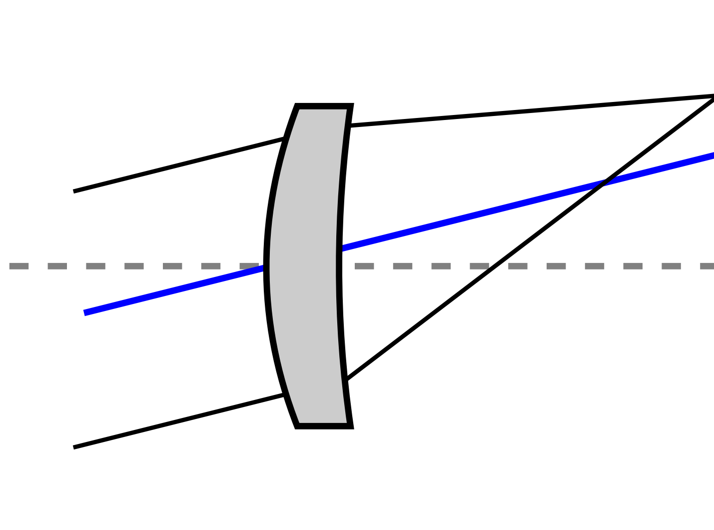

Figure 5.8: A ray tracing showing coma.

Astigmatism corresponds to the a focal length difference between the meridional plane and the sagittal plane for object points off of the optical axis. The meridional plane is the plane we have considered previously in the lens diagrams; it contains the optical axis and the ray that passes through the center of the aperture. The sagittal plane is perpendicular to this plane. The circle of least confusion corresponds to the smallest spot size; it is between the focus in the meridional plane and the focus in the sagittal plane. The 690nm actual beam has intrinsic astigmatism from the laser diode; we wish to limit the astigmatism added by the focusing lens.

Chromatic aberration arises from the wavelength dependence of the index of refraction. We are interested in the chromatic aberration of the lens used to focus both the 690nm and 633nm beams onto the device. We want the distance between the two focal points to be small. We use an achromatic doublet[1] to minimize the chromatic aberration. In addition, the achromatic doublet minimizes both spherical aberration and coma.

The other primary source of aberration in the optical system is the dichroic mirror. We used a custom dichroic mirror coated by Spectral Products with a flatness of $\lambda/8$ to ensure that the Rayleigh criterion was met. We had previously used a dichroic mirror that did not meet the Rayleigh criterion, which led to problems with both optical actuation and optical detection. We previously had to use higher beam powers for the 690nm beam due to the increased spot size. We also had a lower responsivity due to the increased spot size of the 633nm beam.

Polarization

The polarized light is used in both the detection system and the annealing system. In the detection system, the polarization of light is used control the amount of light passed into each path from the polarized beam splitter. In the annealing system, the annealing beam impinges upon the sample at Brewster's angle to maximize the amount of power adsorbed by the device.

Three orientations exist for the polarization of light: linear, circular, and elliptical [71]. For linearly polarized light, the electric field is oriented along a single direction in the plane perpendicular to the direction of propagation. One example of a linearly polarized electric field of amplitude E_0 propagating along the z axis in vacuum with wavelength λ is

$$\mathbf{E}(z,t) = \hat{\mathbf{x}} E_0 \cos(k_L z - \omega_L t), \tag{5.9}$$

[1] Thorlabs AC508-150-A-ML

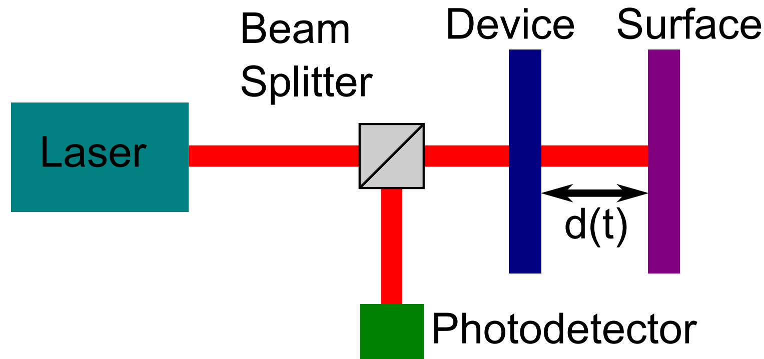

Figure 5.9: Simple interferometer. The interferometer measures d(t), the distance between the device and the surface underneath the device.

where $k_L = 2\pi/\lambda$ is the propagation number and $\omega_L = 2\pi c/\lambda$ is the frequency of the light. For circularly polarized light, both components have equal amplitudes and a $-\pi/2$ phase difference.

$$\mathbf{E} = E_0[\hat{\mathbf{x}}\cos(kz - \omega t) + \hat{\mathbf{y}}\sin(kz - \omega t)]. \tag{5.10}$$

For elliptically polarized light, the two components have different amplitudes and an arbitrary phase difference.

$$\mathbf{E} = [E_x\hat{\mathbf{x}}\cos(kz - \omega t) + E_y\hat{\mathbf{y}}\sin(kz - \omega t + \phi)]. \tag{5.11}$$

5.3 Detection System

We detect the motion of the device using a simple interferometer. The simple interferometer measures the path difference, $d(t) = d_0 + A\cos(\omega_D t)$, between the device and the surface underneath the device, where d_0 is the initial distance between the device and surface, A is the amplitude of the motion, and ω_D is the frequency of the motion. A simplified diagram of the interferometer showing the key components is shown in Figure 5.9. The light from the laser passes through the beam splitter before entering the vacuum chamber through the front window, which is not shown in the figure. The light is then reflected from the device and travels to the photodetector. The reflectance of the front window is $\approx 0.5\%$; the

front window is composed of quartz with a broadband anti-reflective coating[2]. Due to the low reflectance, we treat the interference as a two component process, where E_1 is the electric field reflected from the device and E_2 is the electric field reflected from the surface underneath the device. Assuming that the two electric fields are linearly polarized with parallel polarization, they have the following form at $z = z_0$, the location of the device:

$$\mathbf{E}_1(z_0, t) = \mathbf{E}_{01} e^{i(k_L z_0 - \omega_L t)}, \tag{5.12a}$$

$$\mathbf{E}_2(z_0, t) = \mathbf{E}_{02} e^{i(k_L (z_0 + 2d) - \omega_L t)}. \tag{5.12b}$$

$k_L = 2\pi/\lambda$ is the wavevector and $\omega_L = 2\pi c/\lambda$ is the frequency of the light. We are interested in the interference of these two fields.

$$\mathbf{E} = \mathbf{E_1} + \mathbf{E_2} \tag{5.13a}$$

$$\mathbf{E}^2 = \mathbf{E} \cdot \mathbf{E} \tag{5.13b}$$

$$\mathbf{E(t)}^2 = \mathbf{E}_1^2 + \mathbf{E}_2^2 + 2(\mathbf{E}_{01} \cdot \mathbf{E}_{02}) \cos\left(\frac{4\pi d(t)}{\lambda}\right) \tag{5.13c}$$

We rewrite the interference in terms of the intensity, the quantity measured by the photodetector.

$$I(t) = I_1 + I_2 + 2\sqrt{I_1 I_2} \cos\left(\frac{4\pi d(t)}{\lambda}\right). \tag{5.14}$$

In Figure 5.10, we plot the interference pattern for λ =632.8nm, the wavelength of the HeNe beam. We assume that $I_1 = I_2 = \frac{1}{4} I_0$. The highest responsivity occurs when $d = (2n + 1)\lambda/8$, where n is an integer. We use a photodetector to measure this intensity. The time varying intensity measured with the photodetector is proportional to $\sin(4\pi d(t)/\lambda)$, assuming that we are operating at the point with highest responsivity. We use the small angle approximation to linearize the voltage.

$$V(t) \propto \frac{4\pi d(t)}{\lambda} \tag{5.15}$$

This approximation is valid for $d < 5$ nm.

[2] The window is model number VPZL-450DUC2 purchased from Lesker.

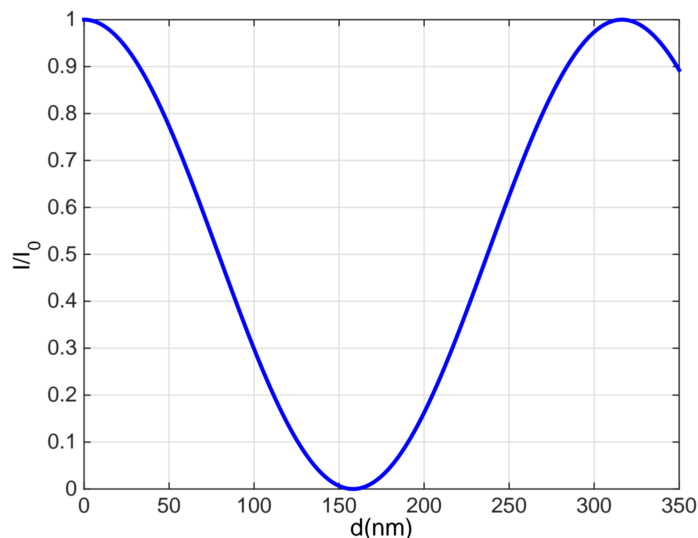

Figure 5.10: Interference pattern for $\lambda = 632.8nm$.

Experimental Setup

A simple interferometer is used to measure the motion of the cantilever. The simple interferometer is very similar to the design used by Rugar et al. [15]. The optical setup is shown in Figure 5.1. The first component of the detection system is the laser. We used an amplitude stabilized HeNe laser to minimize fluctuations in the beam intensity. Fluctuations in the intensity of the laser are indistinguishable from fluctuations caused by a change in the path length; consequently, the amplitude stabilization reduces the noise. The laser is mounted with a cylindrical laser mount on two rack and pinion posts, to enable precise adjustments in the height, pitch, and yaw of the laser.

Following the laser is an optical isolator, which prevents any light reflected from components further along the beam path from entering the laser; the reflected light could destabilize the laser. The next component is a half wave plate (HWP) in a rotation mount; the half wave plate is used to rotate the polarization of the beam such that the maximum amount of light travels to the device. Following the half wave plate is a neutral density filter, used to attenuate the beam power. The beam

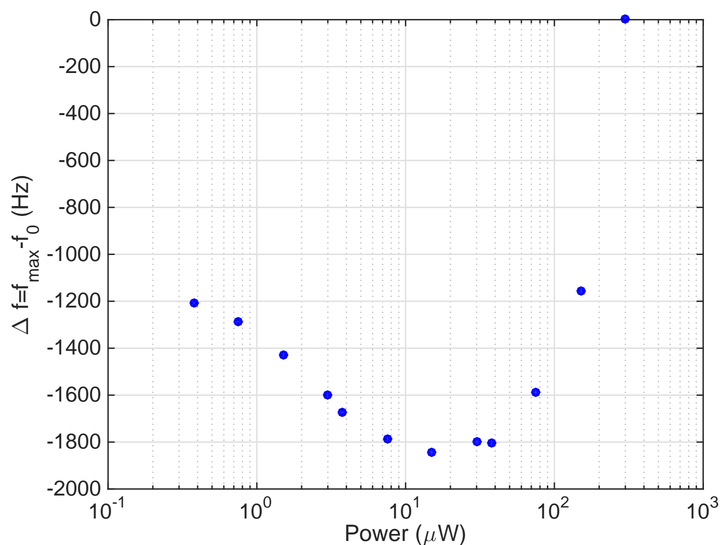

Figure 5.11: Detection beam power vs Δf.

power is attenuated to ensure that heating from the HeNe laser does not lead to a drift in the resonant frequency of the device. For the experiments in Chapter 6, we use a neutral density filter with an optical density of 3.0, which corresponds to 3 μW at the device. We chose this power level by determining the frequency shift due to heating from the HeNe beam. We measured the thermomechanical noise of the device at various intensity levels and determined the corresponding shift in resonant frequency, as shown in Figure 5.11. We measured the thermomechanical noise to avoid measuring the heating from the 690nm actuation laser.

A 20x beam expander follows, mounted in an ultra stable kinematic mount to enable easy alignment of the beam. The next component is the cube polarizing beam splitter (PBS). The PBS splits the beam into its two orthogonal polarization components. The PBS is mounted on a prism mount with pitch, yaw, and roll control for beam alignment. The PBS also prevent ghost reflections, which would occur with a plate beam splitter. Following the PBS is a mirror to direct the beam to the dichroic mirror. The dichroic mirror combines the actuation beam at 690nm and the detection beam at 633nm. The dichroic mirror is chosen such that 99% of the

light at 633nm is reflected, while $>$ 85% of the light at the actuation wavelength, 690nm, is transmitted. Following the dichroic mirror is a quarter wave plate in a rotation mount; the quarter wave plate (QWP) is required to rotate the polarization of the beam by 90° so that the beam reflected from the sample is directed to the photodetector, instead of back towards the laser. After the QWP, the light is focused through an achromatic doublet lens, with $f = 150$ mm, mounted in a kinematic mirror mount on an XYZ stage. We have chosen an achromatic lens to reduce aberrations in the beam. The lens is also chosen to ensure the highest numerical aperture possible. The XYZ stage is a Thorlabs PT3-Z8 motorized stage, with 1" of travel in each direction. Each motor is controlled by a Thorlabs TDC001 T-Cube servo driver; the three drivers are controlled by Labview.

The beam then enters the vacuum chamber through a quartz window with an anti-reflective coating. The beam hits the device and is reflected back along the optical path until it reaches the PBS, where it is directed to the photodetector. Prior to entering the photodetector, the beam traverses a lens with a focal length of 100 mm, to reduce the beam size, since the diameter of the active area of the photodetector is 1 mm. We place a filter between the lens and the photodetector to remove the portion of the 690nm transmitted by the dichroic mirror. The filter[3] has an optical density of 6 for wavelengths between 642.3nm and 696.1nm; it will attenuate the beam at 690nm by a factor of 1 million. The transmission at 633nm is $\geq$ 90%.

The photodetector, a Thorlabs APD130A2, is a temperature compensated, UV enhanced, silicon avalanche photodetector. We utilize a different photodetector for the experiments in Chapter 6 than in Chapter 2 due to the lower optical power used for the experiments. This photodetector has a higher responsivity, 24 A/W at 633 nm, and a higher transimpedance gain, 50 kV/A, than the New Focus 1801. The total gain is 1.2×10^6 V/W. The saturation power is lower at 1.5 μW. The output

[3]The filter is Edmund Optics part number NT68-943.

bandwidth of the photodetector is DC-50MHz. The minimum noise equivalent power is ≈ 0.2 pW/$\sqrt{\text{Hz}}$.

Characterization

The optical detection setup is characterized by three parameters: the spot size of the beam at the device, the responsivity of the system, and the noise floor of the system. We previously discussed the spot size in Section 5.2. The measured spot size is (9.7 ± 0.1) μm.

The responsivity of the system, $\mathcal{R}$, is ratio of the signal measured in Volts at the photodetector to the amplitude of the motion of the device in nm.

$$\mathcal{R} = \frac{S_V^{th}(\omega_0)}{S_x^{th}(\omega_0)}, \tag{5.16}$$

where $S_V^{th}(\omega_0)$ is the measured thermomechanical voltage noise spectral density and $S_x^{th}(\omega_0)$ is the corresponding thermomechanical displacement noise spectral density. We measure the thermomechanical noise spectrum of the device using a Keysight PXA 9030A in spectrum analyzer mode, as shown in Figure 5.12.

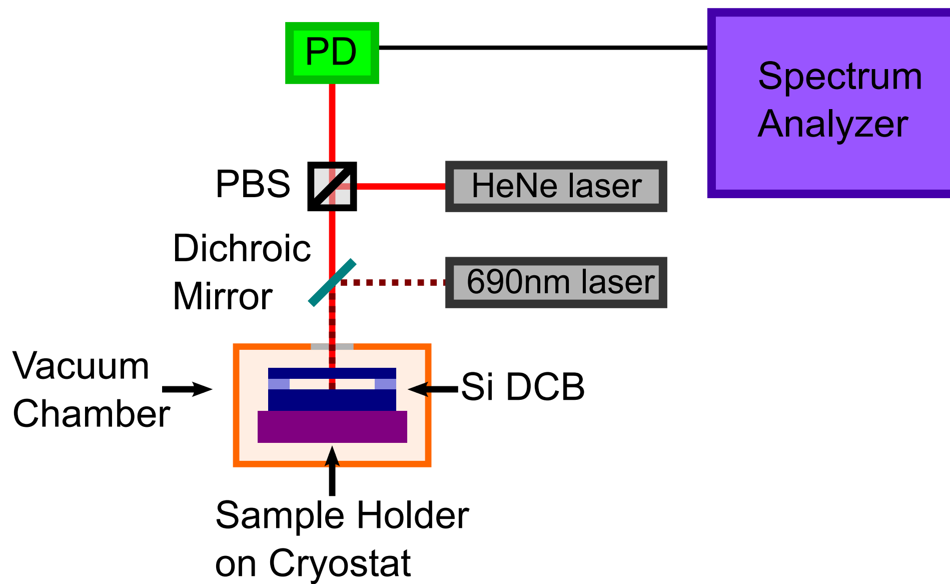

Figure 5.12: Setup for measuring thermomechanical noise. The 690 nm actuation laser was left on during the measurement, but the amplitude was not modulated.

A thermomechanical voltage noise spectral density for Device #3 at T=297 K is shown in Figure 5.13; we fabricated the devices in arrays of 4 device. We number the devices from left to right. Also shown in the figure is the nonlinear least squares fit to a Lorentzian, used to determine $S_V^{th}(\omega_0)$.

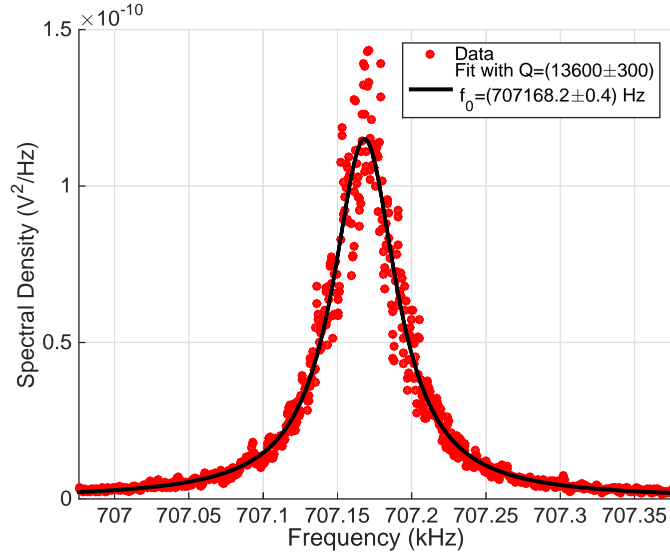

Figure 5.13: Thermomechanical noise spectrum of device #3 at 297K. $S_V^{th}(\omega_0) = (1.15 \pm 0.01) \times 10^{-10} \mathrm{V}^2/\mathrm{Hz}$.

The thermomechanical displacement noise spectral density for a device is given by Equation 5.17 [17]:

$$S_x^{th}(\omega) = \frac{\omega_0}{(\omega_0^2 - \omega^2)^2 + (\omega_0 \omega / Q)^2} \frac{4 k_B T}{M_{eff} Q}, \tag{5.17}$$

where ω_0 is the resonant frequency of the device, Q is the quality factor, k_B is Boltzmann constant, T is the temperature, and M_{eff} is the effective mass of the device. For a doubly clamped beam, $M_{eff} = 0.39 Ltw\rho$ [76], where ρ is the device density. For device dimensions of [L,w,t]= 56 μm, 5 μm, 285 nm, $S_x^{th}(\omega_0) = (35.0 \pm 0.9)$ pm^2/Hz. The corresponding responsivity is $\mathcal{R} = (1.81 \pm 0.01)$ mV/nm.

The thermal noise measurement is limited by the shot noise of the photodetector. In Figure 5.14, we show a fit of the thermomechanical noise on a larger bandwidth,

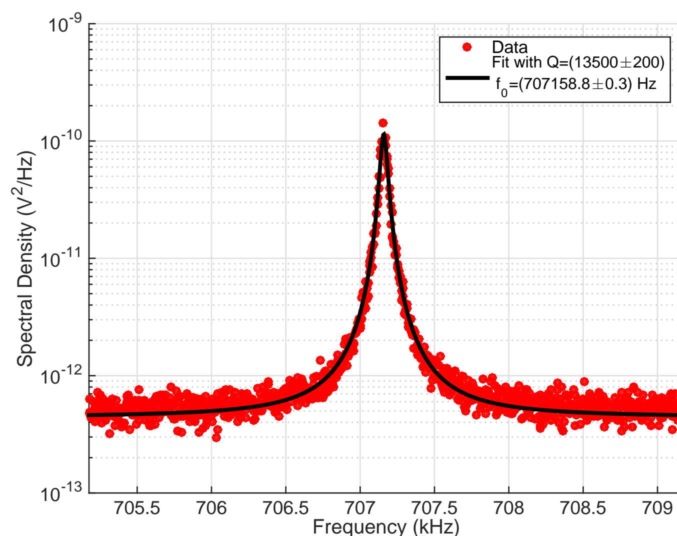

Figure 5.14: Thermomechanical noise spectrum of device #3 at 297K, with a measurement bandwidth of 4 kHz. The amplitude is plotted using a logarithmic scale. The background noise is $(4.4 \pm 0.9) \times 10^{-13}$ V^2/Hz.

$\Delta f = 4$ kHz. For the responsivity previously calculated, the displacement noise floor is 0.4 pm.

5.4 Actuation System

For the phase noise measurements, the devices are driven by modulating the intensity of a 690nm 30mW diode laser.[4] The choice of wavelength is driven by the specifications of the dichroic mirror used to combine the detection and actuation beams before the focusing lens. We wished to maximize reflection at 632.8nm. The laser diode is placed in a mount with temperature control and frequency modulation. The temperature control is required because the laser power, wavelength, and threshold current depend upon the diode temperature; we operate the laser diode at 25°C. The laser diode mount and control unit together provide DC-100MHz modulation of the laser diode.

[4]The laser consists of a HL6738MG laser diode mounted in a Thorlabs temperature controlled laser diode mount (TCLDM9).

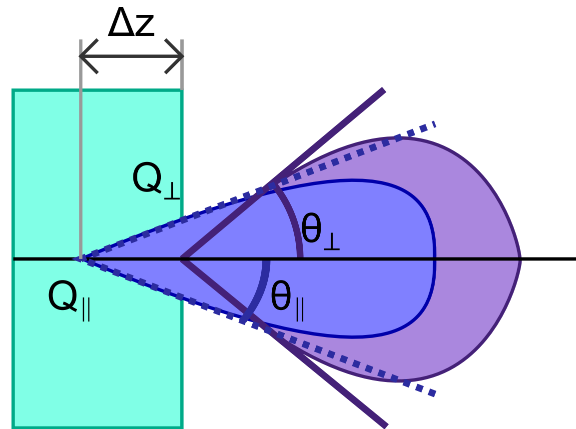

Figure 5.15: Angular emission of a semiconductor laser. $\theta_\perp$ is the full width at half maximum (FWHM) beam divergence angle perpendicular to the junction. $\theta_\|$ is the FWHM beam divergence angle parallel to the junction. Δz is the difference between the parallel source point, $Q_\|$, and the perpendicular source point, $Q_\perp$.

As shown in Figure 5.15, the light emitted by the laser has a large divergence angle perpendicular to the laser junction, $\theta_\perp$, and a small divergence angle parallel to the laser junction, $\theta_\|$ [74]. The resulting beam is elliptical. Gain guided semiconductor lasers also have intrinsic astigmatism. The parallel and perpendicular components of the beam have different source points; for the semiconductor laser used, HL6738MG, Δz, the distance between source points, is 4-6μm depending upon the output power.[5]

The collimation optics for the semiconductor laser consist of two parts: an aspheric singlet to collimate the divergent beam and an anamorphic prism pair to circularize the elliptical beam [75]. The desired beam shape and size is a circular beam with a diameter of 14mm; the beam size is set by the beam steering mirror used to adjust the position of the actuation spot relative to the detection spot. The mirror in the beam steering mirror has a clear aperture of 25.4 mm. The beam steering mirror is at a 45° angle, as shown in Figure 5.1, which reduced the clear aperture in the x-direction to 18.0 mm. As discussed previously, the laser diode produces an elliptical beam. The maximum beam divergence perpendicular to the junction is 23°, with the typical

[5]The data sheet for HL6738MG is available from http://www.thorlabs.us.

beam divergence being 19°. The width of the laser beam d after the collimating lens is set by the focal length f of the collimating lens, with $d = f \tan(\theta_{\perp})$. A lens with a focal length $f = 3.30$ mm[6] produces an elliptical beam with a major axis of 1.40mm. Using the value for the maximum beam divergence parallel to the junction, $\theta_{\|} = 8.5°$, the width of the minor axis of the elliptical beam is 0.49mm. We use an aspheric singlet to collimate the laser beam because it does not add any spherical aberration to the beam. Following the diode laser is an anamorphic prism pair[7] that transforms the elliptical beam into an approximately circular shape by magnifying the minor axis by a factor of 3. Next is a 10x beam expander in a kinematic mount to ensure easy alignment of the beam; the spot size at the device is 14μm. The next element is the beam steering mirror, which controls the position of the actuation beam relative to the detection beam on the sample. We use a piezo actuated mirror mount for fine angular control of the beam position. To move the beam in 1μm increments, over a range of 260μm, requires an angular resolution of 8 microradians with a range of 17 milliradians. This angular resolution and range limited the choice of mirror mount to a Newport Motorized Stability Mount. Following the piezo actuator mirror is the dichroic mirror, which combines the two beams. The beam then enters the achromatic lens and then the chamber.

The amplitude of the actuation laser is modulated by adding an RF component to the DC current.

$$I_D(t) = I_{DC} + I_{MOD} \sin(\omega t) \tag{5.18}$$

For the measurements in Chapter 6, we use I_{DC}=48 mA, which corresponds to a laser power of 0.90 mW. The RF component the laser beam leads to localized heating of the beam, which leads to thermal expansion and thermoelastic actuation of the beam [77, 78].

[6] Thorlabs A414TM-B
[7] Thorlabs PS879-B

5.5 Annealing System

The annealing system is comprised of a diode laser and the optics used to align and focus the beam onto the device. The annealing laser is a 640nm Coherent Cube laser, with a power of 100mW. A heat sink is required for the laser to ensure that it does not overheat. Following the laser is an optical isolator to prevent any light reflected from optics further along the beam line from entering the laser. The next component is a half wave plate to precisely adjust the polarization angle and a quarter wave plate to remove any circular polarization. A polarizing beam splitting cube is the next element; it ensures that the beam is p-polarized, which corresponds to light polarized parallel to the plane of reflection. The polarization of the beam is critical to maximize the power transferred to the devices; the laser beam impinges upon the device at Brewster's angle for silicon, 75°. All light that is polarized parallel to the plane of incidence will be transmitted to the device.

Following the polarization plates is a 2-5x beam expander, and then an achromatic lens with a focal length, $f = 200$mm. The lens is mounted on a motorized XYZ stage. For a magnification of 2x and a focal length of 200mm, the minimum spot size is $78\mu m$. For a magnification of 5x and a focal length of 200mm, the minimum spot size is $31\mu m$.

5.6 Vacuum System

The vacuum system contain two sections: a load lock and a main chamber. A photo of the system is shown in Figure 5.16.

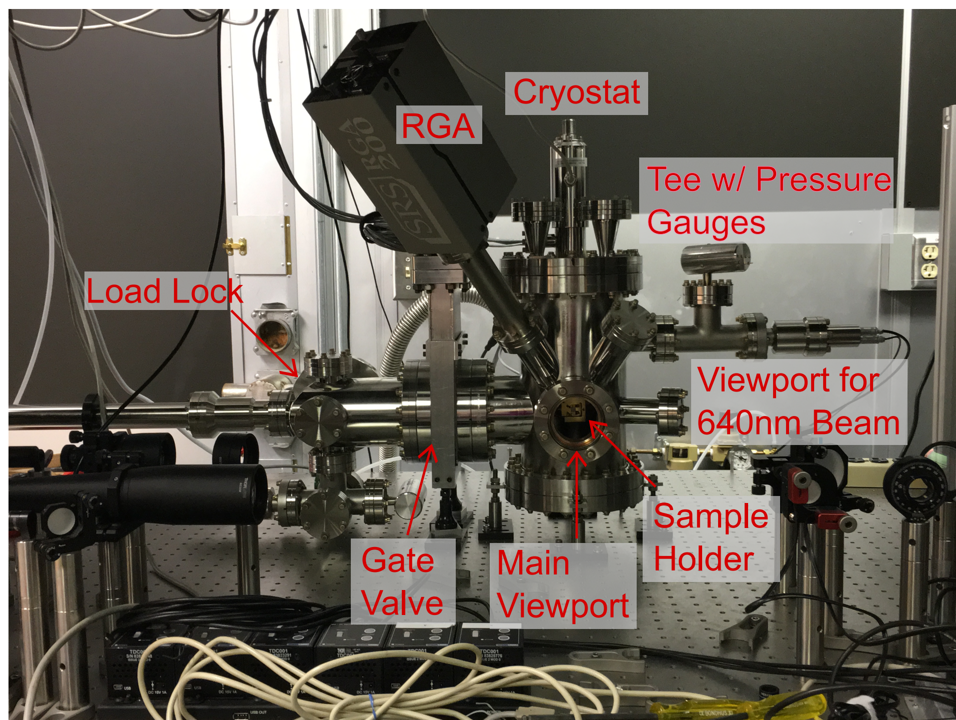

Figure 5.16: Photograph of vacuum setup. The turbomolecular pump is mounted on the back flange of the chamber and is not visible in the photograph.

The main chamber is a custom vacuum chamber fabricated by MDC Vacuum Products. It has an Stanford Research Systems 200 residual gas analyzer (RGA) on the front of the chamber. There are two pressure gauges on the tee on the right side of the chamber: a MKS 422 cathode gauge and a MKS 317 convection Pirani gauge. There is a view port on the front, where the detection beam (633nm HeNe) and the actuation beam (690nm diode laser) enter the system. There is a second optical port that makes a 75° angle with the sample holder, through which the annealing beam enters the chamber. On the back flange of the chamber is a HiPace 80 turbomolecular pump. The turbomolecular pump is backed by an Agilent SH-110 scroll pump. On the left side of the chamber is a gate valve that connects to the load lock. A gas inlet for nitrogen gas is connected to the bottom of the load lock for venting of the chamber.

The initial base pressure of the chamber with the gate valve closed was 2.5×10^{-8}

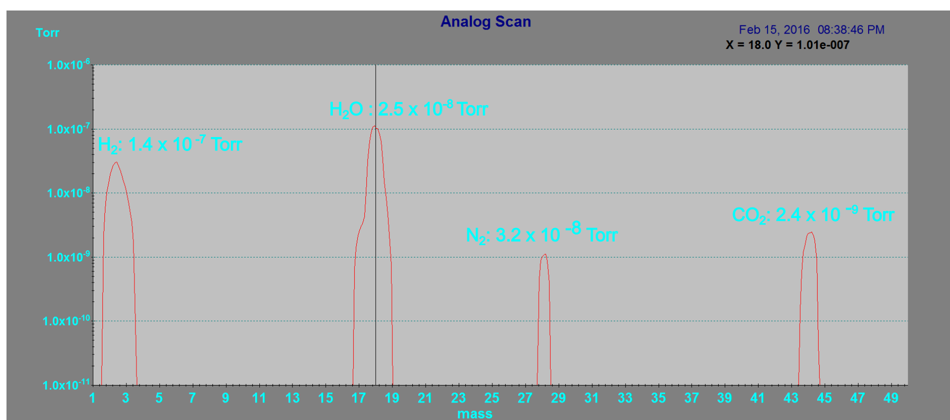

Figure 5.17: RGA spectrum taken before bake out. The partial pressure and species is listed for each peak.

Torr at room temperature. After a low temperature bake out for 36 hours, the chamber reached a base pressure of 2.5×10^{-9} Torr at room temperature. The RGA spectrum taken before the bake out is shown in Figure 5.17; the spectrum after the bake out was below the sensitivity of the RGA.

5.7 Cryostat and Sample Holder

The cryostat is an Advanced Research Systems LT3-B helium flow cryostat. This cryostat was chosen to limit vibrations from the helium flow at the sample. A photograph of the sample holder mounted on the cryostat is shown in Figure 5.18. Both the fixed sample holder (FSH) and mobile sample holder (MSH) are machined from oxygen free copper and electroplated with gold. The mobile sample holder is attached to the fixed sample holder via a stainless steel screw. The sample is attached to the mobile sample holder via beryllium copper springs.

5.8 Sample Fabrication

We used a top down fabrication process to fabricate the devices used in these experiments. An illustration of the process flow is shown in Figure 5.19. We began the sample fabrication with an 8" silicon on oxide wafer from SOITEC. The silicon device layer was 300 nm thick. The buried oxide layer was 400 nm thick. We then

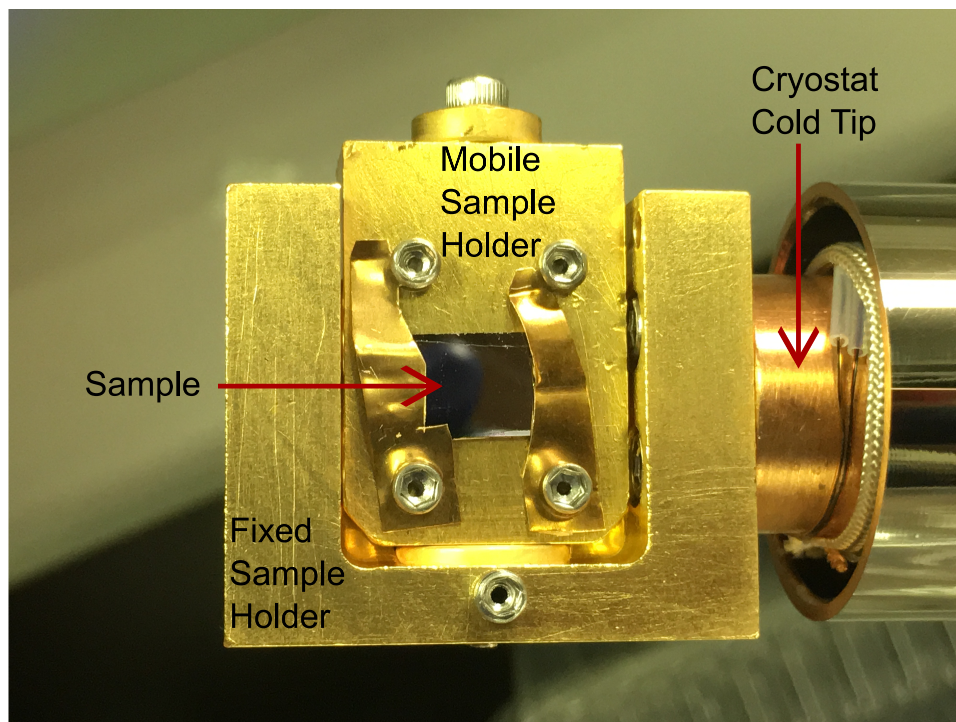

Figure 5.18: Photograph of sample holder mounted on cryostat.

had the wafers oxidized by Rogue Valley Microdevices to thin the silicon device layer to 285 nm. We chose a device layer thickness of 285 nm to maximize reflectivity at 632.8 nm. 285 nm is equal to $\frac{7}{4}\frac{\lambda}{n_{Si}}$, which leads to constructive interference and higher reflectivity [79, 80]. Rogue Valley Microdevices then deposited 100nm of low stress silicon nitride (SiN) on top of the oxide grown on both sides of the wafer via low pressure chemical vapor deposition. The original process flow involved membrane based devices; the silicon nitride was deposited as an etch mask for the potassium hydroxide etch used to fabricate the membranes. We then stripped the SiN layer using a reactive ion etch. We used buffered hydrofluoric acid (BHF) to remove the silicon oxide (SiO_2) layer before spinning ZEP 520A onto the wafers; ZEP 520A is a positive electron beam resist. We then used electron beam lithography to define the devices. We developed the resist with ZED 50. We used reactive ion etching to define the silicon devices. We then used a 49% hydrofluoric acid solution to release the devices; we used a 49% hydrofluoric acid solution instead of buffer

hydrofluoric acid (BHF) due to the non-negligible etching of the device layer by BHF due to the long etch times (30-40 minutes) for BHF. We then used critical point drying to prevent the devices from collapsing. We fabricated the beams in groups of four devices. We used scanning electron microscopy (SEM) to determine the beam dimensions. The two devices measured in Chapter 6 are shown in Figure 5.20; we also include an image of the four devices.

5.9 Summary

In this chapter, we describe the experimental setup used to measure the temperature dependence of anomalous phase noise in Chapter 6. We describe the fabrication process for the silicon doubly clamped beams used in the experiment. We also describe the optical system used to actuate, detect, and anneal the devices, as well as the vacuum system and cryostat used in the measurements.

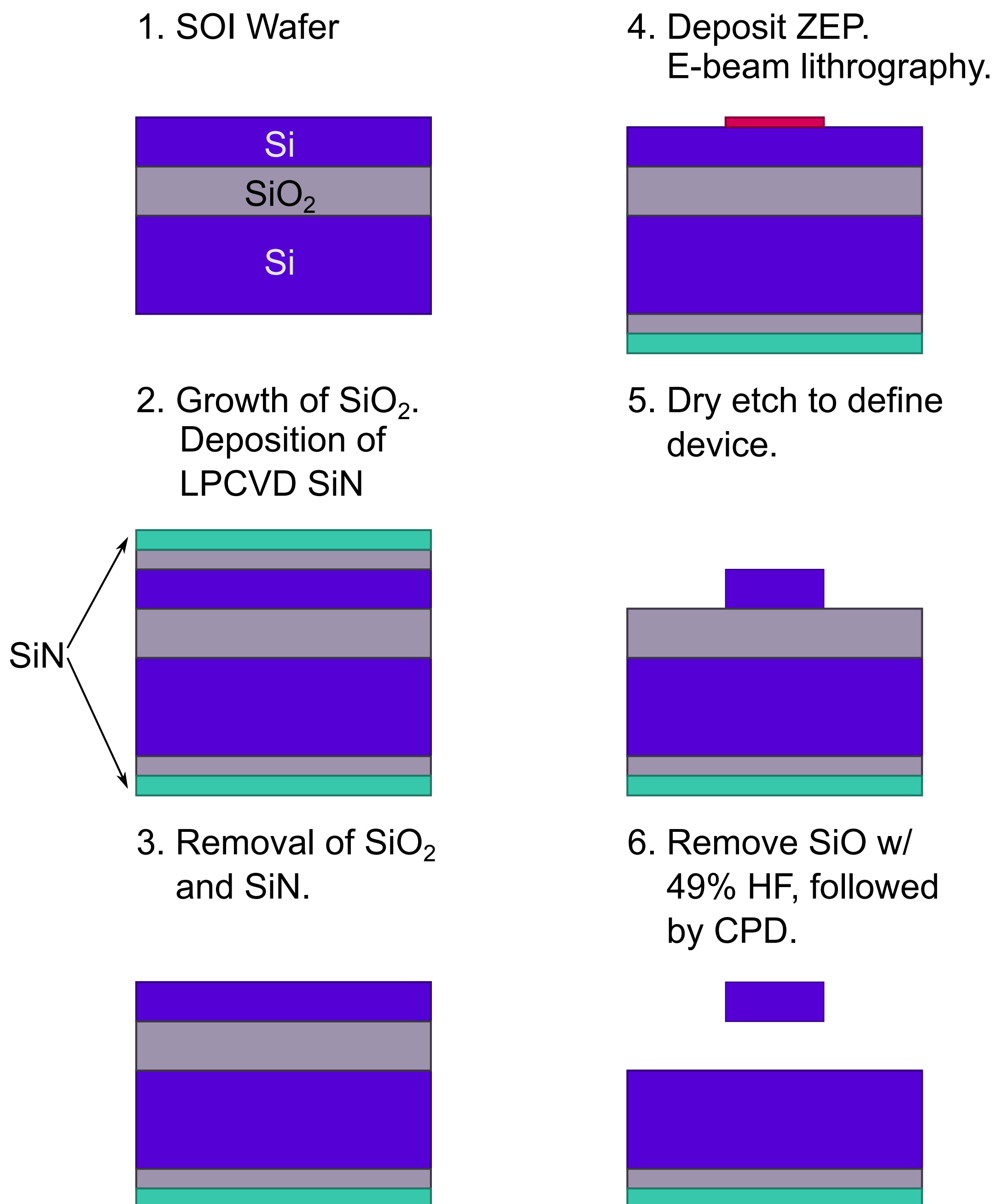

Figure 5.19: Process flow for fabrication of silicon doubly clamped beams for phase noise measurements.

This is a SEM image
of a silcon doubly
clamped beam.

Figure 5.20: Colorized image of a Si doubly clamped beam. **The beam dimensions are [insert numbers after imaging].**

Chapter 6

CHARACTERIZATION OF ANOMALOUS PHASE NOISE

In this chapter, we discuss the measurements made to quantify the temperature dependence of phase noise. We begin with a discussion of the process used to determine the temperature of the device. We then describe the oscillator setup used to make the measurement. We next discuss the data from the measurements and perform an analysis of the temperature dependence of anomalous phase noise.

6.1 Temperature Calibration

Using the setup described in Chapter 5, we measure the phase noise of two silicon doubly clamped beams over a range of temperatures. Before making the phase noise measurement, we first determine the temperature of the sample. The thermometer on the cryostat is not directly mounted on the sample holder; it provides an inaccurate estimate of the temperature of the sample at temperatures below room temperature. To obtain a more accurate value, we measure thermomechanical noise, which is proportional to the absolute temperature of the device. However, to employ this method, several calibrations are required. We measure the backbone curve in order to determine the 1 dB compression point in V_{RMS}. We use this information along with the calculated 1 dB compression in nm_{RMS} to determine the responsivity. We then use the measured thermomechanical noise to determine the temperature. We verify the calculation by determining the sample temperature at room temperature, where the sample is in thermal equilibrium with the sample holder. We begin by measuring the backbone curve for Device #3. A diagram of the measurement setup is shown in Figure 6.1. We use optical detection and optical actuation, along with an Agilent 4395a Network/Spectrum/Impedance analyzer in network analyzer

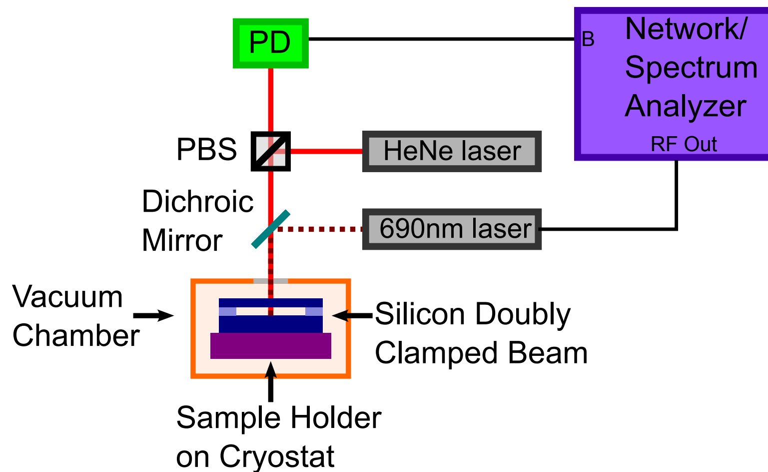

Figure 6.1: Measurement setup for temperature calibration. We use the network analyzer to measure the backbone curve and the spectrum analyzer to measure the thermomechanical noise.

mode to measure the backbone curve. An example backbone curve for device #3 at T=297K is shown in Figure 6.2. We observe a softening Duffing instability instead of the expected stiffening instability for both beams. We observed a small amount of buckling in SEM images of devices with similar dimensions fabricated using the same fabrication procedure, which would lead to the softening observed. From the backbone curve, we determine that the 1dB compression point occurs at V_{RMS}=6.78 mV_{RMS}. The 1dB compression point corresponds to the amplitude at which the signal is 1dB smaller than expected for a linear transfer function. The 1dB compression is defined as $x_c = 0.745 a_c$ [44], where a_c is the critical amplitude, which corresponds to the onset of non-linearity [6].

$$\langle x_c \rangle \approx t \left[\frac{2}{0.528 Q (1 - \nu_{xz})^2} \right]^{1/2}, \tag{6.1}$$

where ν_{xz} is Poisson's ratio and t is the thickness of the device. Using Equation 6.1 and Q=14000, we find that x_C =3.75 nm_{RMS}. The corresponding responsivity is (1810 ± 90) μV/nm. We next measure the thermomechanical noise using a Keysight PXA 9030A in spectrum analyzer mode, as described previously in Section 5.3. The thermomechanical noise spectrum is shown in Figure 6.3. In order to find the

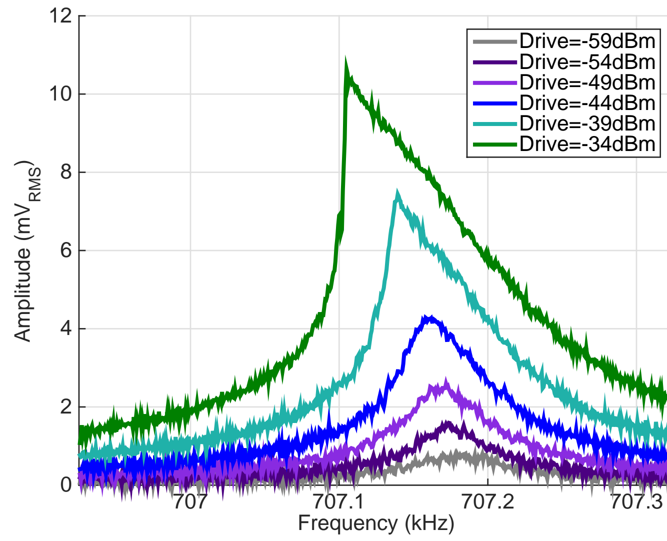

Figure 6.2: Backbone curve for Device #3 at 297K. We used ND=3.0 on the HeNe laser and ND=2.6 with I_D=48 mA on the 690 nm laser.

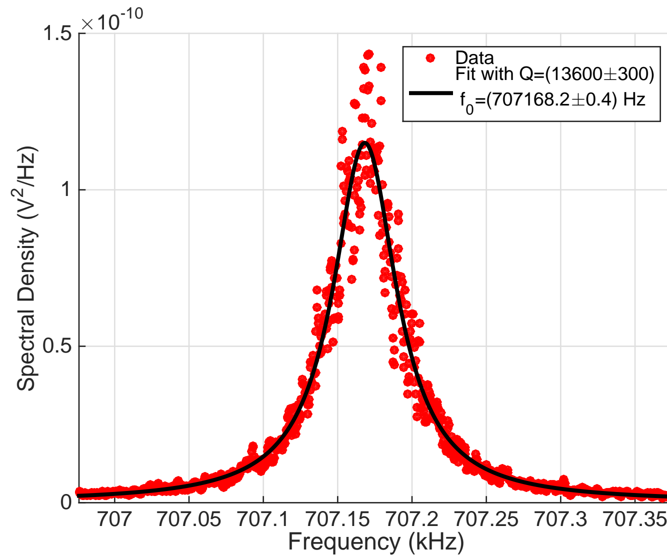

Figure 6.3: Thermomechanical noise spectrum of device #2 at 297K. $S_V^{th}(\omega_0) = (1.15 \pm 0.01) \times 10^{-10}\mathrm{V}^2/\mathrm{Hz}$.

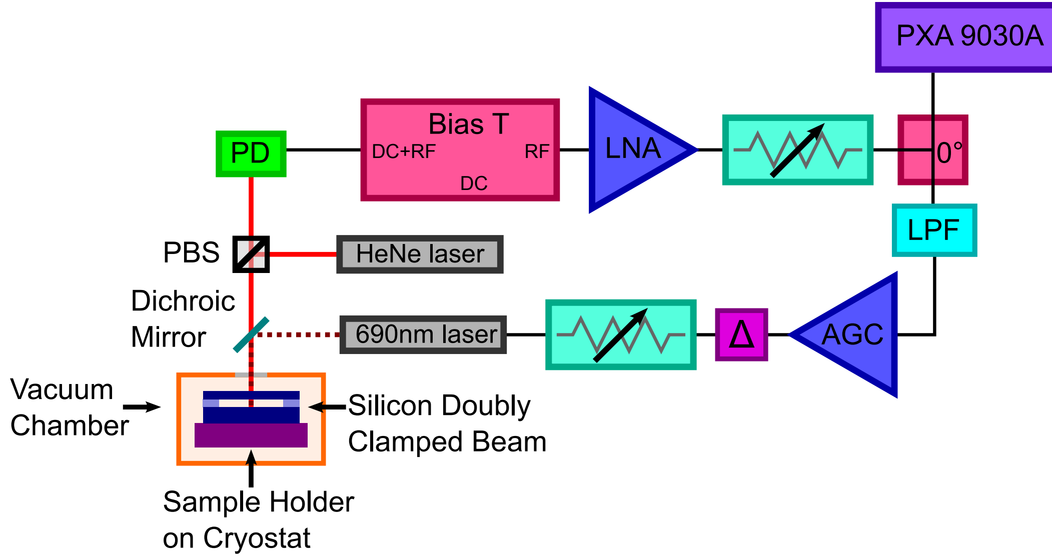

Figure 6.4: Diagram of oscillator setup. The signal from the DCB is measured with the photodetector. The RF portion of the signal is amplified, attenuated, and split between the PXA 9030A and the AGC; there is a low pass filter before the AGC. After the AGC is a phase shifter followed by variable attenuation before the signal is fed to the 690nm laser diode, in order to modulate the intensity.

temperature, we invert the equation for responsivity.

$$T = \frac{S_v^{th}}{\mathscr{R}^2}\frac{M_{eff}\omega_0^3}{4k_BQ} \tag{6.2}$$

Using the measured responsivity and the measured values of S_V^{th}, M_{eff}, Ω_0, and Q, we find $T = (298 \pm 19)$ K, which agrees with the temperature measured by the temperature controller of 297 K.

6.2 Oscillator Setup

We used the silicon doubly clamped beams described in Chapter 5 as the resonator in the oscillator. A diagram of the oscillator setup is shown in Figure 6.4. The signal from the silicon doubly clamped beam is detected with the photodetector, as described in Chapter 5. Following the photodetector is a Mini-Circuits ZFBT-4R2GW+ bias-tee, which splits the signal into a DC component and an RF component composed of frequencies greater than 100kHz. We measure the DC component with a multimeter. The signal level allows us to monitor the optical

alignment during measurements; shifts in the measured voltage correspond to a shift in alignment and a lower responsivity. After the bias-tee is a Mini-Circuits ZFL-1000LN+ low noise amplifier, with a gain of 23.4 dB around 715 kHz, the resonant frequency of the device. Following the amplifier is a variable attenuator to prevent overload of the PXA 9030A and the automatic gain control circuit. After the variable attenuator is a Mini-Circuits ZFSC-2-4-S+ 0° power splitter. On one side of the splitter is a Keysight PXA 9030A signal analyzer with a phase noise measurement application. On the other side of the splitter is a Mini-Circuits BLP-1.9 low pass filter, which has a 3 dB bandwidth of 1.9 MHz. After the low pass filter is the AGC circuit, which employs an Analog Devices AD8368 on its associated evaluation board. For an input range of -30 dBm to -10 dBm, the AGC provides a constant output of -10 dBm. The response time of the AGC to a change in the input signal level is on the order of hundreds of microseconds. The response time of the measurement is limited by the response time of the AGC. After the AGC is a Mini-Circuits JCPHS-2.5+ variable voltage phase shifter. After the phase shifter is a variable attenuator to ensure the proper drive level is used to modulate the 690nm actuation beam.

6.3 Temperature Dependence of Anomalous Phase Noise

We measured the temperature dependence of anomalous phase noise over a range of temperatures for two devices. Before discussing the data from these measurements, we consider the temperature dependence of relevant properties of the device, such as quality factor, resonant frequency, and actuation efficiency. For all of the measurements, the detection laser was attenuated by a neutral density filter of ND=3.0. For all of the measurements, the actuation laser was driven with a DC current I_D=48 mA. For the measurement on Device #2 at 297 K, the actuation beam was attenuated with a neutral density filter of ND=4.0. For the rest of the measurements, a neutral

density filter of ND=2.6 was used. We compare the measured resonant frequency and quality factors of the two devices in Tables 6.1 and 6.2. As expected, both

Device #2		
Temperature (K)	Q	f_0 (Hz)
21 ± 2	39100 ± 400	730704.2 ± 0.2
52 ± 5	20500 ± 300	728836.6 ± 0.2
297	16500 ± 300	710667.0 ± 0.3

Table 6.1: Temperature Dependent Properties of Device #2

Device #3		
Temperature (K)	Q	f_0 (Hz)
25 ± 2	38000 ± 600	729963.5 ± 0.1
45 ± 4	25000 ± 500	725153.2 ± 0.2
297	14000 ± 200	707158.2 ± 0.4

Table 6.2: Temperature Dependent Properties of Device #3

the quality factor and the resonant frequency increased as temperature decreased. To assess drive efficiencies for the devices at different temperatures, we compare the depth of modulation required to reach an amplitude of 1.0 nm for Device #2 and an amplitude of 1.4 nm for Device #3; 1.4 nm is less than half of the 1 dB compression point for all temperatures. An amplitude of 1.4 nm corresponds to a $\sim$ 3 dB higher modulation depth. The modulation depth for Device #2 is given in Table 6.3 and the modulation depth for Device #3 is given in Table 6.4. For Device #2, the depth of modulation increased as the temperature decreased, despite the use of a larger neutral density filter at 297 K. For Device #3, a higher modulation depth was required to reach an amplitude of 1.5 nm at 45 K than at 25 K. However, the actuation efficiency is highly dependent upon the alignment of the actuation beam to the device. The measurement at 45 K most likely corresponded to a poorer alignment of the actuation beam.

We measured λ_{11} for both devices at 297 K. We measured resonant frequency, f_0, versus the amplitude of the motion of the device for several drive levels. For

Device #2		
Temperature (K)	Amplitude (nm)	Drive (dBm)
21 ± 2	1.0	-23
52 ± 5	1.0	-29
297	1.0	-34

Table 6.3: Comparison of Actuation Efficiency vs Temperature for Device #2

Device #3		
Temperature (K)	Amplitude (nm)	Drive (dB)
25 ± 2	1.4	-28
45 ± 4	1.5	-24
297	1.4	-49

Table 6.4: Comparison of Actuation Efficiency vs Temperature for Device #3

measurements where the device was in the nonlinear operating regime, we used the frequency at the highest amplitude as the resonant frequency. At each drive level, we measured the resonant frequency at a low drive amplitude and then measured the resonant frequency at the desired drive amplitude in order to account for drifts in the resonant frequency. We used the responsivity calculated from the thermomechanical noise peak to determine the device amplitude in nm. We used a linear fit to determine λ_{11} for both devices. The data and fits are shown in Figures 6.5-6.6.

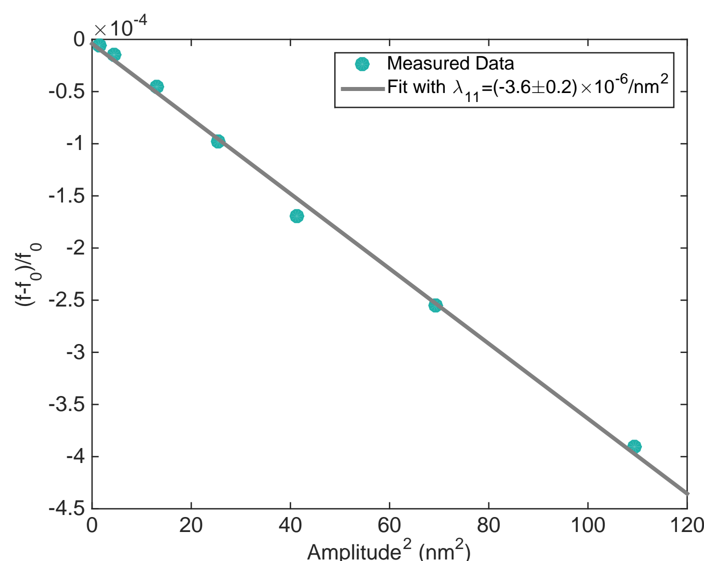

Figure 6.5: Fit of amplitude squared versus fractional frequency shift for Device # 2

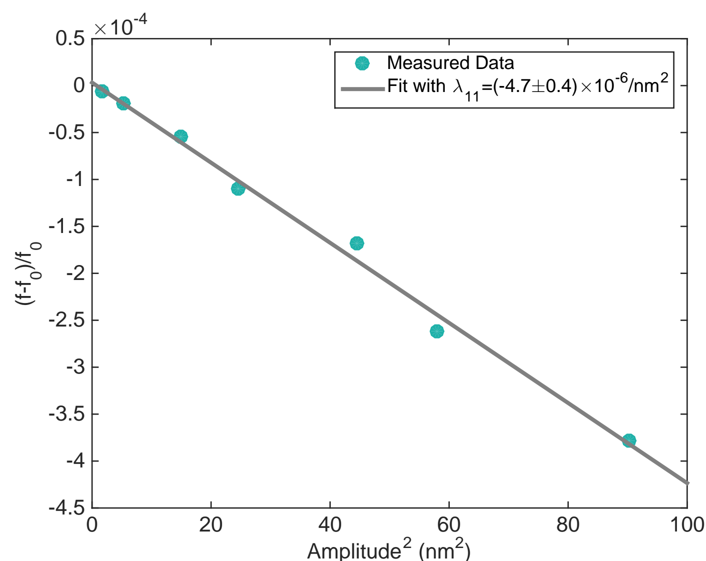

Figure 6.6: Fit of amplitude squared versus fractional frequency shift for Device # 3

Device #3		
Temperature (K)	a	Δ
25 ± 2	0.69 ± 0.04	$\frac{\pi}{2}$
45 ± 4	0.78 ± 0.04	$\frac{\pi}{2}$
297	0.75 ± 0.04	$\frac{\pi}{2}$

Table 6.5: Table of Operation Points for Device #3

We next consider the temperature dependence of anomalous phase noise in Device #3. We provide the operating points for the measurements in Table 6.5. We calculate the amplitude, a, using the value measured for the nonlinear spring coefficient, λ_{11}, at room temperature. Ideally, λ_{11} should be measured at each temperature, because λ_{11} depends upon several temperature dependent quantities: the Young's modulus of silicon, the dimensions of the beam, and the tension in the beam. However, we did not measure λ_{11} while measuring the phase noise, so we use the value from 297 K as an estimate for all temperatures. The operating points are almost within one standard deviation of each other. The temperature dependence of anomalous phase noise for these operating points is shown in Figure 6.7; we have subtracted off the

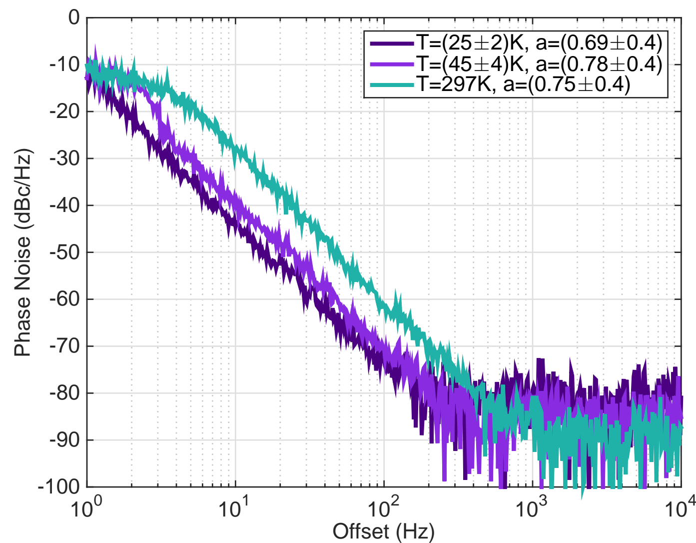

Figure 6.7: Phase Noise of Device #3 vs Temperature

constant background due to shot noise from the photodetector.

During these measurements, we did not alter Δ. The majority of the operating points corresponded to the regime where direct thermomechanical noise is greater than or equal to amplitude to phase conversion thermomechanical noise ($a < 0.82$); in this case, changing Δ would not have changed the total thermomechanical noise. If the operating points had been in the regime where amplitude to phase conversion thermomechanical noise dominated, then increasing Δ to values greater than $\frac{\pi}{2}$ would have decreased the contribution from D_a, lowering the total contribution from thermomechanical noise.

We now compare the phase noise measured at $\approx$ 23 K, $\approx$ 55 K, and 297 K for the two devices. The operating points (a, Δ) for both devices at each temperature are given in Table 6.6. The operating points differed between temperatures; however, the operating points were consistent at each temperature. We show the phase noise of the two devices at $\approx$ 23 K in Figure 6.8, $\approx$ 55 K in Figure 6.9, and 297 K in Figure 6.10. The phase noise measured at similar operating points and similar temperatures is consistent between the two devices, with the exception of large offset

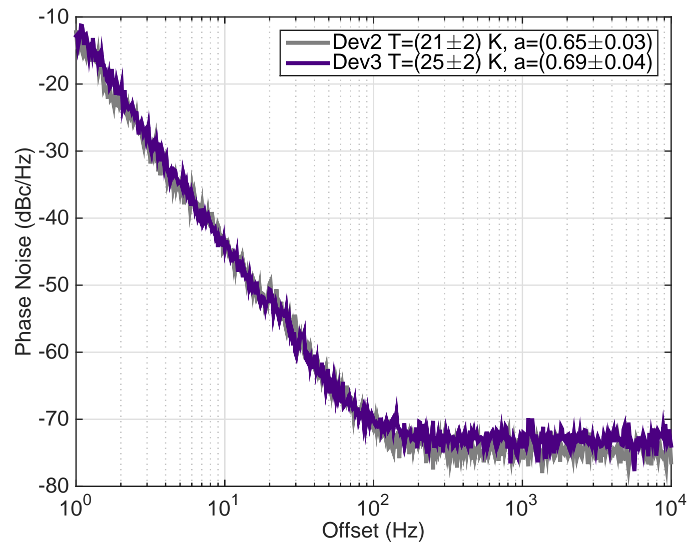

Figure 6.8: Comparison of Phase Noise at 23 K

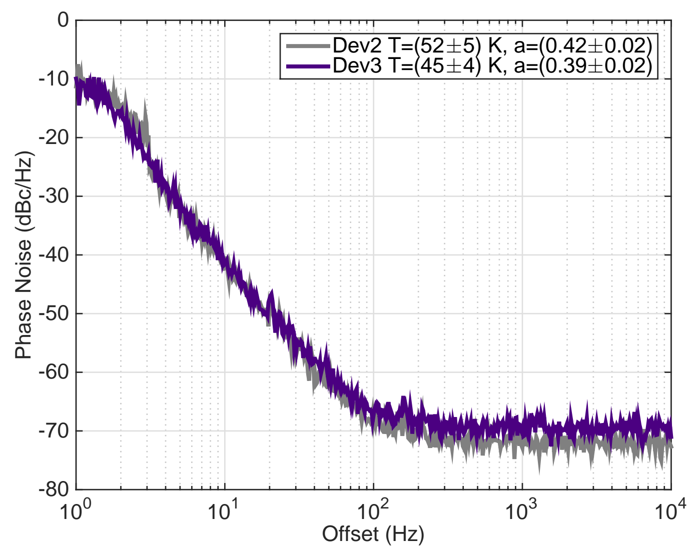

Figure 6.9: Comparison of Phase Noise at 55 K

Device #2		
Temperature (K)	a	Δ
21 ± 2	0.65 ± 0.03	$\frac{\pi}{2}$
52 ± 5	0.42 ± 0.02	$\frac{\pi}{2}$
297	0.85 ± 0.04	$\frac{\pi}{2}$

Device #3		
Temperature (K)	a	Δ
25 ± 2	0.69 ± 0.04	$\frac{\pi}{2}$
45 ± 4	0.39 ± 0.02	$\frac{\pi}{2}$
297	0.75 ± 0.04	$\frac{\pi}{2}$
297	0.99 ± 0.04	$\frac{\pi}{2}$

Table 6.6: Table of Operation Points

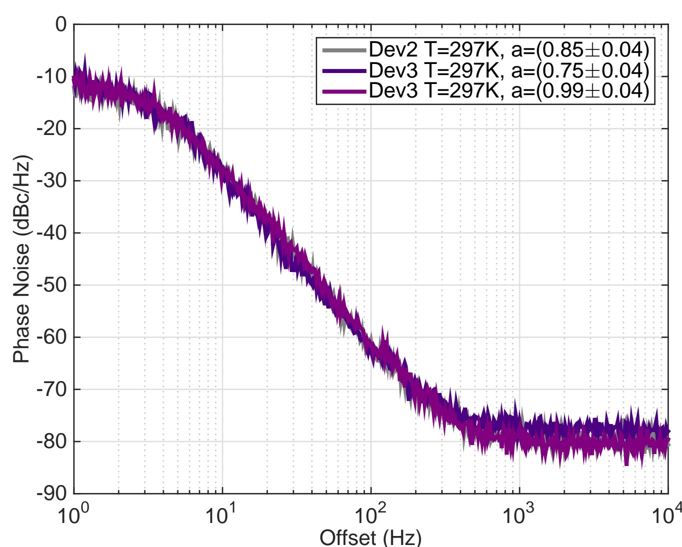

Figure 6.10: Comparison of Phase Noise at 297 K

frequencies, where the noise is dominated by shot noise. At low offset frequencies, the measurement is limited by the upper measurement limit of the PXA, ≈ -10 dBc/Hz, which leads to a roll off in the measured phase noise. For $\approx$ 23 K and $\approx$ 55 K, the operating points are within one standard deviation of each other. For the data taken at 297 K, the amplitude of Device # 2 is between the two measured values for Device #3; the gray trace representing Device # 2 is covered by the traces corresponding to Device #3.

We also plot the phase noise at a 10 Hz offset for each device versus temperature in Figure 6.11 for the operating points listed Table 6.6. We observed a temperature

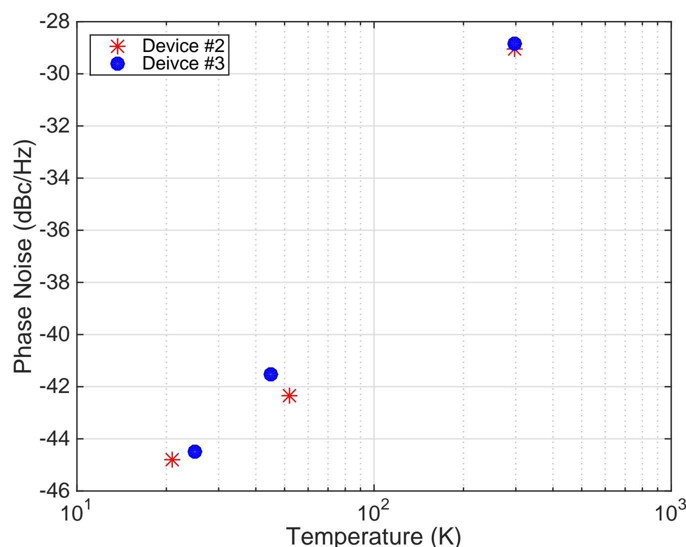

Figure 6.11: Comparison of Phase Noise at 10 Hz Offset vs Temperature

dependence of roughly $T^{1.5}$. Data at more temperatures and consistent operating points would be required to accurately assess the temperature dependence of anomalous phase noise. However, our measurements demonstrate that anomalous phase noise decreases with temperature.

6.4 Frequency Dependence of Anomalous Phase Noise

We next assess the frequency dependence of anomalous phase noise. We fit the three measurements shown in Figure 6.7. We use the offset frequencies where the measurement is not limited by the roll off from PXA at low offset frequencies and by shot noise from the photodetector at high offset frequencies. We employ a linear fit of the logarithm base 10 of the offset frequency and the measured phase noise to determine the frequency dependence of anomalous phase noise. For T=25 K, we fit the phase noise for the following offset frequencies: 1.8 Hz to 100 Hz. For T=45 K, we fit the phase noise for the following offset frequencies: 3.1 Hz to 212 Hz. For T=297 K, we fit the phase noise for the following offset frequencies: 8.1 Hz to 603 Hz. The data and fits are shown in Figures 6.12-6.14. We observed a f^{α} dependence with $\alpha \approx -3$.

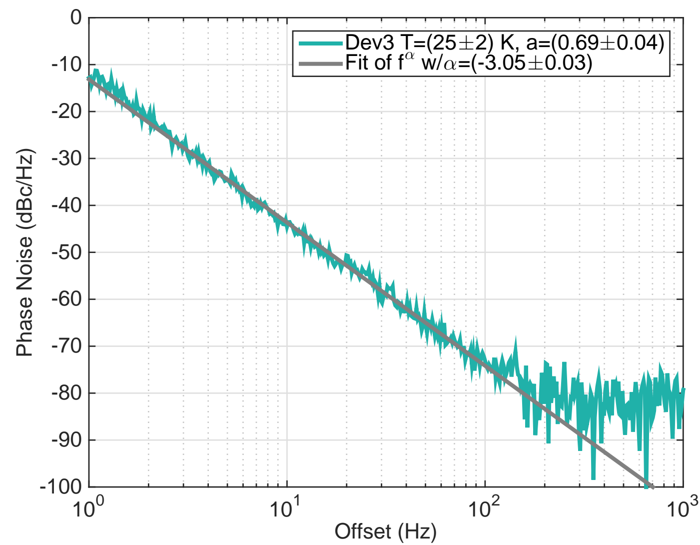

Figure 6.12: Frequency Dependence of Phase Noise at T=25 K

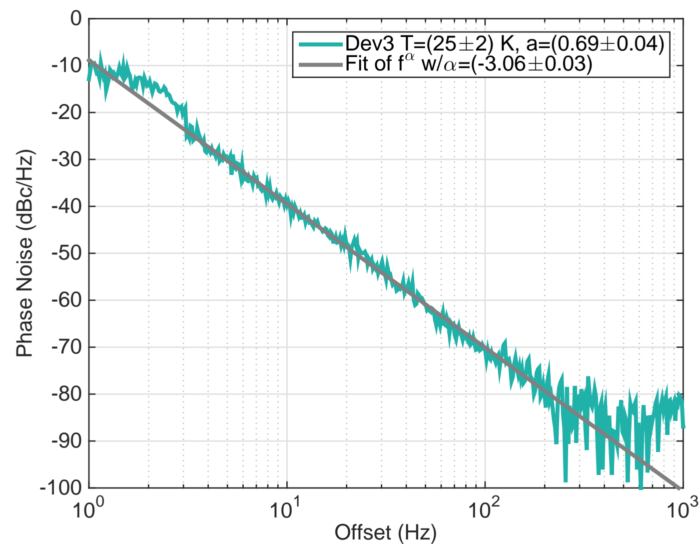

Figure 6.13: Frequency Dependence of Phase Noise at T=45 K

6.5 Mode Dependence of Anomalous Phase Noise

In addition to measuring the temperature dependence of anomalous phase noise, we also measured the phase noise of both the first and second mode of Device #3 at 297 K. The phase noise measurement for the second mode, as well as the data from the first mode ($f_1 = 707$ kHz) referenced to the frequency of the second mode ($f_2 = 1.867$ MHz), is shown in Figure 6.15. The phase noise measured for the

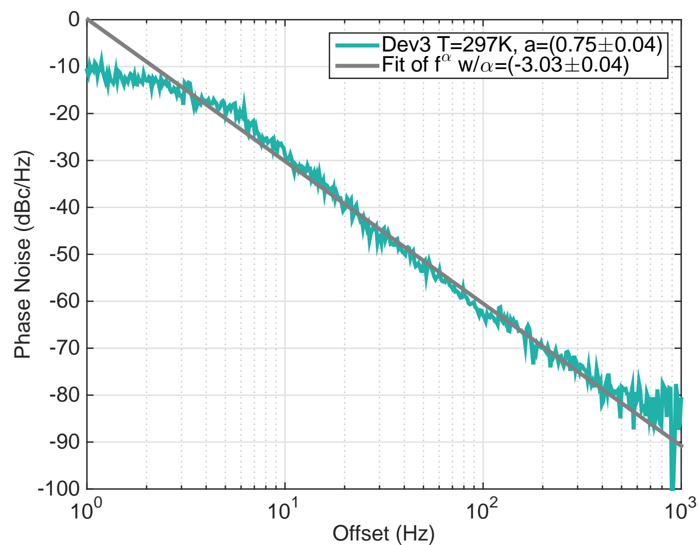

Figure 6.14: Frequency Dependence of Phase Noise at T=297 K

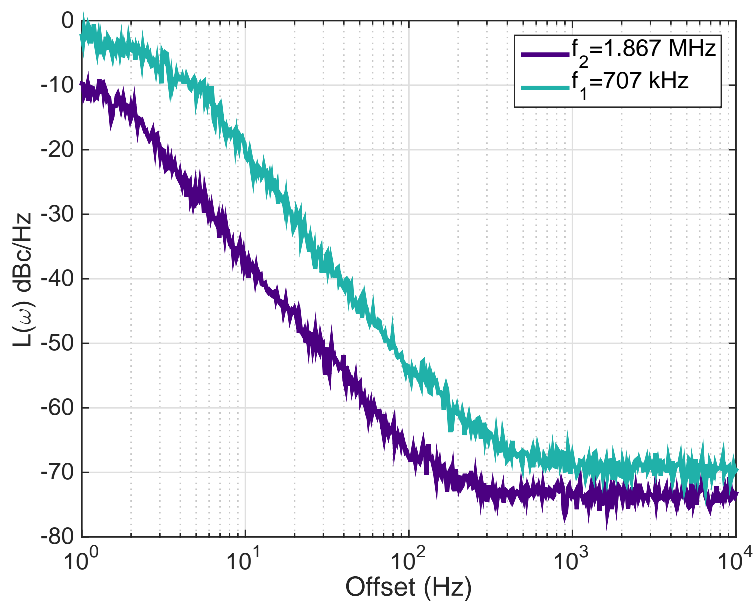

Figure 6.15: Comparison of phase noise measured in first and second mode of Device #3.

second mode had a $1/f^3$ frequency dependence, as expected for anomalous phase noise.

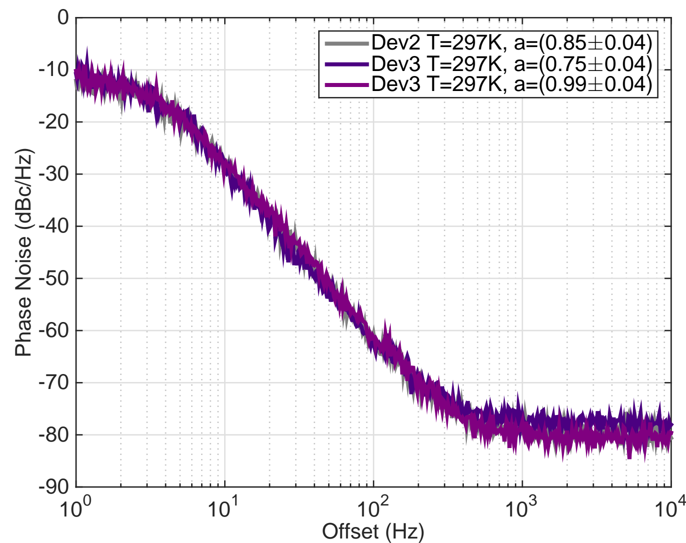

Figure 6.16: Comparison of Phase Noise at 297 K

6.6 Back Action

There are several sources of noise in the measurement system that could potentially lead to noise with a $1/f^3$ frequency dependence. In this section, we consider the effects of heating from both the actuation laser and the detection laser. In the following section, we consider noise due to amplifiers and parameter fluctuations using the framework developed in Chapter 4.

We begin by assessing the heating from the actuation laser at 297 K. Ideally, we would determine the back action at all measurement temperatures, but we only have data for 297K. In addition, a definitive measurement of back action would require increasing the heating from the actuation laser until an increase in phase noise was observed. However, the instrumentation used to measure phase noise broke. Instead, we compare the measurement of phase noise at 297K, where we accidentally used two different neutral density filters for the measurements on Device #2 and Device #3. For reference, we repeat the data previously shown in Figure 6.10. The data for Device #2 was taken with a neutral density filter with ND=4.0, a modulation depth of ≈ -22 dBm, and $I_D = 48$ mA. Before the neutral density filter, the maximum

power is $\approx$ 1.7 mW. After the neutral density filter[1], the maximum power is $\approx$ 0.93 μW. The data for Device #3 with an operating point of (a = 0.99 ± 0.04) was taken with a neutral density filter with ND=2.6, a modulation depth of ≈ -45 dBm, and I_D = 48 mA. Before the neutral density filter, the maximum power is $\approx$ 0.96 mW. After the neutral density filter, the maximum power is $\approx$ 7.3 μW. Decreasing the maximum drive power by almost a factor of 10 did not lead to a decrease in phase noise, which suggests that the measurement was not limited by heating due to the actuation laser at 297 K.

Ideally, we would assess heating due to the detection laser by measuring the phase noise while increasing the power from the detection laser. However, as previously noted, the instrumentation used to measure phase noise broke. In Chapter 5, we measured the shift in resonant frequency versus optical detection power. The power level chosen for the measurements (3 μW) corresponded to a minimum in the frequency shift, which should lead to the minimum amount of heating. Further measurements are required to determine if the detection beam caused heating in the device and additional noise in the measurement.

6.7 Noise Analysis

We now consider the phase noise in the system using the framework introduced in Section 4.1. In the analysis, we ignore fluctuations in both α and γ; we assume that the nonlinearity of the resonator and the intrinsic damping remain constant. Following the noise analysis performed by Villanueva et al. [31], we begin our analysis by measuring the phase noise of every component in the system with a test signal. We used a Keysight N5181A signal generator to apply a signal with a frequency of 715 kHz and a magnitude on the order of the signal at the component under test in the oscillator loop for a typical measurement. We then measured the

[1] 690nm is at the edge of the design wavelength for the neutral density filters and the filters allow more than the quoted light through.

phase noise at the output of the component under test. We did not observe phase noise on a level comparable to the phase noise previously measured in this chapter from any component. We compare the phase noise of the test signal with two drive levels in Figure 6.17. These two drive levels were used to attain the correct signal level input at different components under test. We next compare the phase noise

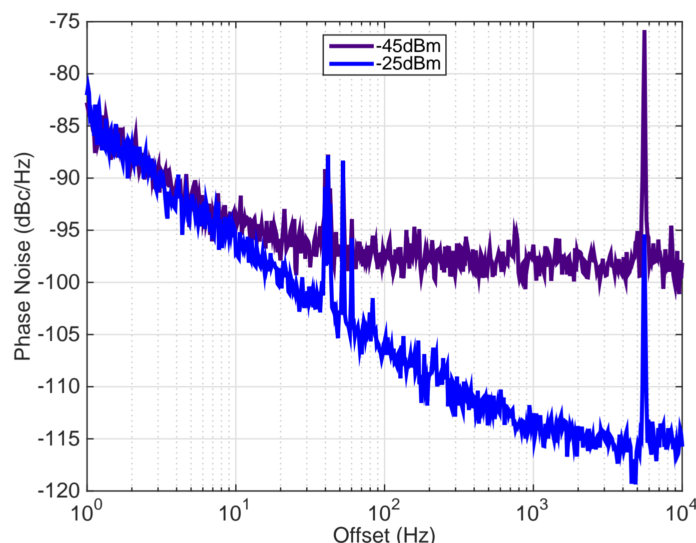

Figure 6.17: Comparison of phase noise from N518A at two different drive levels

from the components under test in Figure 6.18. The gray trace corresponds to the phase noise from the signal generator with a drive level of -45 dBm. The test signal was fed into the low noise amplifier (LNA), a MiniCircuits ZFL-1000LN+, which was followed by an attenuator of 5 dB and a Mini-Circuits ZFSC-2-4-S+ 0° power splitter. The dark purple trace corresponds to the phase noise measured at the output of the power splitter; it has the same magnitude as the phase noise measured from the signal generator with a drive level of -45 dBm. We next fed the test signal from the signal generator with a drive level of -25 dBm into a Mini-Circuits BLP-1.9 low pass filter, whose output was then fed into the AGC. The light purple trace corresponds to the phase noise measured at the output of the AGC; the measured phase noise is on the order of the phase noise of the drive signal. We then applied the test signal with

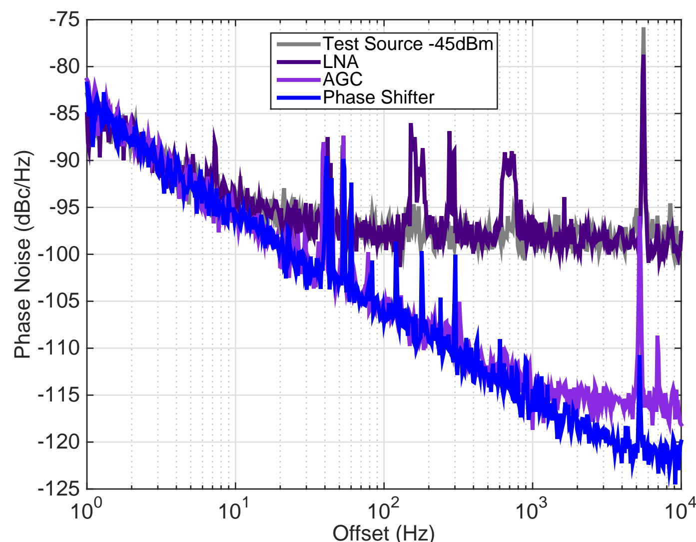

Figure 6.18: Comparison of phase noise from components under test

a drive level of -13 dBm to the Mini-Circuits JCPHS-2.5+ variable voltage phase shifter. The phase noise measured at the output of the phase shifter, shown in blue, is on the order of the phase noise of the test signal from the signal generator. All of the components tested contributed minimal phase noise to the measurement.

We also consider $1/f$ noise from the electronics used in the feedback loop that is converted to $1/f^3$ noise by the resonator via the Leeson effect. Assuming a quality factor of 15000 and an offset frequency of 10 Hz, the resonator would increase the magnitude of a $1/f$ noise source by 23 dBm at a 10 Hz frequency offset. None of the components under test generated $1/f$ noise with a magnitude of -30 dBc/Hz at a 10 Hz offset, which is the level required to generate the phase noise measured earlier in the chapter. Thus, the previously measured phase noise is not caused by $1/f$ noise from the electronics.

From the phase noise measurements on the components in the oscillator loop, we determined that the largest source of phase noise in the oscillator loop, other than the resonator, was the photodetector. We now perform the noise analysis for Device #3 at T=297K, with an operating point ($a = 0.75$, $\Delta = \pi/2$). We first consider phase

noise due to thermomechanical motion, both the direct component and the amplitude to phase conversion component. Using the measured parameters, $I_{Th} = \frac{k_B T Q_0 \tilde{\alpha_0}}{M_{eff}^2 \Omega_0^4} = 2.2 \times 10^{-4}$, $D_{direct} = \frac{1}{a^2} = 1.80$, and $D_a = \left(\frac{3}{2}a + \frac{1}{a^2}\cos(\Delta)\right)^2 = 2.25a^2 = 1.25$. We plot the phase noise due to thermomechanical motion and compare it with the measured phase noise in Figure 6.19 We next consider phase noise from fluctuations in Δ. The shot noise from the photodetector is fed back to the device; it is a signal with a well defined amplitude, but a poorly defined phase, which corresponds to fluctuations in Δ. In the oscillator loop, the gain chain is highly saturated due to the AGC. For a highly saturated gain chain, the noise from fluctuations in Δ is the ratio of noise from the photodetector and $\frac{3}{2}$ of the product of a and s: $I_\Delta = \frac{2S_a}{3a \cdot s}$. From large bandwidth measurements of thermomechanical noise, we determine a responsivity between S_a and I_{Th}. In Chapter 5, we found a background noise of 4.4×10^{-13} V^2/Hz and $S_v^{th}(\Omega_0) = 1.15 \times 10^{-10}$ V^2/Hz, which leads to a responsivity $\mathscr{R}_\Delta = 3.8 \times 10^{-3}$. This background noise and thermomechanical noise were measured on Device #3 during the calibration measurements prior to the phase noise measurement at T=297 K; these value correspond to typical values during the measurement. Thus, we obtain:

$$I_\Delta = \frac{2\mathscr{R}_\Delta I_{Th}}{3a \cdot s}. \tag{6.3}$$

For the operating parameters, $D_\Delta = 1/4$ and $s = a$. Ideally, we would have confirmed the estimate of noise due to fluctuations in Δ by adding an additional white noise source between the photodetector and the LNA and then measuring the change in phase noise. We end our analysis by considering fluctuations in s. Ideally, we would have measured the phase noise at the output of the AGC while applying a signal with a small amplitude modulation on the order of the response time of the AGC, between 1-10 kHz, in order to simulation fluctuations in s. However, due to broken instrumentation, we were unable to perform this test. We instead assume that $I_s = I_{Th}$, since I_{Th} was previously the largest source of noise in the system;

$D_s = (\frac{3}{4}a)^2 = 0.32$ for this operating point. We plot the comparison of phase noise in Figure 6.19. The largest source of phase noise is direct thermomechanical noise; however, the phase noise due to direct thermomechanical noise has a smaller magnitude and different frequency dependence than the measured phase noise. None of the sources of phase noise considered would generate the phase noise measured.

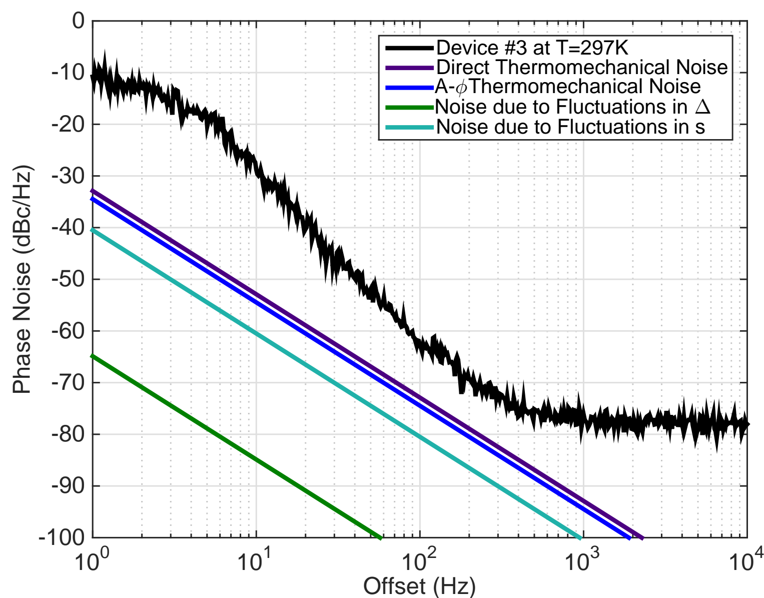

Figure 6.19: Comparison of measured phase noise and estimated phase noise due to thermomechanical fluctuations, fluctuations in Δ, and fluctuations in s.

6.8 Summary

We measured the phase noise of two silicon double clamped beams over a range of temperatures in order to characterize the temperature dependence and the frequency dependence of anomalous phase noise. We observed a $1/f^3$ frequency dependence and a T^α with $\alpha \approx 1.5$ dependence for the beams. We also observed anomalous phase noise in the second mode of one of the beams. We assessed sources of back action and noise in the system and determined that none of them could generate the measured phase noise. In conclusion, our measurements confirm that anomalous phase noise decreases with temperature; we can decrease the contribution from anomalous phase

noise in future frequency shift based sensors by performing measurements at low temperatures in a dilution refrigerator.

Chapter 7

CONCLUSION

In this thesis, we focused on two areas of interest in MEMS and NEMS: predicting the quality factor due to gas damping without numerical simulations and characterizing anomalous phase noise. We determined that the dynamic similarity principle provides an alternate method for predicting the quality factor due to gas damping. We also further characterized anomalous phase noise and ruled out several potential sources of anomalous phase noise. From our measurements, we conclude that anomalous phase noise is temperature dependent and it can be reduced by performing measurements at low temperatures in a dilution refrigerator.

The source of anomalous phase noise remains unclear. Further measurements should be made on silicon doubly clamped beams with different orientations with respect to the crystal axis in order to determine if changing the Young's modulus affects anomalous phase noise. Measurements should also be performed on silicon doubly clamped beams with differing volumes in order to determine the volume dependence of anomalous phase noise. These measurements should provide the information required to determine techniques to reduce anomalous phase noise through device engineering. Additional measurements should also be made to further quantify the relationship between temperature and anomalous phase noise. In addition, annealing experiments should be performed on devices to determine if heating the device, and consequently, lowering the number of defects, leads to lower anomalous phase noise.

BIBLIOGRAPHY

[1]G. Binnig, C. F. Quate, and C. Gerber, "Atomic force microscope", Phys. Rev. Lett. **56**, 930–933 (1986).

[2]M. Li, H. X. Tang, and M. L. Roukes, "Ultra-sensitive nems-based cantilevers for sensing, scanned probe and very high-frequency applications", Nature Nanotechnology **2**, 114–120 (2007).

[3]K. Jensen, K. Kim, and A. Zettl, "An atomic-resolution nanomechanical mass sensor", Nature Nanotechnology **3**, 533–537 (2008).

[4]M. S. Hanay, S. Kelber, A. K. Naik, D. Chi, S. Hentz, E. C. Bullard, E. Colinet, L. Duraffourg, and M. L. Roukes, "Single-protein nanomechanical mass spectrometry in real time", Nature Nanotechnology **7**, 602–608 (2012).

[5]D. P. E. Smith, "Limits of force microscopy", Review of Scientific Instruments **66**, 3191 (1995).

[6]K. L. Ekinci and M. L. Roukes, "Nanoelectromechanical systems", Review of Scientific Instruments **76**, 061101 (2005).

[7]G. Karniadakis, A. Beskok, and N. Aluru, *Microflows and nanoflows: fundamentals and simulation* (Springer, New York, 2005).

[8]B. Zohuri, *Dimensional analysis and self-similarity methods for engineers and scientists* (Springer, 2015).

[9]J. O'Hanlon, *A user's guide to vacuum technology*, 3rd (Wiley-Interscience, New Jersey, 2003).

[10]J. E. Sader, J. Pacifico, C. P. Green, and P. Mulvaney, "General scaling law for stiffness measurement of small bodies with applications to the atomic force microscope", Journal of Applied Physics **97**, 124903 (2005).

[11]R. W. Fox, A. T. McDonald, and P. J. Pritchard, *Introduction to fluid mechanics*, 6th (John Wiley and Sons, 2004).

[12]J. E. Sader, "Frequency response of cantilever beams immersed in viscous fluids with applications to the atomic force microscope", Journal of Applied Physics **84**, 64–76 (1998).

[13]D. L. Roy, W. Yang, X. Yin, R. Y. Lai, S.-H. Liou, and D. J. Sellmyer, "High-sensitivity detector for molecular sensing using magnetic particles", Journal of Applied Physics **109**, 07E532 (2011).

[14]W. N. Sharpe, ed., *Springer handbook of experimental solid mechanics* (Springer Science+Business Media, 2008).

[15]D. Rugar, H. J. Mamin, R. Erlandsson, J. E. Stern, and B. D. Terris, “Force microscope using a fiber-optic displacement sensor”, Review of Scientific Instruments **59**, 2337–2340 (1988).

[16]R. E. Fischer and B. Tadic-Galeb, *Optical system design* (McGraw Hill, New York, 2000).

[17]K. Ekinci, Y. Yang, and M. Roukes, “Ultimate limits to inertial mass sensing based upon nanoelectromechanical systems”, Journal of Applied Physics **95**, 2682–2689 (2004).

[18]J. E. Sader, I. Larson, P. Mulvaney, and L. R. White, “Method for the calibration of atomic force microscope cantilevers”, Review of Scientific Instruments **66**, 3789–3798 (1995).

[19]E. C. Bullard, J. Li, C. R. Lilley, P. Mulvaney, M. L. Roukes, and J. E. Sader, “Dynamic similarity of oscillatory flows induced by nanomechanical resonators”, Phys. Rev. Lett. **112**, 015501 (2014).

[20]D. Rugar, R. Budakian, H. J. Mamin, and B. W. Chui, “Single spin detection by magnetic resonance force microscopy”, Nature **430**, 329–332 (2004).

[21]M. Li, E. B. Myers, H. X. Tang, S. J. Aldridge, H. C. McCaig, J. J. Whiting, R. J. Simonson, N. S. Lewis, and M. L. Roukes, “Nanoelectromechanical resonator arrays for ultrafast, gas-phase chromatographic chemical analysis”, Nano Letters **10**, 3899–3903 (2010).

[22]C.-C. Nguyen and R. Howe, “An integrated cmos micromechanical resonator high-q oscillator”, Solid-State Circuits, IEEE Journal of **34**, 440–455 (1999).

[23]C. T. .-.-C. Nguyen, “Mems technology for timing and frequency control”, Ultrasonics, Ferroelectrics, and Frequency Control, IEEE Transactions on **54**, 251–270 (2007).

[24]J. T. M. van Beek and R. Puers, “A review of mems oscillators for frequency reference and timing applications”, Journal of Micromechanics and Microengineering **22**, 013001 (2012).

[25]T. L. Naing, T. Rocheleau, E. Alon, and C.-C. Nguyen, “A 78-microwatt gsm phase noise-compliant pierce oscillator referenced to a 61-mhz wine-glass disk resonator”, in European frequency and time forum international frequency control symposium (eftf/ifc), 2013 joint (July 2013), pp. 562–565.

[26]E. Sage, “Nouveau concept de spectrometre de masse a base de reseaux de nanostructures oscillantes”, PhD thesis (L’Université Joseph Fourier, 2014).

[27]S. Hentz, “Downscaling silicon resonant mems and nems sensors: devices, transduction, non-linear dynamics and applications”, PhD thesis (Institut National des Sciences Appliquées de Lyon, 2012).

[28]A. K. Naik, M. S. Hanay, W. K. Hiebert, X. L. Feng, and M. L. Roukes, "Towards single-molecule nanomechanical mass spectrometry", Nat Nano **4**, 445–450 (2009).

[29]E. Gavartin, P. Verlot, and T. J. Kippenberg, "Stabilization of a linear nanomechanical oscillator to its thermodynamic limit", Nat Commun **4** (2013).

[30]L. G. Villanueva, R. B. Karabalin, M. H. Matheny, E. Kenig, M. C. Cross, and M. L. Roukes, "A nanoscale parametric feedback oscillator", Nano Letters **11**, 5054–5059 (2011).

[31]L. G. Villanueva, E. Kenig, R. B. Karabalin, M. H. Matheny, R. Lifshitz, M. C. Cross, and M. L. Roukes, "Surpassing fundamental limits of oscillators using nonlinear resonators", Phys. Rev. Lett. **110**, 177208 (2013).

[32]C. Chen, S. Lee, V. V. Deshpande, G.-H. Lee, M. Lekas, K. Shepard, and J. Hone, "Graphene mechanical oscillators with tunable frequency", Nat Nano **8**, 923–927 (2013).

[33]K. Y. Fong, W. H. P. Pernice, and H. X. Tang, "Frequency and phase noise of ultrahigh q silicon nitride nanomechanical resonators", Phys. Rev. B **85**, 161410 (2012).

[34]M. Sansa, E. Sage, E. C. Bullard, M. Gély, T. Alava, E. Colinet, A. K. Naik, L. G. Villanueva, Duraffourg, M. L. Roukes, G. Jourdan, and S. Hentz, "Frequency fluctuations in silicon nanoresonators", Nature Nanotechnology (2016) doi:10.1038/nnano.2016.19.

[35]E. Rubiola, *Phase noise and frequency stability in oscillators* (Cambridge University Press, 2009).

[36]I. S. C. C. 27, "Ieee standard definitions of physical quantities for fundamental frequency and time metrology—random instabilities", IEEE STD 1139-2008, c1–35 (2008).

[37]T. H. Lee and A. Hajimiri, "Oscillator phase noise: a tutorial", Solid-State Circuits, IEEE Journal of **35**, 326–336 (2000).

[38]F. Reif, *Fundamentals of statistical and thermal physics* (McGraw-Hill, 1965).

[39]P. Dutta, P. Dimon, and P. M. Horn, "Energy scales for noise processes in metals", Phys. Rev. Lett. **43**, 646–649 (1979).

[40]P. Dutta and P. M. Horn, "Low-frequency fluctuations in solids: 1/f noise", Reviews of Modern Physics **53**, 497–516 (1981).

[41]M. B. Weissman, "$\frac{1}{f}$ noise and other slow, nonexponential kinetics in condensed matter", Rev. Mod. Phys. **60**, 537–571 (1988).

[42]T. Parker, "Characteristics and sources of phase noise in stable oscillators", in 41st annual symposium on frequency control. 1987 (May 1987), pp. 99–110.

[43]V. F. Kroupa, *Frequency stability: introduction and applicaitons* (IEEE Press, 2012).

[44]H. W. C. Postma, I. Kozinsky, A. Husain, and M. L. Roukes, “Dynamic range of nanotube- and nanowire-based electromechanical systems”, Applied Physics Letters **86**, 223105–3 (2005).

[45]Y. T. Yang, C. Callegari, X. L. Feng, K. L. Ekinci, and M. L. Roukes, “Zeptogram-scale nanomechanical mass sensing”, Nano Letters **6**, 583–586 (2006).

[46]J. Gao, J. Zmuidzinas, B. A. Mazin, H. G. LeDuc, and P. K. Day, “Noise properties of superconducting coplanar waveguide microwave resonators”, Applied Physics Letters **90**, 102507 (2007) `http://dx.doi.org/10.1063/1.2711770`.

[47]Y. Zhang, J. Moser, J. Güttinger, A. Bachtold, and M. I. Dykman, “Interplay of driving and frequency noise in the spectra of vibrational systems”, Phys. Rev. Lett. **113**, 255502 (2014).

[48]E. Kenig, M. C. Cross, L. G. Villanueva, R. B. Karabalin, M. H. Matheny, R. Lifshitz, and M. L. Roukes, “Optimal operating points of oscillators using nonlinear resonators”, Phys. Rev. E **86**, 056207 (2012).

[49]E. Kenig and M. C. Cross, “Frequency precision of oscillators based on high-q resonators”, arXiv:1510.07331v2, 2015.

[50]D. S. Greywall, B. Yurke, P. A. Busch, A. N. Pargellis, and R. L. Willett, “Evading amplifier noise in nonlinear oscillators”, Physical Review Letters **72** (1994).

[51]H. K. Lee, R. Melamud, S. Chandorkar, J. Salvia, S. Yoneoka, and T. Kenny, “Stable operation of mems oscillators far above the critical vibration amplitude in the nonlinear regime”, Microelectromechanical Systems, Journal of **20**, 1228–1230 (2011).

[52]A. N. Cleland and M. L. Roukes, “Noise processes in nanomechanical resonators”, Journal of Applied Physics **92**, 2758–2769 (2002).

[53]M. A. Hopcroft, W. D. Nix, and T. W. Kenny, “What is the young’s modulus of silicon?”, Microelectromechanical Systems, Journal of **19**, 229–238 (April 2010).

[54]W. M. Haynes, ed., *Crc handbook of chemistry and physics*, 95th ed. (CRC Press, 2014).

[55]W. P. Mason and T. B. Bateman, “Ultrasonic wave propagation in doped n-germanium and p-silicon”, Phys. Rev. **134**, A1387–A1396 (1964).

[56]M. H. Matheny, L. G. Villanueva, R. B. Karabalin, J. E. Sader, and M. L. Roukes, “Nonlinear mode-coupling in nanomechanical systems”, Nano Letters **13**, 1622–1626 (2013).

[57]A. N. Cleland, *Foundations of nanomechancics: from solid-state theory to device applications* (Springer-Verlag Berlind Heidelberg, 2003).

[58]M. Asheghi, M. N. Touzelbaev, K. E. Goodson, Y. K. Leung, and S. S. Wong, "Temperature-dependent thermal conductivity of single-crystal silicon layers in soi substrates", Journal of Heat Transfer **120**, 30–36 (1998).

[59]G. Bekefi and A. H. Barrett, *Electromagnetic vibrations, waves, and radiation*, 6th (MIT Press, 1990).

[60]G. Bahl, R. Melamud, B. Kim, S. A. Chandorkar, J. Salvia, M. Hopcroft, D. Elata, R. Hennessy, R. Candler, R. Howe, and T. Kenny, "Model and observations of dielectric charge in thermally oxidized silicon resonators", Microelectromechanical Systems, Journal of **19**, 162–174 (2010).

[61]Y. K. Yong and J. R. Vig, "Modeling resonator frequency fluctuations induced by adsorbing and desorbing surface molecules", IEEE Transactions On Ultrasonics Ferroelectrics and Frequency Control **37**, 543–550 (1990).

[62]A. Zangwill, *Physics at surfaces* (Cambridge University Press, 1988).

[63]K. Kolasinski, *Surface science: foundations of catalysis and nanoscience*, 2nd (John Wiley and Sons, 2008).

[64]Y. T. Yang, C. Callegari, X. L. Feng, and M. L. Roukes, "Surface adsorbate fluctuations and noise in nanoelectromechanical systems", Nano Letters **11**, 1753–1759 (2011).

[65]M. S. Hanay, S. I. Kelber, C. D. O'Connell, P. Mulvaney, J. E. Sader, and M. L. Roukes, "Inertial imaging with nanomechanical systems", Nat Nano **10**, 339–344 (2015).

[66]E. Sage, A. Brenac, T. Alava, R. Morel, C. Dupré, M. S. Hanay, M. L. Roukes, L. Duraffourg, C. Masselon, and S. Hentz, "Neutral particle mass spectrometry with nanomechanical systems", Nat Commun **6** (2015).

[67]A. S. Nowick and B. S. Berry, *Anelastic relaxation in crystalline solids* (Academic Press, 1972).

[68]A. Zimmer, R. Nawrodt, D. Heinert, C. Schwarz, M. Hudl, T. Koettig, W. Vodel, A. Tünnermann, and P. Seidel, "Mechanical losses in low loss materials studied by cryogenic resonant acoustic spectroscopy of bulk materials (cra spectroscopy)", Journal of Physics: Conference Series **92**, 012095 (2007).

[69]J. H. Scofield, J. V. Mantese, and W. W. Webb, "Temperature dependence of noise processes in metals", Phys. Rev. B **34**, 723–731 (1986).

[70]B. G. Svensson, B. Mohadjeri, A. Hallén, J. H. Svensson, and J. W. Corbett, "Divacancy acceptor levels in ion-irradiated silicon", Phys. Rev. B **43**, 2292–2298 (1991).

[71]E. Hecht, *Optics*, Vol. 4th (Addison-Wesley, 2002).

[72]A. A. Siegman, *Lasers* (University Science Books, 1986).

[73]H. Urey, “Spot size, depth-of-focus, and diffraction ring intensity formulas for truncated gaussian beams”, Appl. Opt. **43**, 620–625 (2004).

[74]H. Gross, ed., *Handbook of optical systems*, Vol. 1 (Wiley-VCH, 2005).

[75]W. J. Smith, *Modern optical engineering*, 4th (SPIE Press, 2008).

[76]B. D. Hauer, C. Doolin, K. S. D. Beach, and J. P. Davis, “A general procedure for thermomechanical calibration of nano/micro-mechanical resonators”, Annals of Physics **339**, 181–207 (2013).

[77]B. Ilic, S. Krylov, K. Aubin, R. Reichenbach, and H. G. Craighead, “Optical excitation of nanoelectromechanical oscillators”, Applied Physics Letters **86**, 193114–3 (2005).

[78]B. Ilic, S. Krylov, and H. G. Craighead, “Theoretical and experimental investigation of optically driven nanoelectromechanical oscillators”, Journal of Applied Physics **107**, 034311–13 (2010).

[79]D. Rugar, B. C. Stipe, H. J. Mamin, C. S. Yannoni, T. D. Stowe, K. Y. Yasumura, and T. W. Kenny, “Adventures in attonewton force detection”, Applied Physics A: Materials Science & Processing **72**, S3–S10 (2001).

[80]H. J. Mamin and D. Rugar, “Sub-attonewton force detection at millikelvin temperatures”, Applied Physics Letters **79**, 3358–3360 (2001).